Hydrodynamic Modelling Report

Technical Report A - Annexure H

HydroNumerics

HydroNumerics

Crib Point Gas Import Facility

Hydrodynamic Modelling Report

Final Report

June 2020

Report prepared for CEE Pty Ltd

HydroNumerics Pty Ltd
ABN 87 142 999 246
www.hydronumerics.com.au

NOTICE

DISCLAIMER

The accuracy of information presented in this document is entirely dependent on the accuracy and completeness of supplied information. Hydronumerics Pty Ltd makes no warranty, representation or guarantee with respect to the accuracy and completeness of supplied information, shall have no liability to any person for any errors or omissions in the supplied information, and shall have no liability for loss or damage of any kind suffered or incurred by any person acting in reliance on the information in this document where the loss or damage arises from errors or omissions in the supplied information.

EXECUTIVE SUMMARY

Western Port Bay (WPB) is an embayment on the coast of southern Victoria. The bay consists of a complex series of deep channels, intertidal flats and two large islands - French Island in the north and Phillip Island to the south. Exchange of seawater between the bay and Bass Strait is through a wide western entrance at Flinders and a small entrance between Phillip Island and San Remo.

AGL Wholesale Gas Ltd (AGL) is assessing the feasibility of mooring a Floating Storage and Regasification Unit (FSRU) at Crib Point Jetty in the north arm of WPB to supply Liquefied Natural Gas (LNG) to its customers in south-eastern Australia. The Crib Point Jetty has been selected by AGL as the preferred location for a continuously moored FSRU because it is an established port with existing jetty infrastructure and close to the Victorian gas network.

At peak production rate the FSRU heat-exchange process will extract up to 468,000 m^3 of seawater per day from WPB through sea chests on the port and starboard side of the vessel. The seawater will pass through heat exchangers before being discharged back to the bay at up to 7 ^oC cooler via 6 ports on the starboard side.

The discharge will create a plume that is cooler, and therefore of higher density, than the surrounding seawater. During periods of low currents, the plume is expected to descend to the seabed at a lateral distance of approximately 60 m from the discharge ports (CEE, 2018a). The extent of the plume at the seabed will depend on the momentum of the discharge exiting the ports and the transport and mixing imparted by the ambient flow (northward during flood tide and southward during ebb tide) as the dense plume descends under the action of gravity.

There are three heat exchangers on the FSRU, each with two ports, so depending on the level of gas production two, four or six ports will be operating concurrently. This report considers peak production rates (discharge of 468,000 m^3/day, i.e. 5.4 m^3/s) and average production rates (discharge of 312,000 m^3/day, i.e. 3.6 m^3/s).

The intake seawater is chlorinated by electrolysis to control fouling in the pumps, pipes and heat exchangers. On discharge, the residual chlorine concentration will be 100 µg/L or lower.

Hydronumerics was commissioned to assist with an assessment of the potential impact on the marine environment associated with the intake seawater and seawater discharge, during operation of the FSRU. The objectives of this assessment are to:

- Assess the extent of the plume of cooler seawater on the sea floor;
- Assess the distribution of residual chlorine in the discharged seawater; and
- Assess the extent of entrainment of larvae released from various points in WPB into the FSRU.

To undertake these assessments, a three-dimensional model of the whole of WPB was used. An existing Aquatic Ecosystem Model 3D (AEM3D) model of WPB that was previously developed for Melbourne Water and EPA Victoria was modified and applied in this project.

The key changes to the model were to increase the resolution of the grid and upgrade model boundary conditions. Two new model grids were developed: a 50 x 50 m resolution grid in the region around Crib Point, extending to 200 x 200 m and then 500 x 500 m out into Bass Strait; and a 20 x 20 m grid in the Crib Point region that stepped out to 200 m for the remainder of the bay. The finer model grid provided higher resolution around the project site for the purpose of the FSRU discharge modelling and the coarser model grid allowed longer simulation times.

The Australian Community Climate and Earth-System Simulator (ACCESS) weather model outputs from the Australian Bureau of Meteorology (BoM) were used to provide spatially distributed meteorological inputs at the surface of the model, in contrast to earlier models that applied meteorological data from a single site. This upgrade accounted for wind-field changes over the expanse of the bay.

BoM Ocean Modelling, Analysis, and Prediction System (OceanMAPS) model outputs were used to define sea level, surface salinity and daily temperature profiles at the ocean boundary. The Oregon State University's Tidal Data Inversion Software (OTIS) was used to generate latitude and longitude specific tidal oscillations over the length of ocean boundary.

ACCESS atmospheric data and OceamMaps oceanographic data was used to generate a continuous 11-month period of model boundary forcing from June 2018 to April 2019.

Three Acoustic Doppler Current Profilers (ADCPs) were deployed in March and April of 2019 at Crib Point Jetty, in the main northern channel east of Crib Point and further east in the narrow eastern channel of the North Arm. Each ADCP was deployed at the seabed and set to record current, water level, and temperature every 10 minutes in 1 m vertical bins. These measurements were used to check the model predictions of sea level and northward and eastward current components near the seabed, at mid-depth and near the water surface.

Overall, the model reproduced the observed dominant north-south vector components well and reliably reproduced the timing of changes in the observed current. However, at the middle ADCP, the model briefly produced 10 to 20% higher peaks in near-surface southerly currents compared to the observed currents. In addition, the modelled north-south currents under-predict the measured bottom currents at the western ADCP during the ebb tide. These discrepancies relate in part to the 3D gridded representation of the bathymetry and are more pronounced during spring ebbing tide when water level is lowest. There was good agreement between simulated and measured speed and direction of the median and 75th percentile ebb and flood tide currents at 2, 5 and 9 m above the seabed at all three ADCP sites.

To model the plume behaviour of the cool water discharged from the FSRU, the dilution and trajectory of the near-field plumes were modelled by CEE and mapped into the hydrodynamic grid of the regional 3D model of the bay. The results show that with faster currents, the plume more rapidly entrains the transverse momentum of the ambient tidal current and turns into the current, thereby limiting the lateral travel (east from the FSRU) of the plume. With weaker currents, there is a larger lateral travel, and also a greater sinking of the plume towards the seabed. The hydrodynamic model simulations included the effects of the vessel hull on the local currents under and around the moored vessel. The situation with an LNG tanker moored parallel to the FSRU also was modelled.

The discharge was modelled over a 28-day period using the 20 x 20 m resolution grid for peak and average FSRU production rates. Additional model sensitivity simulations were undertaken to examine the effects of differing port configurations and thus near-field dilution.

The simulation results for peak production indicate that the dispersion of the discharge has several different patterns during a tidal cycle. During mid-tide there is a strong ambient current that entrains the discharge rapidly in the water column so that the discharge mixes and travels north on a flooding tide, or south on the ebbing tide. Temperatures at the seabed are predominately warmer than -0.3 °C from ambient during this part of the tidal cycle.

For low and high tide, when the ambient currents slow (i.e. near and at slack water) the plume descends to the bed where it can pool for a short period. During this time, cooling of -0.7 °C or lower are predicted beside the FSRU as the plume plunges to the east of the vessel. While the estimated near-field plume dilution (for discharge -7 °C from ambient) is 20 to 26:1, depending on the tidal stage (CEE, 2018a), corresponding to a temperature reduction averaging -0.3 °C from ambient, the slack water lasts longer than the plume evolution time so near-field dilution is reduced as the plumes entrain pre-cooled ambient seawater during descent.

Shortly after slack water, and as the tidal currents increase, the plume of new discharge water moves back towards the mid-depth as the transport and dilution increases with the increasing ambient currents. The plume no longer plunges to the bed returning to the mid-tide state described above. The water that pooled near the bed during slack water travels predominately north (during flood tide) or south (during ebb tide) with the increasing currents and dilutes as it travels.

There is less east-west movement of the plume during this time due to the dominance of the north-south flow. As the patches of cooler water travel along the seabed under the action of the currents, the pooled water is diluted by vertical and lateral mixing as shear increases, until mixing erodes the plume completely. Within approximately 1.5 hours of slack water, temperature reductions are -0.3 °C from ambient or warmer at the seabed below the FSRU and at sites 300 to 400 m north (during flood tide) and south (during ebb tide).

Temperature Outcomes

The following summary can be drawn for temperature changes at the seabed during peak FSRU discharge rate of 5.4 m^3/s:

- For 10 % of the time there is a small area of seabed beside the FSRU (and extending for less than the dimensions for the FSRU) that experiences cooling of -0.3 to -0.5 °C from ambient; and
- For 5 % of the time there is:
    - A region beneath the plunging zone of the plume (approx. 100 m by 100 m) that experiences cooling of -0.5 to -0.7 °C from ambient; and
    - An outer region that extends up to 300 m north and south of the FSRU that experiences cooling of -0.3 to -0.5 °C from ambient. The width of the elongated plume is approximately 50 to 200 m, and widest near the FSRU.

For the average FSRU discharge rate of 3.6 m^3/s:

- For 5 % of the time there is region beneath the plunging area of the plume (approx. 100 m by 100 m) that experiences cooling of -0.3 to 0.5 °C from ambient.

At the bay-wide scale, heat fluxes are dominated by exchanges with the ocean and atmosphere (on diurnal and seasonal cycles and during events such as storms) so that the dispersed cool water has a local effect but a negligible large scale or cumulative effect on the water temperatures in the remainder of the bay.

Chlorine Outcomes

The FSRU produces chlorine in the seawater used for cooling and other purposes by electrolysis of the sodium chloride in the seawater drawn into the vessel. There is rapid decay of the chlorine as it passes through the pipes and heat exchangers. At the discharge ports, the chlorine level will be a maximum concentration of 100 μg/L. Over the same 28-day simulation for cool-water discharge the concentrations of chlorine at the seabed were assessed.

Consistent with CSIRO's report (Batley and Simpson, 2019), CEE has adopted a CPO (chlorine produced oxidants) guideline value of 6 μg Cl/L for 99% species protection for assessing potential impacts at Crib Point where strong tidal reversals in currents result in intermittent exposure of biota to dispersing discharge. For the great majority of the time the chlorine is dispersed and diluted to concentrations less that 6 μg/L in the vicinity of the FSRU and lower concentrations beyond the project area.

The modelling indicated for the peak FSRU discharge rate of 5.4 m^3/s, 5% of the time there is a patch on the seabed (approx. 200 m N-S by 150 m E-W) where the discharge plume plunges and chlorine concentrations at the seabed are higher than 6 μg/L.

For average discharge of 3.6 m^3/s, 5% of the time there is a patch on the seabed (approx. 50 m by 50 m) where the discharge plume plunges and chlorine concentrations at the seabed are higher than 6 μg/L.

These percentile results reflect short-duration concentration peaks. The time-weighted average chlorine concentration near the FSRU is below 2 μg/L which is below the guideline value of 6 μg/L.

Because there is rapid chemical change, and because of the large exchange of waters between the project area and the remainder of the bay (and ultimately with Bass Strait), the cumulative effects of chlorine discharge from the FSRU in the project area and more broadly over the remainder of the bay are expected to be negligible. The chlorine created by electrolysis of seawater returns to the chloride (as part of sodium chloride) in seawater in a day or so, so there is no long-term accumulation of chlorine in the bay (CEE 2018d).

Plankton Entrainment Outcomes

The potential entrainment of plankton into the FSRU (e.g. plankton and fish larvae) from different regions of the bay was simulated in the model by releasing neutrally buoyant particles into various zones in the western and northern parts of the bay. The position of each particle was determined in the model every 10 minutes. To allow a 28 days run time, the 50 x 50 m model grid was used for the particle release and capture simulations.

The dimensions of the entrainment volume associated with seawater intake by the FSRU were determined as a function of the current speed (CEE, 2018b). These dimensions were applied to determine the number of the released particles from each zone that travel into the intake entrainment zone. As a sensitivity analysis, a series of counts were made based on particle release at different stages of the tide (spring, neap, rising and falling) and with different initial distributions (vertical and horizontal).

Simulation results for intake rate of 5.2 m^3/s indicate that the highest entrainment occurs for particles released in the main channel close to Crib Point, where 0.75% of particles are predicted to be captured over a 28-day period. For zones further away, the entrainment ranged between 0.41 % (east of Crib Point) to less than 0.1 % in the western entrance to the bay. The average entrainment rate for North Arm was 0.38% over 28 days for a 5.2 m^3/s intake rate and 0.26% over 28 days for a simulated intake rate of 3.5 m^3/s.

The entrainment asymptotes towards the end of the 28-day simulation as the particles are flushed to Bass Strait, or dispersed throughout the remainder of the bay, becoming increasingly unlikely to encounter the entrainment zone of the FSRU over time. The water on the mudflats in the north of the Bay drains slowly compared the other zones in the North Arm so the entrainment percentage continues to increase rather than asymptote over the 28-day simulation period.

Dispersion of particles through the remainder of the bay, including loss to the ocean (which is highest for areas nearer to the entrance to the bay) are the dominant mechanisms for loss of particles from each of the zones.

A second 28-day entrainment simulation undertaken for winter predicted very similar entrainment rates as the spring results, shown in the sensitivity analysis of different release times and distributions.

The entrainment results need to be considered in the context of the biological cycles and life cycle of the populations as the 28-day timeframe considered may be longer than the time taken to renew populations. The biological context and implications of these model results are addressed in the marine risk assessment prepared by CEE.

Discharge Scenarios

Additional discharge scenarios were considered in this assessment. These included closed loop operation, ballast water discharges and the dilution of the discharges when an LNG vessel is moored next to the FSRU. The outcomes of these scenarios are described in Chapters 6 to 8.

CONTENTS

1 Project Description 1

1.1 Proposed Crib Point LNG Facility 1
1.2 Floating Storage Regasification Unit (FSRU) 2
1.3 Project Objectives 5

2 Hydrodynamic Model 6

2.1 Model Description 6
2.1.1 Previous Models 6
2.1.2 Model Requirements 7
2.1.3 AEM3D 8
2.2 Model Set-up 10
2.2.1 Bathymetry 10
2.2.2 Meteorological Inputs 12
2.2.3 Oceanographic Inputs 13
2.2.4 Simulations Periods 14
2.3 Model Performance 18
2.3.1 ADCP Data 18
2.3.2 Model Calibration 19
2.3.3 Modelled Surface Heights 20
2.3.4 Modelled Currents 22
2.3.5 Correlation with Observed Currents 32

3 FSRU Cool Water Discharge 35

3.1 Model Set-up 35
3.1.1 Description of Discharge 35
3.1.2 Near Field Modelling of Plumes 35
3.1.3 Far Field Modelling of Plumes 36
3.2 Model Results 38
3.2.1 Behaviour of the Discharge Plume 38
3.2.2 Peak FSRU Discharge 51
3.2.3 Average FSRU Discharge 55
3.3 Temperature Outcomes 58

4 FSRU Chlorine Discharge 59

4.1 Model Set-up 59
4.2 Model Results 59
4.2.1 Peak FSRU Discharge 59
4.2.2 Average FSRU Discharge 62
4.3 Chlorine Outcomes 66

5 FSRU Intake of Plankton 67

5.1 Model Set-up 67
5.1.1 Particle Release 67
5.1.2 Particle Entrainment into FSRU Intake 69
5.2 Model Results 70
5.2.1 FSRU Entrainment 70
5.3 Outcomes for Entrainment 83

6 Closed Loop Operation 84

6.1 Scenario Descriptions 84
6.2 Closed Loop Peak Discharge Results 84
6.3 Closed Loop 2/3 Discharge Results 87
6.4 Additional West Rear Discharge Results 88

7 Ballast Water Discharge 94

7.1 Scenario Description 94
7.2 Ballast Water Discharge Results 94

8 LNG Unloading Scenarios 96

8.1 Scenario Descriptions 96
8.2 Open Loop Peak Production 97
8.3 Open Loop 2/3 Production 103
8.4 Open Loop 1/3 Production 108
8.5 Open Loop, Peak Production, West Facing Ports 109
8.6 Closed Loop East and West Rear Discharge 112
8.7 Closed Loop 2/3 Production 117
8.8 Closed Loop 1/3 Production 119

9 Assumptions, Limitations and Model Sensitivity 122

9.1 Assumptions and Limitations 122
9.2 Model Sensitivity 123
9.2.1 FSRU Discharge 123
9.2.2 FSRU Intake 129

10 Conclusions 133

10.1 Temperature Outcomes 133
10.2 Chlorine Outcomes 134
10.3 FSRU Entrainment 135
10.4 Model Sensitivity 136
10.5 Discharge Scenarios 136

11 References 137

FIGURES

Figure 1.1 Satellite image of Western Port Bay (source: Worldwind). 2

Figure 1.2 Arial image of Crib Point Jetty (source: Bing). 2

Figure 1.3 Conceptual image of discharge plume trajectory (source CEE). Water depth is approximately 15 m at slack tide. 4

Figure 1.4 Example of monthly gas production rate (source CEE). 4

Figure 2.1 AEM3D bathymetry showing extent of 50 x 50 m, 200 x 200 and 500 x 500 m sections of the model grid. 11

Figure 2.2 Depth contours from the 50 x 50 m resolution grid at Crib Point. 11

Figure 2.3 Wind rose at Crib Point from ACCESS wind maps, November 2018 to April 2019. 12

Figure 2.4 Wind rose in the northwest of WPB from ACCESS wind maps, November 2018 to April 2019. 13

Figure 2.5 Wind rose at Rhyll from ACCESS wind maps, November 2018 to April 2019. 13

Figure 2.6 Sea-level at the ocean boundary during March-April 2019. The bottom panel illustrates the low frequency sea level changes by way of a 14-day moving average of the data above. 14

Figure 2.7 Wind roses for selected simulation periods. 15

Figure 2.8 Sea level at the model boundary for selected simulation periods. 16

Figure 2.9 24-hour running mean of sea level at the model boundary for selected simulation periods. 17

Figure 2.10 ADCP locations (RHDHV, 2019) 18

Figure 2.11 Comparison between observed (blue) and modelled (red) surface heights at West ADCP 1 (West). 20

Figure 2.12 Comparison between observed (blue) and modelled (red) surface heights at middle ADCP 2 (Middle). 21

Figure 2.13 Comparison between observed (blue) and modelled (red) surface heights at East ADCP 2 (East). 22

Figure 2.14 Comparison between observed (blue) and modelled (red) north and east current vectors at ADCP 1 (West). 24

Figure 2.15 Comparison between observed (blue) and modelled (red) north and east current vectors at ADCP 2 (Middle). 25

Figure 2.16 Comparison between observed (blue) and modelled (red) north and east current vectors at ADCP 3 (East). 26

Figure 2.17 Observed (left) and modelled (right) current roses at ADCP 1 (West) at (from top to bottom of page) 9, 5 and 2 m above the seabed. 27

Figure 2.18 Observed (left) and modelled (right) current roses at ADCP 2 (Middle) at (from top to bottom of page) 9, 5 and 2 m above the seabed. 28

Figure 2.19 Observed (left) and modelled (right) current roses at ADCP 3 (East) at (from top to bottom of page) 9, 5 and 2 m above the seabed. 29

Figure 2.20 Comparison between observed (blue) and modelled (red) 50^{th} (left column) and 75^{th} (right column) percentile ebb and flood velocity vectors at ADCP 1 (West) at (from top to bottom of page) 9, 5 and 2 m above the seabed. 30

Figure 2.21 Comparison between observed (blue) and modelled (red) 50th (left column) and 75th (right column) percentile ebb and flood velocity vectors at all ADCP locations at (from top to bottom of page) 9, 5 and 2 m above the seabed. 31

Figure 2.22 A cross-section west to east of the simulated northward current during ebb (top panel) and flood (centre panel) tide, and the 24 h mean northward current (bottom panel, note smaller range of contour values). Approximate locations of ADCPs are indicated by dotted vertical lines. 32

Figure 2.23 Least squares linear fits observed and modelled north and east current vectors at all three ADCP locations. 34

Figure 3.1 Model cell locations selected for plume input in far-field model. Each cell is 20 x 20 m in size. 38

Figure 3.2 Modified lateral plume position as a function of ambient velocity. 38

Figure 3.3 A cross-section west to east of the simulated temperature anomaly during high tide (sea level and northward current are shown in top time series panel, with circle indicating timing of cross-section; location of FSRU indicated by dashed line in cross-section). 39

Figure 3.4 A cross-section north to south of the simulated temperature anomaly during high tide (sea level and northward current are shown in top time series panel, with circle indicating timing of cross-section; location of FSRU indicated by dashed line in cross-section). 40

Figure 3.5 A plan view of the simulated temperature anomaly at 7 m below sea level during high tide (sea level is shown in top time series panel, with circle indicating timing of plan view). 41

Figure 3.6 A plan view of the simulated temperature anomaly at the seabed during high tide (sea level is shown in top time series panel, with circle indicating timing of plan view). 42

Figure 3.7 A cross-section west to east of the simulated temperature anomaly during falling tide (sea level and northward current are shown in top time series panel, with circle indicating timing of cross-section; location of FSRU indicated by dashed line in cross-section). 43

Figure 3.8 A cross-section north to south of the simulated temperature anomaly during falling tide (sea level and northward current are shown in top time series panel, with circle indicating timing of cross-section; location of FSRU indicated by dashed line in cross-section). 43

Figure 3.9 A plan view of the simulated temperature anomaly at 7 m below sea level during falling tide (sea level is shown in top time series panel, with circle indicating timing of plan view). 44

Figure 3.10 A plan view of the simulated temperature anomaly at the seabed during falling tide (sea level is shown in top time series panel, with circle indicating timing of plan view). 45

Figure 3.11 A cross-section west to east of the simulated temperature anomaly during low tide (sea level and northward current are shown in top time series panel, with circle indicating timing of cross-section; location of FSRU indicated by dashed line in cross-section). 46

Figure 3.12 A cross-section north to south of the simulated temperature anomaly during falling tide (sea level and northward current are shown in top time series panel, with circle indicating timing of cross-section; location of FSRU indicated by dashed line in cross-section). 46

Figure 3.13 A plan view of the simulated temperature anomaly at 7 m below sea level during low tide (sea level is shown in top time series panel, with circle indicating timing of plan view). . 47

Figure 3.14 A plan view of the simulated temperature anomaly at the seabed during low tide (sea level is shown in top time series panel, with circle indicating timing of plan view). 48

Figure 3.15 A cross-section west to east of the simulated temperature anomaly during rising tide (sea level and northward current are shown in top time series panel, with circle indicating timing of cross-section; location of FSRU indicated by dashed line in cross-section). 49

Figure 3.16 A cross-section north to south of the simulated temperature anomaly during rising tide (sea level and northward current are shown in top time series panel, with circle indicating timing of cross-section; location of FSRU indicated by dashed line in cross-section). 49

Figure 3.17 A plan view of the simulated temperature anomaly at 7 m below sea level during rising tide (sea level is shown in top time series panel, with circle indicating timing of plan view). 50

Figure 3.18 A plan view of the simulated temperature anomaly at the seabed during rising tide (sea level is shown in top time series panel, with circle indicating timing of plan view). 51

Figure 3.19 10th percentile of temperature change at the seabed over a 28-day simulation at peak FSRU discharge. 52

Figure 3.20 5th percentile of temperature change at the seabed over a 28-day simulation at peak FSRU discharge. 53

Figure 3.21 Time series of sea level (top panel) and (running down the page) temperature reduction at the seabed below the plume and north, south, west and east of the FSRU during peak discharge. 54

Figure 3.22 24-hr moving average time series of sea level (top panel) and (running down the page) temperature reduction at the seabed below the plume and north, south, west and east of the FSRU during peak discharge. 55

Figure 3.23 5th percentile of temperature change at the seabed over a 28-day simulation at average FSRU discharge. 56

Figure 3.24 Time series of sea level (top panel) and (running down the page) temperature reduction at the seabed below the plume and north, south, west and east of the FSRU during average discharge. 57

Figure 4.1 50th percentile of chlorine concentration at the seabed during over a 28-day simulation at peak FSRU discharge. 60

Figure 4.2 95th percentile of chlorine concentration at the seabed during over a 28-day simulation at peak FSRU discharge. 60

Figure 4.3 Time series of sea level (top panel) and (running down the page) chlorine concentration at the seabed below the plume and north, south, west and east of the FSRU during peak discharge. 61

Figure 4.4 24-hr moving average time series of sea level (top panel) and (running down the page) chlorine concentration at the seabed below the plume and north, south, west and east of the FSRU during peak discharge. 62

Figure 4.5 50th percentile of chlorine concentration at the seabed during over a 28-day simulation at average FSRU discharge. 63

Figure 4.6 95th percentile of chlorine concentration at the seabed during over a 28-day simulation at average FSRU discharge. 64

Figure 4.7 24-hr moving average time series of sea level (top panel) and (running down the page) chlorine concentration at the seabed below the plume and north, south, west and east of the FSRU during average discharge. 65

Figure 5.1 Particle release zones based on description from CEE (pers. comms, 2019). 68

Figure 5.2 Distribution of Zone 2 particles over 25 days. 69

Figure 5.3 Percentage of particles entrained during 28 days at peak intake (maximum percentage from scenarios is shown here). The average for North Arm at peak production is approximately 0.38 % per 28 days. 73

Figure 5.4 Percentage of particles entrained during 28 days at annual average intake (maximum percentage from scenarios is shown here). The average for North Arm at average production is approximately 0.26 % per 28 days. 74

Figure 5.5 Fate of Zone 2 particles over 28 days (top: percentage entrained; centre: percentage leaving to Bass Strait; bottom: percentage remaining in zone region). 75

Figure 5.6 Fate of Zone 3 particles over 28 days: percentage entrained into FSRU (top); percentage leaving to Bass Strait (middle); and percentage remaining in zone (bottom). 76

Figure 5.7 Fate of Zone 5 particles over 28 days: percentage entrained into FSRU (top); percentage leaving to Bass Strait (middle); and percentage remaining in zone (bottom). 77

Figure 5.8 Fate of Zone 6 particles over 28 days: percentage entrained into FSRU (top); percentage leaving to Bass Strait (middle); and percentage remaining in zone (bottom). 78

Figure 5.9 Fate of Zone 7 particles over 28 days: percentage entrained into FSRU (top); percentage leaving to Bass Strait (middle); and percentage remaining in zone (bottom). 79

Figure 5.10 Fate of Zone 8 particles over 28 days: percentage entrained into FSRU (top); percentage leaving to Bass Strait (middle); and percentage remaining in zone (bottom). 80

Figure 5.11 Fate of Zone 9 particles over 28 days: percentage entrained into FSRU (top); percentage leaving to Bass Strait (middle); and percentage remaining in zone (bottom). 81

Figure 5.12 Fate of Zone 10 particles over 28 days: percentage entrained into FSRU (top); percentage leaving to Bass Strait (middle); and percentage remaining in zone (bottom). 82

Figure 6.1 Plan view of location of warm water discharge from FSRU (blue square). The dark outlines indicate the location of the FSRU vessel. 84

Figure 6.2 Plan view of mean chlorine concentration in the water column (highest for all depths) for a 28-day closed loop peak discharge simulation. 85

Figure 6.3 Plan view of 95th percentile chlorine concentration in the water column (highest for all depths) for a 28-day closed loop peak discharge simulation. 86

Figure 6.4. Plan view of mean chlorine concentration in the water column (highest over all depths) for a 28-day closed loop 2/3 discharge simulation. 87

Figure 6.5 Plan view of 95th percentile chlorine concentration in the water column (highest over all depths) for a 28-day closed loop 2/3 discharge simulation. 88

Figure 6.6 Plan view of 5th percentile of temperature change in the water column (highest for all depths) for a 28-day closed loop east and west rear discharge simulation. 89

Figure 6.7 Plan view of mean chlorine concentration in the water column (highest for all depths) for a 28-day closed loop east and west rear discharge simulation. 89

Figure 6.8 Plan view of 95th percentile chlorine concentration in the water column (highest for all depths) for a 28-day closed loop east and west rear discharge simulation. 90

Figure 6.9 Time series of sea level (top panel) and (running down the page) temperature reduction at the seabed below the plume and north, south, west and east of the FSRU during closed loop east and west rear discharge. 91

Figure 6.10 Time series of sea level (top panel) and (running down the page) chlorine concentration at the seabed below the plume and north, south, west and east of the FSRU during closed loop east and west rear discharge. 92

Figure 6.11 24-hr moving average time series of sea level (top panel) and (running down the page) chlorine concentration at the seabed below the plume and north, south, west and east of the FSRU during closed loop east and west rear discharge. 93

Figure 7.1 Plan view of location of ballast water discharge from FSRU (blue square). The dark outlines indicate the location of the FSRU vessel. 94

Figure 7.2 Plan view of 95th percentile of highest chlorine concentration in the water column (i.e. over all depths) for a 28-day ballast water discharge simulation. 95

Figure 8.1 Plan view of location of heat exchanger discharge from FSRU (blue squares) for configuration peak (left), 2/3 and 1/3 (right) open loop production. The dark outlines indicate the location of the FSRU and neighbouring vessel. 97

Figure 8.2 Plan view of 5th percentile of temperature decrease at the seabed for a 28-day open loop peak production simulation with neighbouring vessel configuration. 98

Figure 8.3 Plan view of mean (top) and 95th percentile (bottom) chlorine concentration at the seabed for a 28-day open loop peak production simulation with neighbouring vessel. 99

Figure 8.4 Time series of sea level (top panel) and (running down the page) temperature reduction at the seabed below the plume and north, south, west and east of the FSRU during peak discharge simulation with neighbouring vessel. 100

Figure 8.5 Time series of sea level (top panel) and (running down the page) chlorine concentration at the seabed below the plume and north, south, west and east of the FSRU during peak discharge simulation with neighbouring vessel. 101

Figure 8.6 24-hr moving average time series of sea level (top panel) and (running down the page) chlorine concentration at the seabed below the plume and north, south, west and east of the FSRU during peak discharge simulation with neighbouring vessel. 102

Figure 8.7 Plan view of 5th percentile of temperature decrease at the seabed for a 28-day open loop 2/3 production simulation with neighbouring vessel. 103

Figure 8.8 Plan view of mean (top) and 95th percentile (bottom) chlorine concentration at the seabed for a 28-day open loop 2/3 production simulation with neighbouring vessel. 104

Figure 8.9 Time series of sea level (top panel) and (running down the page) temperature reduction at the seabed below the plume and north, south, west and east of the FSRU during average discharge simulation with neighbouring vessel. 105

Figure 8.10 Time series of sea level (top panel) and (running down the page) temperature reduction at the seabed below the plume and north, south, west and east of the FSRU during average discharge simulation with neighbouring vessel. 106

Figure 8.11 24-hr moving average time series of sea level (top panel) and (running down the page) chlorine concentration at the seabed below the plume and north, south, west and east of the FSRU during average discharge simulation with neighbouring vessel. 107

Figure 8.12 Plan view of 5th percentile of temperature decrease at the seabed for a 28-day open loop 1/3 production simulation with neighbouring vessel. 108

Figure 8.13 Plan view of mean (top) and 95th percentile (bottom) chlorine concentration at the seabed for a 28-day open loop 1/3 production simulation with neighbouring vessel. 109

Figure 8.14 Plan view of 5th percentile of temperature decrease at the seabed for a 28-day open loop peak production simulation with discharge from west side of FSRU and neighbouring vessel configuration. 110

Figure 8.15 Plan view of mean (top) and 95th percentile (bottom) chlorine concentration at the seabed for a 28-day open loop peak production simulation with discharge from west side of FSRU and neighbouring vessel. 111

Figure 8.16 Plan view of 5th percentile of temperature change in the water column (highest from all depths) for a 28-day closed loop east and west rear discharge simulation with neighbouring vessel. 112

Figure 8.17 Plan view of mean chlorine concentration in the water column (highest from all depths) for a 28-day closed loop east and west rear discharge simulation with neighbouring vessel. 113

Figure 8.18 Plan view of 95th percentile chlorine concentration in the water column (highest from all depths) for a 28-day closed loop east and west rear discharge simulation with neighbouring vessel. 113

Figure 8.19 Time series of sea level (top panel) and (running down the page) temperature reduction at the seabed below the plume and north, south, west and east of the FSRU during closed loop east and west rear discharge with neighbouring vessel. 114

Figure 8.20 Time series of sea level (top panel) and (running down the page) chlorine concentration at the seabed below the plume and north, south, west and east of the FSRU during closed loop east and west rear discharge with neighbouring vessel. 115

Figure 8.21 24-hr moving average time series of sea level (top panel) and (running down the page) chlorine concentration at the seabed below the plume and north, south, west and east of the FSRU during closed loop east and west rear discharge simulation with neighbouring vessel. 116

Figure 8.22 Plan view of mean (top) and 95th percentile (bottom) chlorine concentration in the water column (i.e. over all depths) for a 28-day closed loop 2/3 production simulation with neighbouring vessel. 118

Figure 8.23 Plan view of mean (top) and 95th percentile (bottom) chlorine concentration in the water column (i.e. over all depths) for a 28-day closed loop 1/3 production simulation with neighbouring vessel. 120

Figure 8.24 Plan view of mean (top) and 95th percentile (bottom) chlorine concentration in the water column (i.e. over all depths) from ballast and closed loop discharges for a 28-day closed loop 1/3 production simulation with neighbouring vessel. 121

Figure 9.1 Timeseries of current at the FSRU ports (top panel), temperature reduction at sites at and north of FSRU (second panel), temperature reduction at sites at and south of FSRU (third panel) and temperature reduction at sites at and east of the FSRU during peak discharge for three different model configurations. 124

Figure 9.2 -0.3 ºC contour of 5th percentile of temperature decrease at the seabed during over a 28-day simulations at peak FSRU discharge. Simulation P is shown in dark blue..... 125

Figure 9.3 -0.5 ºC contour of 5th percentile of temperature decrease at the seabed during over a 28-day simulations at peak FSRU discharge. Simulation P is shown in dark blue..... 126

Figure 9.4 -0.3 ºC contour of 5th percentile of temperature decrease at the seabed during over a 28-day simulation at average FSRU discharge. Simulation P is shown in dark blue. 127

Figure 9.5 -0.5 ºC contour of 5th percentile of temperature decrease at the seabed during over a 28-day simulation at average FSRU discharge. Simulation P is shown in dark blue. 128

Figure 9.6 Entrainment of particles over 28 days from Zone 2 (top); Zone 3 (middle); Zone 7 (bottom) for different model hydrodynamics (colours) and different release times (solid, dashed and dotted lines are for initial conditions of uniform surface distribution on rising tide, mixed distribution on rising tide and mixed distribution on falling tide, respectively) 130

Figure 9.7 Entrainment of particles over 28 days from Zone 2 (top); Zone 3 (middle); Zone 7 (bottom) for different model set-up (colours) and different release times (solid, dashed and dotted lines are for initial conditions of uniform surface distribution on rising tide, mixed distribution on rising tide and mixed distribution on falling tide, respectively)..... 132

TABLES

Table 3.1 Near-field Prediction of Plume Extent and Temperature Difference. 36
Table 3.2 Initial footprint in 20 x 20 m far-field model (north-south extent is 60 m for 4-port case) 37
Table 5.1 Dimensions of entrainment zone from the FSRU sea chest. Vertical distances are from the surface, lateral distances are from the side of the vessel. 70
Table 5.2 Percentage of particles entrained during 28 days at peak and annual average intake (maximum percentage from scenarios is shown here)..... 72

APPENDICES

Appendix A Hydrodynamic Model

Appendix B FSRU Discharge Modelling

Appendix C FSRU Intake Modelling

GLOSSARY

ACCESS	The Australian Community Climate and Earth-System Simulator weather models that have been developed by the Bureau of Meteorology.
ADCP	Acoustic Doppler Current Profiler is a hydroacoustic current meter used to measure water velocity and direction.
AEM3D	Aquatic Ecosystem Model 3D. Three-dimensional model for simulating hydrodynamics and water quality in surface water.
Bass Strait	Bass Strait is the sea strait separating Tasmania from Victoria on the Australian mainland.
Bathymetry	Mapping of the sea floor depths.
Boundary Conditions	Environmental conditions (e.g. oceanographic and meteorological) at the edges or surface of a model domain.
FSRU	Floating Storage and Regassification Unit. Liquefied Natural Gas (LNG) storage ship that has an onboard regassification plant capable of returning LNG back into a gaseous state and then supplying it directly into the gas network.
OceanMAPS	Ocean Modelling, Analysis, and Prediction System. Australia's operational ocean forecast system developed by the Bureau of Meteorology.
OTIS	Oregon State University Tidal Inversion Software used to generate tidal series.
North Arm	Channel of Western Port Bay between the west coast and French Island that runs north from Sandy Point, past Crib Point, to the bend in the channel near Chinaman Island.
Sea Chest	Sea chests are gratings that are located underwater on the hull of a ship used to draw in water.
Slack Tide	Slack water is a short period in a body of tidal water when there is no movement before the direction of the tidal stream reverses.
Tidal Excursion	Horizontal distance a particle moves during one tidal cycle of ebb and flow.
WPB	Western Port Bay

1 Project Description

1.1 Proposed Crib Point LNG Facility

Western Port Bay (WPB) is an embayment on the coast of southern Victoria. The Bay consists of a complex series of deep channels, intertidal flats and two large islands - French Island in the north and Phillip Island to the south (see Figure 1.1). Exchange of seawater between the Bay and Bass Strait is through a wide western entrance at Flinders and a small entrance between Phillip Island and San Remo.

AGL Wholesale Gas Ltd (AGL) is assessing the feasibility of mooring a Floating Storage and Regasification Unit (FSRU) at Crib Point Jetty in the north arm of Western Port Bay to supply Liquefied Natural Gas (LNG) to its customers in south-eastern Australia (see Figure 1.2). The Crib Point Jetty has been selected by AGL as the preferred location for a continuously moored FSRU because it is an established port with existing jetty infrastructure and close to the Victorian gas network.

At peak production rate the FSRU heat-exchange process will extract up to 468,000 m^3 of seawater per day from WPB though sea chests on the port and starboard side of the vessel. The seawater will pass through heat exchangers before being discharged back to the bay at up to 7 ^oC cooler via 6 ports on the starboard side (CEE, 2018a).

The discharge will create a plume that is cooler, and therefore of higher density, than the surrounding seawater. During periods of low currents, the plume is expected to descend to the seabed at a lateral distance of approximately 60 m from the discharge ports (CEE, 2018a). The extent of the plume at the seabed will depend on the momentum of the discharge exiting the ports and the transport and mixing imparted by the ambient flow (northward during flood tide and southward during ebb tide) as the dense plume descends under the action of gravity.

There are three heat exchangers on the FSRU, each with two ports, so depending on the rate of gas production, two, four or six ports will be operating concurrently, This report considers the effects at peak production rates (discharge of 468,000 m^3/day, i.e. 5.4 m^3/s) and average production rates (discharge of 312,000 m^3/day, i.e. 3.6 m^3/s).

The seawater is chlorinated by electrolysis of the inflowing seawater to control fouling in the pumps, pipes and heat exchangers. On discharge, the residual chlorine concentration will be 100 µg/L or lower.

Hydronumerics was commissioned to assist with an assessment of the potential impact on the marine environment associated with the seawater intake seawater and discharge seawater discharge, during operation of the FSRU. The objectives of this assessment are to:

- Assess the extent of the plume of cooler water seawater on the sea floor;
- Assess the distribution of residual chlorine in the discharged seawater; and
- Assess the extent of entrainment of larvae released from various points in WPB into the FSRU.

Figure 1.1 Satellite image of Western Port Bay (source: Worldwind).

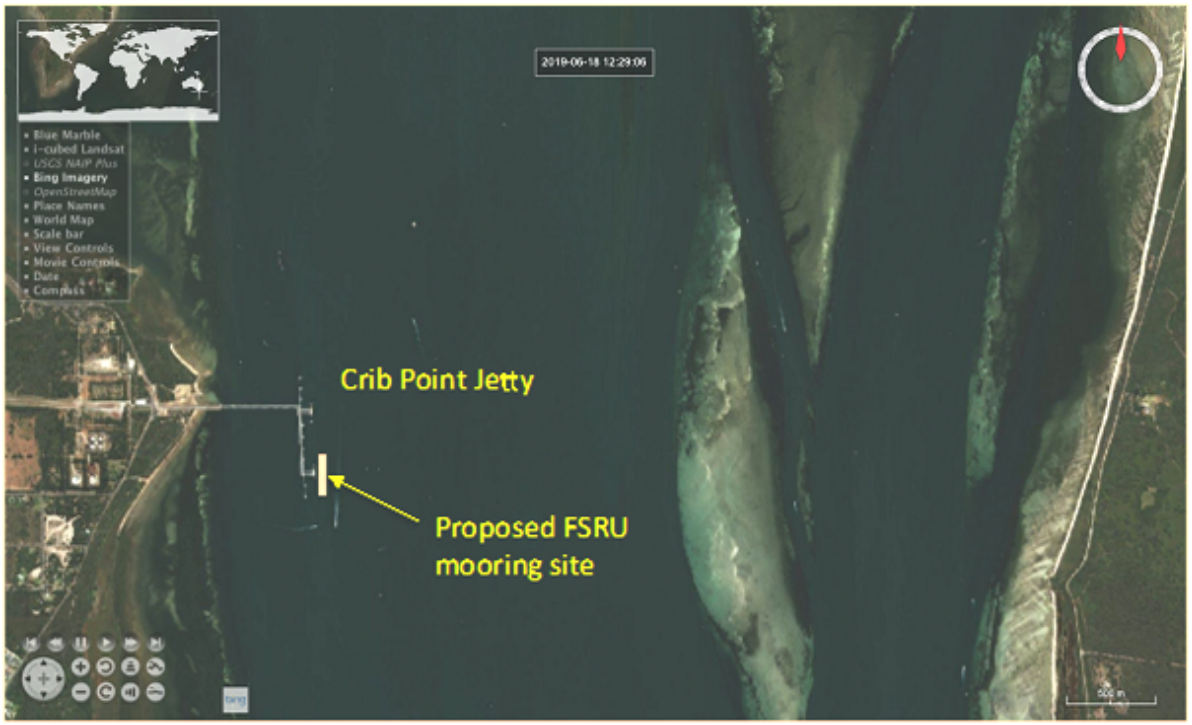

Figure 1.2 Arial image of Crib Point Jetty (source: Bing)

1.2 Floating Storage Regasification Unit (FSRU)

The FSRU vessel will be approximately 300 m long and 46 m wide and will be moored at Berth 2 at the southern end of the Crib Point jetty (Figure 1.2) with the bow of the vessel facing north.

The FSRU has an estimated draught of 9.3 m in ballast conditions and 11.6 m in loaded conditions. The water depth is 13 m at LAT, so that the hull will be approximately 2.4 m above the seabed at low tide.

At maximum operational capacity, 468,000 m^3/d of seawater will be drawn from WPB via sea chests on the port (western) and starboard (eastern) side of the vessel. Intake water will pass through heat exchangers before being discharged back to the bay at approximately 7 ^oC cooler than intake temperature. The discharge will exit via 6 ports on the starboard side, each port having a diameter of 0.45 m, spaced a minimum of 10 m apart, and located at approximately 2 m below sea level. The discharge velocity at each port will be approximately 5.7 m/s.

The discharge will create up to six separate plumes that are cooler, and therefore of higher density, than the surrounding seawater. During low currents the plume is expected to fall to the seabed at a lateral distance of approximately 60 m from the discharge ports (CEE, 2018a). The extent of decrease in temperature at the seabed and the temporal and spatial pattern of the decrease will depend on the momentum of the discharge exiting the ports and the transport and mixing imparted by the ambient flow (northward during flood tide and southward during ebb tide) as the dense plume descends under the action of gravity (Figure 1.3).

There are three heat exchangers (regasification units) on the FSRU, each with two ports so, depending on the level of gas production, two, four or six ports will be operating concurrently. An example of the month-by-month gas production is shown in Figure 1.4 below. Peak gas production, and hence peak seawater intake and discharge, will occur in the two winter months when six ports discharge a total of 468,000 m^3/day (5.4 m^3/s). Over the year, the average intake and discharge is equivalent to about four discharge ports at a total discharge of 312,000 m^3/day (3.6 m^3/s).

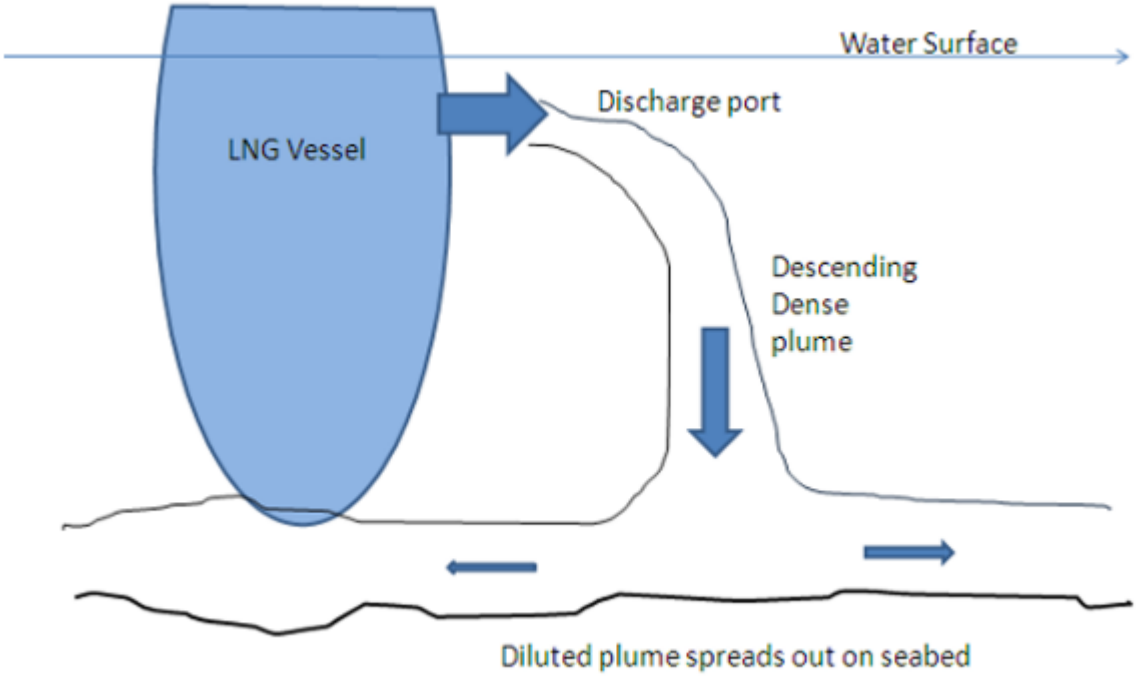

Figure 1.3 Conceptual image of discharge plume trajectory (source CEE). Water depth is approximately 15 m at slack tide.

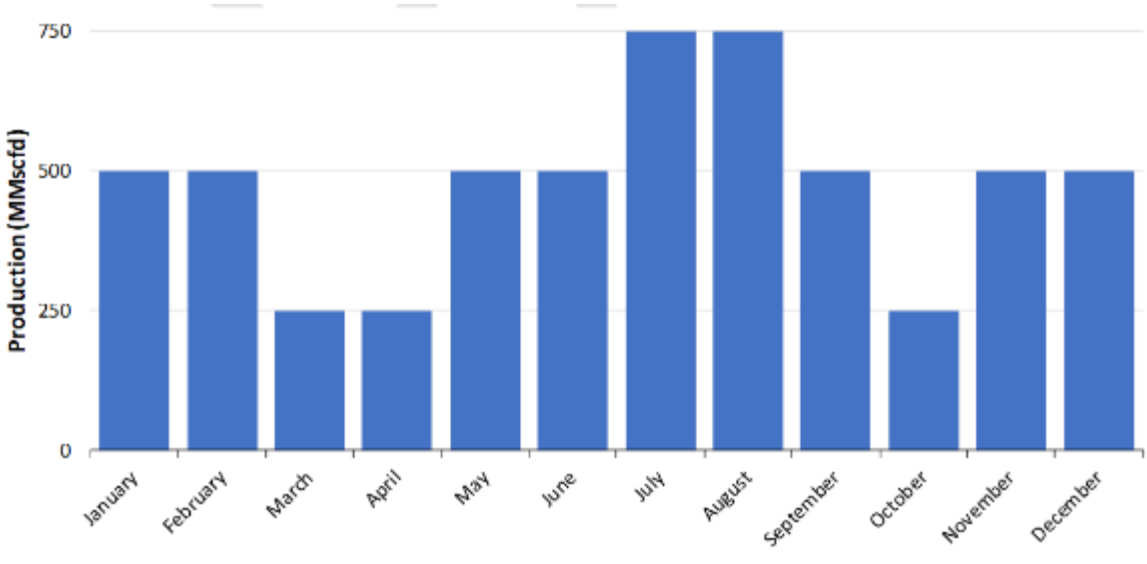

Figure 1.4 Example of monthly gas production rate (source CEE).

1.3 Project Objectives

Hydronumerics was commissioned to assist with an assessment of the potential impact on the marine environment associated with the seawater intake and discharge during operation of the FSRU. This report describes the development and application of a hydrodynamic model of WPB (described in Chapter 2) that has been applied to quantify the following:

- The potential extent of the plume of cooler seawater on the sea floor (see Chapter 3);
- The distribution of residual chlorine in the discharged seawater (see Chapter 4); and
- The extent of entrainment of larvae released from various points in WPB (see Chapter 5).

To undertake these assessments, a three-dimensional model of the whole of WPB was applied. An existing Aquatic Ecosystem Model 3D (AEM3D) model of WPB that was previously developed for Melbourne Water and EPA Victoria was modified and applied in the project.

2 Hydrodynamic Model

2.1 Model Description

2.1.1 Previous Models

WPB has been studied extensively since the 1970's, with a number of these studies supported by numerical models focused on a range of processes including circulation, sediment transport, catchment inputs, water quality, algal production, seagrass meadows and mangrove habitats. A brief overview of the models, or components of models, that account for the hydrodynamic processes occurring in the bay is presented below. These previous modelling studies provide some guidance as to the required attributes of a fit-for-purpose model for this project, which is discussed in the section that follows.

Early two-dimensional models by Hinwood and O'Brien (1974) and Hinwood (1979) showed that residual tidal motion circulates around French Island converging at a tidal divide in the northeast corner of the bay. The addition of prevailing winds to the model produced net eastward currents and an overall residual circulation that was clockwise around French Island with flow entering and exiting primarily through the western entrance to Bass Strait. Whilst the coarse grid of the model was sufficient for understanding general circulation, Hinwood (1979) indicated that finer model grids (down to 100 m) were required to improve model capability for the bay.

Other two-dimensional models developed in the decades that followed had either a coarse grid, and were focused on the fate of sediment loads into the bay (e.g. Hancock et al. 2001, Wallbrink et al. 2003, Hughes et al. 2003), or were applied to investigate specific issues such as shipping (Lee, 2011).More recent applications of two-dimensional depth-averaged models include higher resolution simulations of the full bay down to 50-100 m grid scales in the navigation and port areas (Symonds et al. 2016). The commercially available models tested by Symonds et al. (2016), whilst different in terms of numerical solution and grid structure, predicted consistent hydrodynamic conditions that agreed well with measured data.

Two-dimensional models are usually considered adequate for representing circulation in well-mixed and rapidly flushed environments like WPB. However, during the drought conditions from 1998 to 2011, salinity increased as high as 40 psu (Practical Salinity Units) in the northern tidal mudflats of WPB (Lee, 2011) so model development shifted in focus to the inclusion of processes of atmospheric heat exchange, evaporation and three-dimensional representation of stratified flow that is necessary to model density gradients. Harrison et al. (2011) applied three-dimensional models with grids of varied lateral resolution and six vertical layers. Whilst coarse grids of 400 m were used for long-term simulations of whole-of-bay circulation, grids at this scale provided only limited detail about the complexities of the flow within each of the sections of the bay.

A hydrodynamic model was developed to determine the impact of port design scenarios for the preliminary business case investigations of part of Infrastructure Victoria's Second Container Port Advice (Cardno, 2017). The model used the FLOW module of the Delft3D modelling system developed by Deltares of The Netherlands, which included a robust and efficient wetting and drying algorithm. This is particularly important for Western Port where there are extensive mangroves and intertidal areas.

More recent three-dimensional models of the whole of the bay have been applied with increased grid resolution (down to 50 m over tidal flats and channels in the northern sections of the bay) to simulate general circulation, sediment transport from catchments and bed load, light environment over seagrass meadows and mangrove seed dispersion (Hydronumerics, 2016, Cinque et al. 2018, and Hurst 2018).

A key finding relevant to this study is the role that variations in wind field over the expanse of WPB have on the hydrodynamics and circulation. The selection of meteorological recordings from one station over another as model boundary conditions leads to notably different results in terms of net circulation.

2.1.2 Model Requirements

The features required of a hydrodynamic model to ensure its suitability for this project fall into two categories:

1. Requirements for modelling hydrodynamics; and
2. Requirements for modelling project elements.

Findings from previous modelling studies, coupled with the parameters of this project lead to a list of features that a hydrodynamic model should have to be fit-for-purpose for this assessment. The features fall into two categories. Firstly, there are those that are required to adequately simulate the hydrodynamics with sufficient detail. The first category includes whole-of-bay circulation and detail in the project area at Crib Point, where the localised impacts of the FSRU are likely to be observed. The second category focuses on the attributes required to adequately incorporate the project elements and how they interact with the background hydrodynamics. This includes the impacts of the discharge and the likely entrainment of biological constituents from various habitats around the bay. Some model requirements fit into both categories. Specifically, the requirements are as follows.

Requirements for modelling background hydrodynamics:

- Domain coverage that includes the entirety of the bay so the model can reproduce the complex and interconnected processes that govern circulation of water within the bay;
- Sufficient grid resolution to model flows that respond to complex bathymetric features such as the channels and tidal flats that make up a large portion of the bay. Importantly, this includes wetting and drying of shallow intertidal areas. Previous modelling suggested that grid resolutions of less than 400 m and down to 100 m are required to achieve this;
- Incorporating best available ocean boundary data, as this is the predominant forcing mechanism for bay hydrodynamics. This includes both tidal oscillations and atmospheric pressure-driven low frequency oceanographic oscillations; and
- Heterogeneous surface wind forcing to account for the known variability of the wind field over WPB in response to topography, which has been demonstrated in previous modelling studies.

Requirements for modelling project elements:

- Sufficient model grid resolution in the project area to account for the scale of the FSRU vessel, local bathymetric features and near-field plume propagation. These features have scales of less than 100 m;
- Capacity to model the influence of the FSRU vessel on local flow and the changing position of discharge ports (relative to the seabed) during rise and fall of the tide, and the loading of LNG and export of gas from the FSRU;
- Three-dimensional grid to account for near-field plunging and dispersion of negatively buoyant (cooler) FSRU discharge and potential formation of cool water pools during slack tides;
- Explicitly derived vertical mixing that responds to changes in ambient shear, and so diminishes mixing during slack tide when cool water pooling may occur. This is opposed to a two-dimensional model or application of a simplistic vertical diffusivity rate that is likely to under-predict the potential for cool water pooling; and
- Particle release and tracking to provide estimates of potential entrainment into the FSRU intake of biological constituents from different regions within the bay.

A previously developed Aquatic Ecosystem Model 3D (AEM3D) hydrodynamic model of WPB (Hydronumerics, 2016, Cinque et al. 2018 and Hurst 2018) was modified to simulate the FSRU intake and discharge at Crib Point.

Key model changes were to develop a finer resolution model grid at Crib Point and to apply spatially and temporally varying oceanographic and meteorological boundary conditions that were sourced from the Bureau of Meteorology's (BOM) OceanMAPS and ACCESS regional modelling platforms.

The model configuration included the simulation of the effects of the moored FSRU vessel on local currents and accounting for sub-grid scale near-field dilution of the FSRU discharge. To incorporate the latter, a separate discharge plume model (near-field model) was developed by CEE (2018a) and used to configure the initial dilution and travel path of the FSRU discharge in the WPB hydrodynamic model (the far-field model). The near-field plume model was required to account for processes of exit momentum from the discharge ports, ambient current during discharge and the descent under gravity that determine the location and dilution of the plume in the near-field (i.e. to 60 m from the ports).

2.1.3 AEM3D

The Aquatic Ecosystem Model 3D (AEM3D) is developed and distributed by Hydronumerics. AEM3D originates from the ELCOM-CAEDYM model developed by the Centre for Water Research, University of Western Australia (e.g. see Hodges et al. 2000, Dallimore et al. 2003, Romero et al. 2004, and Bothelo and Imberger 2007), which has been applied to numerous estuarine and oceanographic systems (e.g. Chan et al. 2002, Spillman et. al. 2007, Hillmer and Imberger 2007 and Silva et al. 2014). AEM3D is currently applied to WPB by Melbourne Water and previously by EPA Victoria. Whilst AEM3D includes comprehensive water quality modelling capabilities, only the hydrodynamics components have been utilised for this project.

The hydrodynamics component in AEM3D predicts velocity, temperature and salinity distribution in natural water bodies that are subjected to external forcing from the ocean (salinity, temperature, low-frequency oscillations, tides and waves), the atmosphere, surface

flows, groundwater flows and flows from built structures such as pipes and chutes. The simulation method solves the unsteady, viscous Navier-Stokes equations for incompressible flow using the hydrostatic assumption for pressure (Hodges et al. 2000). Simulated processes include baroclinic and barotropic responses, rotational effects, tidal forcing, wind stresses, thermal forcing, inflows, outflows, and transport of salt, heat and passive scalars. The hydrodynamic algorithms in AEM3D are based on the Euler-Lagrange method for advection of momentum with a conjugate-gradient solution for the free surface. Passive and active scalars (i.e. tracers, salinity and temperature) are advected using a conservative ULTIMATE QUICKEST scheme. The AEM3D code has been optimised for computational efficiency and operates on parallel cores, typically configured to have real to runtime ratios of between 100:1 and 1000:1 that are dependent on grid resolution and size.

Technical specifications and a description of the mixing model in AEM3D are provided in Appendix A.

For this project the model functionality includes:

- Modification of tidal phase and amplitude in response to bathymetric change and bed friction, including the wetting and drying of intertidal areas;
- Baroclinic flow driven by density gradients (i.e. salinity and temperature gradients) such as those between FSRU discharge and ambient waters of the bay;
- Conservative numerical tracers to track outfall plume fate and transport (including constituents added to the plume such as anti-fouling agents); and
- Lagrangian particle release and tracking to examine the extent of larvae entrainment from different regions within the bay.

2.2 Model Set-up

2.2.1 Bathymetry

WPB AEM3D modelling applications have previously focussed on whole-of-bay processes including residual circulation and sediment transport from and to the northern tidal flats. A new model bathymetry was developed for this project to provide an appropriate bathymetry resolution for simulating hydrodynamic processes and discharges around Crib Point. This included high-resolution bathymetric data from the project site, creating a variable lateral grid resolution with a focus on the area of interest, and establishing sufficient vertical grid spacing to resolve the processes associated with transport and mixing of the FSRU discharge.

The bathymetric datasets used to develop the model grid were:

- Victorian Coastline DEM (VCDEM) raster data at 10 m resolution from Spatial Systems CRC – used for depths shallower than 30 m AHD;
- Bass Strait Depth Zone Contour Lines (BSDZCL) from the 1:250,000 National Bathymetric Map Series from DELWP – used for depths greater than and equal to 30 m AHD; and
- Western Port DEM (WPDEM) raster data at 2.5 m resolution from Frontier SI (formerly Spatial Systems CRC) – used for Crib Point region.

The Victorian Regional Channels Authority (VRCA) provided a 0.5 m resolution bathymetric dataset for the region around Berth 2 at Crib Point Jetty. The data were interpolated to a 2 m grid and subtracted from the WPDEM to determine the differences in the datasets (see Appendix A). Longitudinal bands of 10-30 cm deficit or surfeit between the two grids became evident in the difference plot, perhaps due to regions where accretion or erosion has occurred between bathymetric surveys.

To generate the model bathymetry the VCDEM was cropped to include the coast from Cape Schanck to Cape Patterson and meshed with the BSDZCL data. This data was then used to generate a 50 x 50 m plaid model grid in the region around Crib Point, extending to 200 x 200 m then 500 x 500 m to the extent of the domain (see Figure 2.1). Contours of the model grid at Crib Point are illustrated in the Figure 2.2.

A second grid with 20 x 20 m spacing in the Crib Point region (in place of the 50 x 50 m grid portion), stepping out to 200 m for the remainder of the domain was also developed. This grid provided higher resolution around the project site for the purpose of the FSRU discharge

modelling assessments. Both model grids have z-coordinate systems with vertical resolution of 1 m in the project site and up to 8 m in the deeper regions of the bay entrance and Bass Strait. The computational efficiencies of these grids were 1:100 for the 50 x 50 m grid and 1:40 for the 20 x 20 m grid on an 8-core Intel 3.4GHz Linux desktop computer.

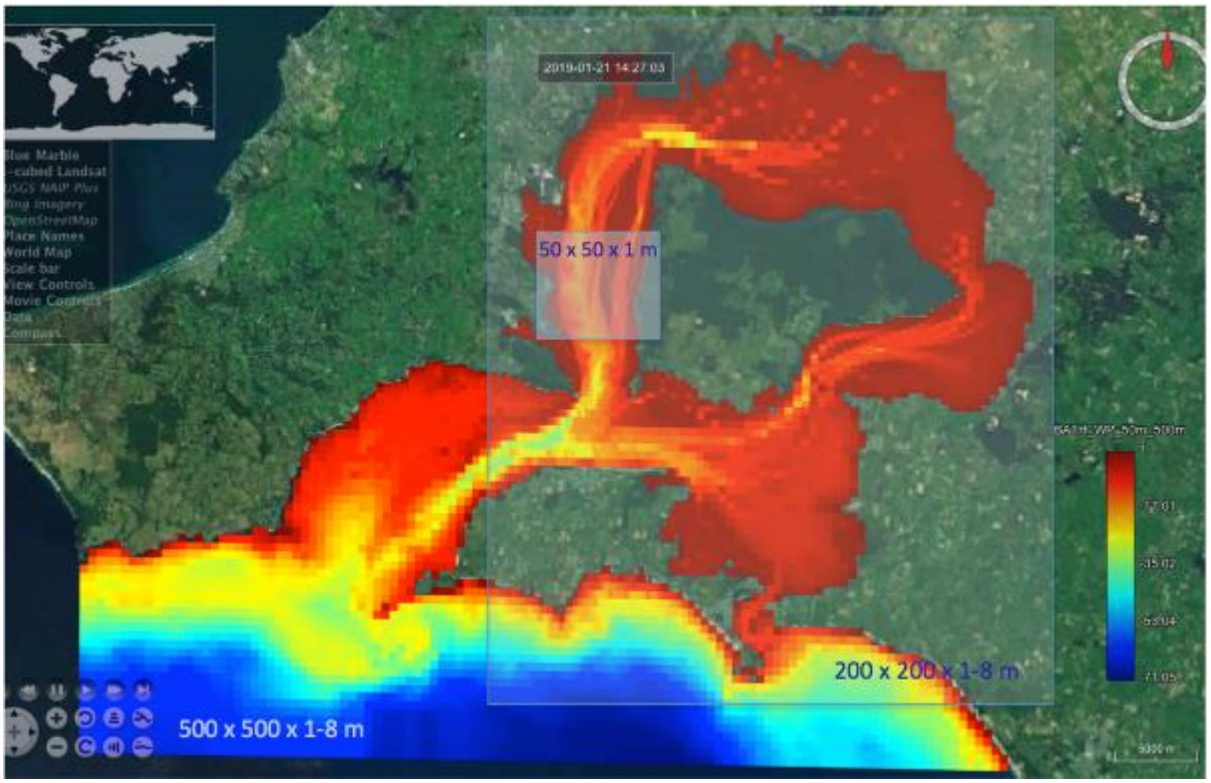

Figure 2.1 AEM3D bathymetry showing extent of 50 x 50 m, 200 x 200 and 500 x 500 m sections of the model grid.

Figure 2.2 Depth contours from the 50 x 50 m resolution grid at Crib Point.

2.2.2 *Meteorological Inputs*

The Australian Community Climate and Earth-System Simulator (ACCESS, see http://www.bom.gov.au/australia/charts/about/about_access.shtml) weather model outputs were used at a 1.5 km resolution and 1-hour timestep to provide heterogonous meteorological inputs at the surface of the model domain.

Meteorological and oceanographic inputs for the period from June 2018 to April 2019 were sourced and used for the modelling assessments. Wind roses for wind speed and direction at Crib Point, in the northwest of the bay and south of the bay (Rhyll) extracted from the mapped wind data are illustrated in Figure 2.3 to Figure 2.5, respectively.

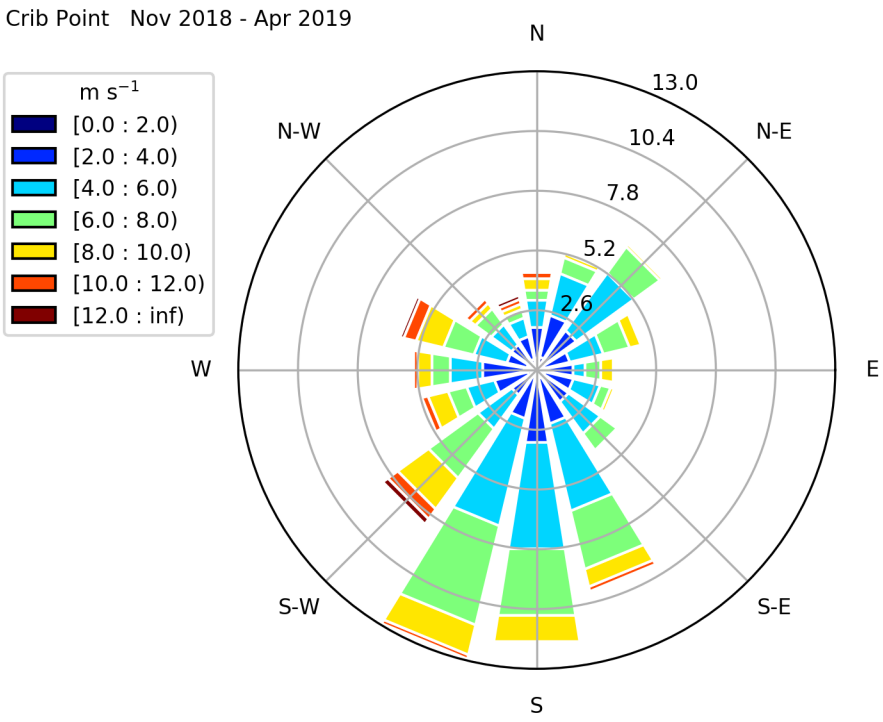

Figure 2.3 Wind rose at Crib Point from ACCESS wind maps, November 2018 to April 2019.

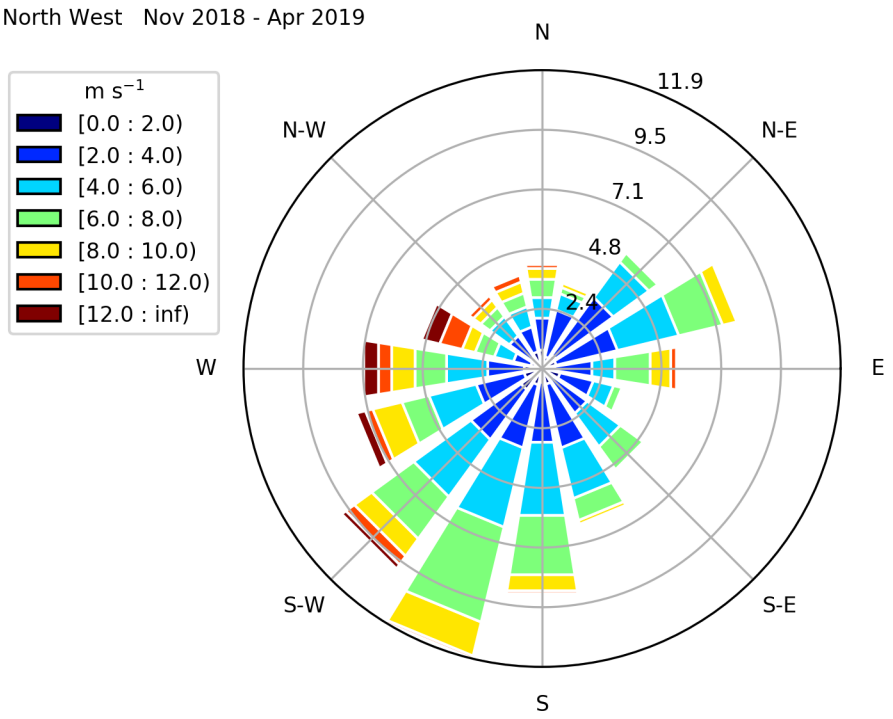

Figure 2.4 Wind rose in the northwest of WPB from ACCESS wind maps, November 2018 to April 2019.

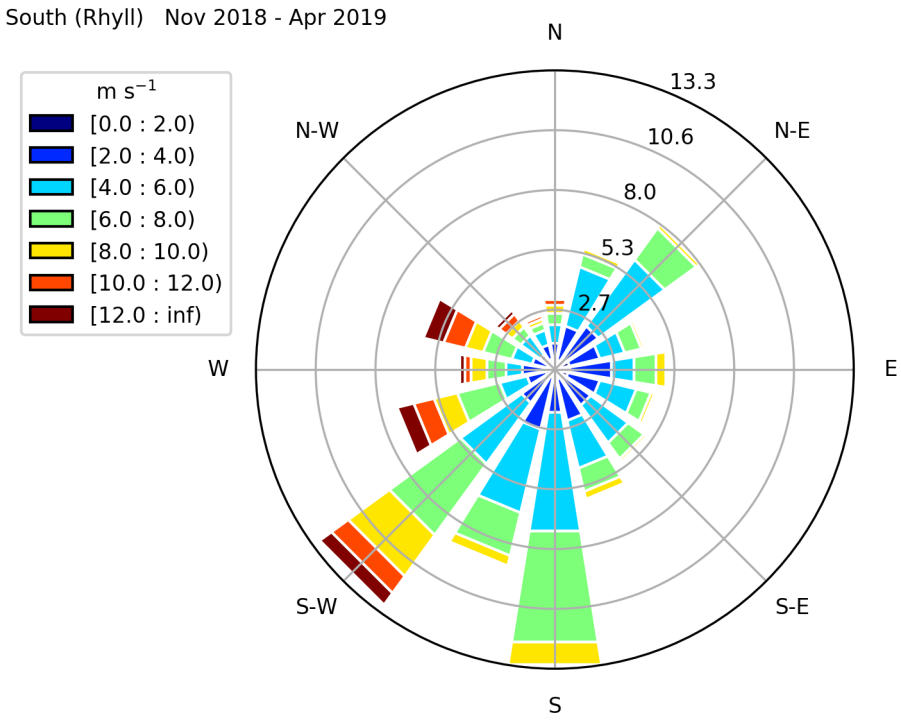

Figure 2.5 Wind rose at Rhyll from ACCESS wind maps, November 2018 to April 2019.

2.2.3 Oceanographic Inputs

The Ocean Modelling, Analysis, and Prediction System (OceanMAPS) produces a 7-day forecasts of the ocean circulation around Australia (90-180E and south of 20N) and is

underpinned by the Ocean Forecasting Australia Model (OFAM), and the Bluelink Ocean Data Assimilation System (BODAS). The OceanMAPS data were sourced from BoM at 3-hourly intervals for sea level, surface salinity and daily temperature profiles at 10 km spatial resolution. This data was used to define the ocean boundaries for WPB model.

The Bureau's OceanMAPS model provides 3-hourly sea level without tidal component. The Oregon State University's Tidal Data Inversion Software (OTIS) was then used to generate an hourly time series of the tidal component of surface height based on the latitude and longitude of each boundary cell.

The daily vertical temperature profile output at the OceanMAPS model cell near to the WPB entrance was used for the model boundary condition for temperature and 3-hourly surface salinity used to define the salinity at the boundary.

An example of the ocean boundary sea level is provided in Figure 2.6.

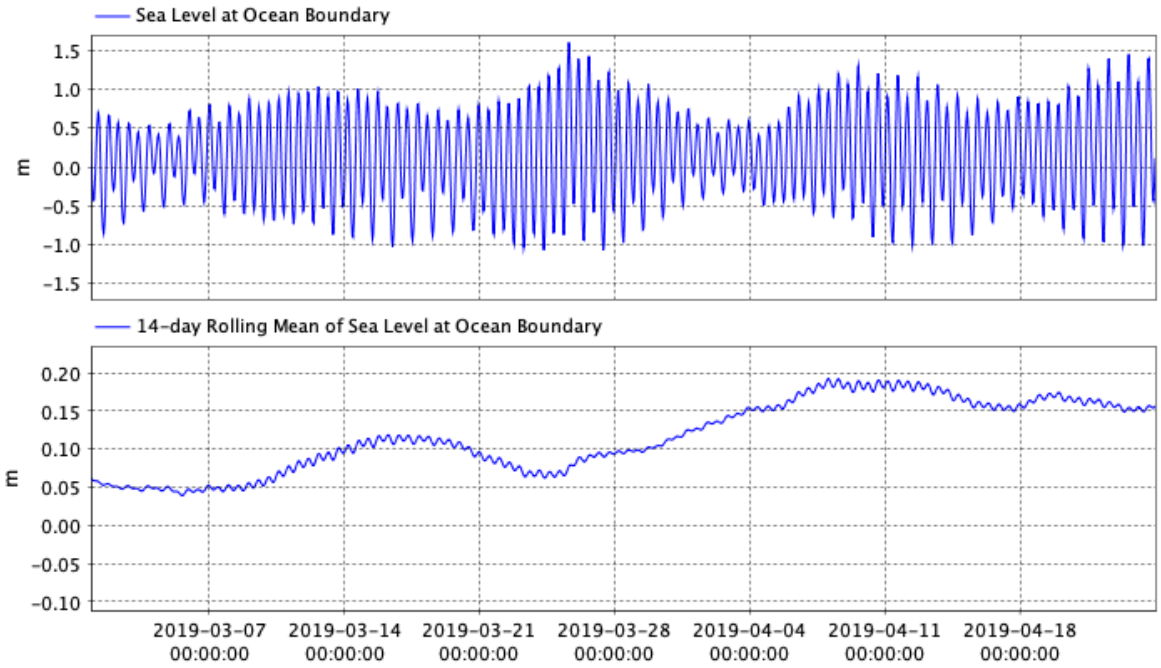

Figure 2.6 Sea-level at the ocean boundary during March-April 2019. The bottom panel illustrates the low frequency sea level changes by way of a 14-day moving average of the data above.

2.2.4 Simulations Periods

The model was applied over a calibration period from 20 March to 19 April 2019 (see Section 2.3 below) and three selected 28-day simulation periods. These simulation periods were:

- 3 to 30 June 2018;
- 11 November to 9 December 2018; and
- 3 to 30 April 2019.

Figure 2.7 to Figure 2.9 illustrate the differences in wind and sea level between the simulation periods and the calibration period. Each period experienced different prevailing wind conditions and consisted of a range of spring and neap tide phases. In addition, each period contained different low frequency sea surface oscillations.

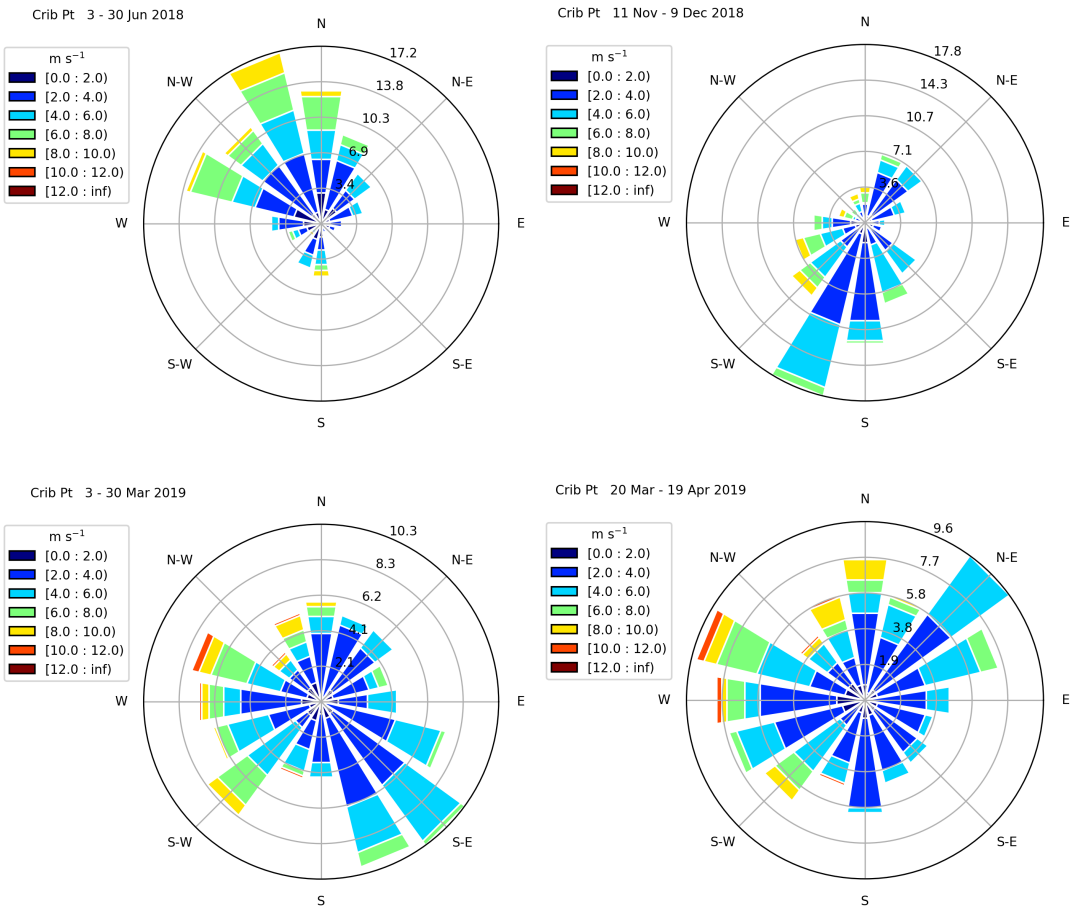

Figure 2.7 Wind roses for selected simulation periods.

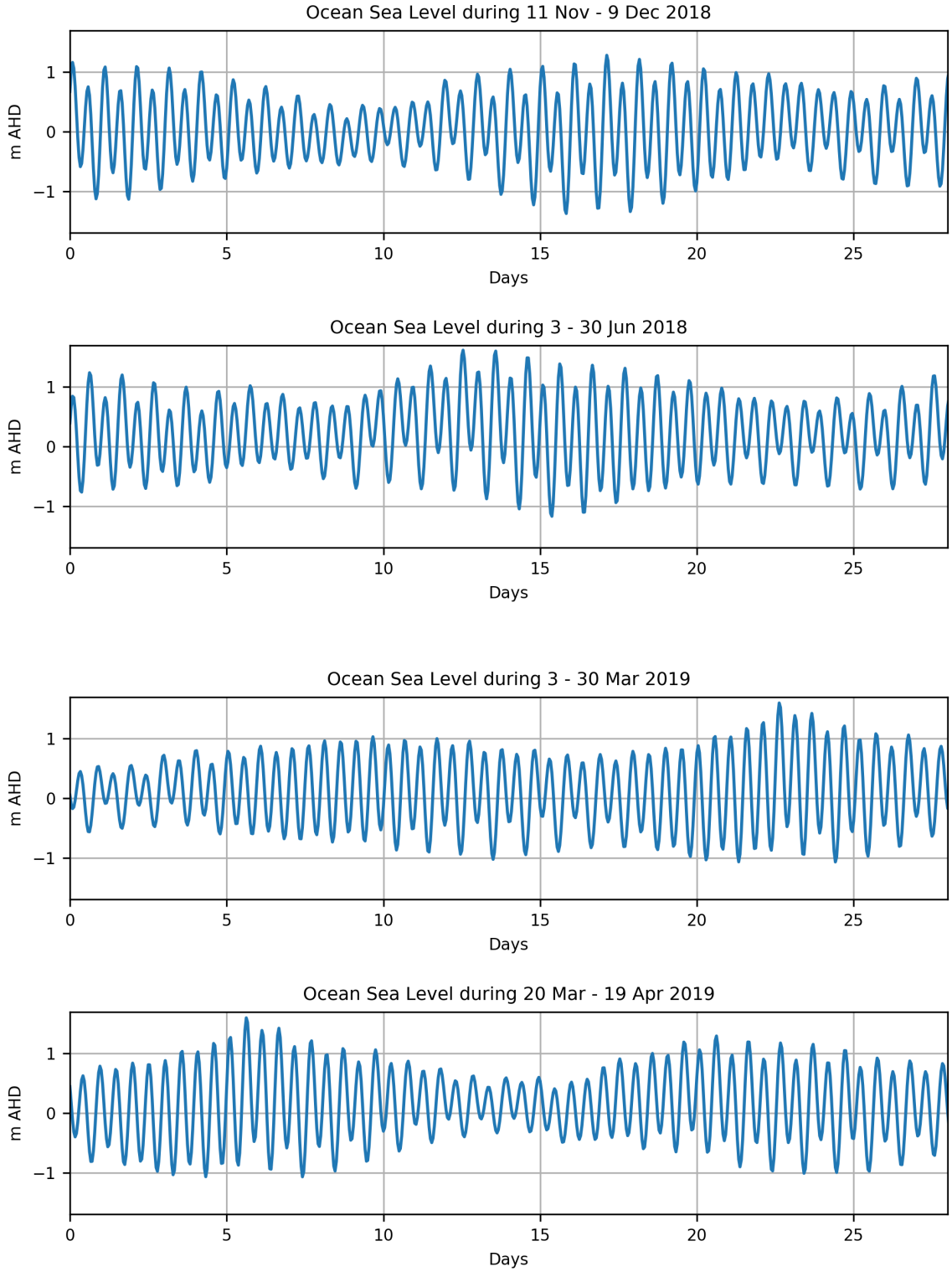

Figure 2.8 Sea level at the model boundary for selected simulation periods.

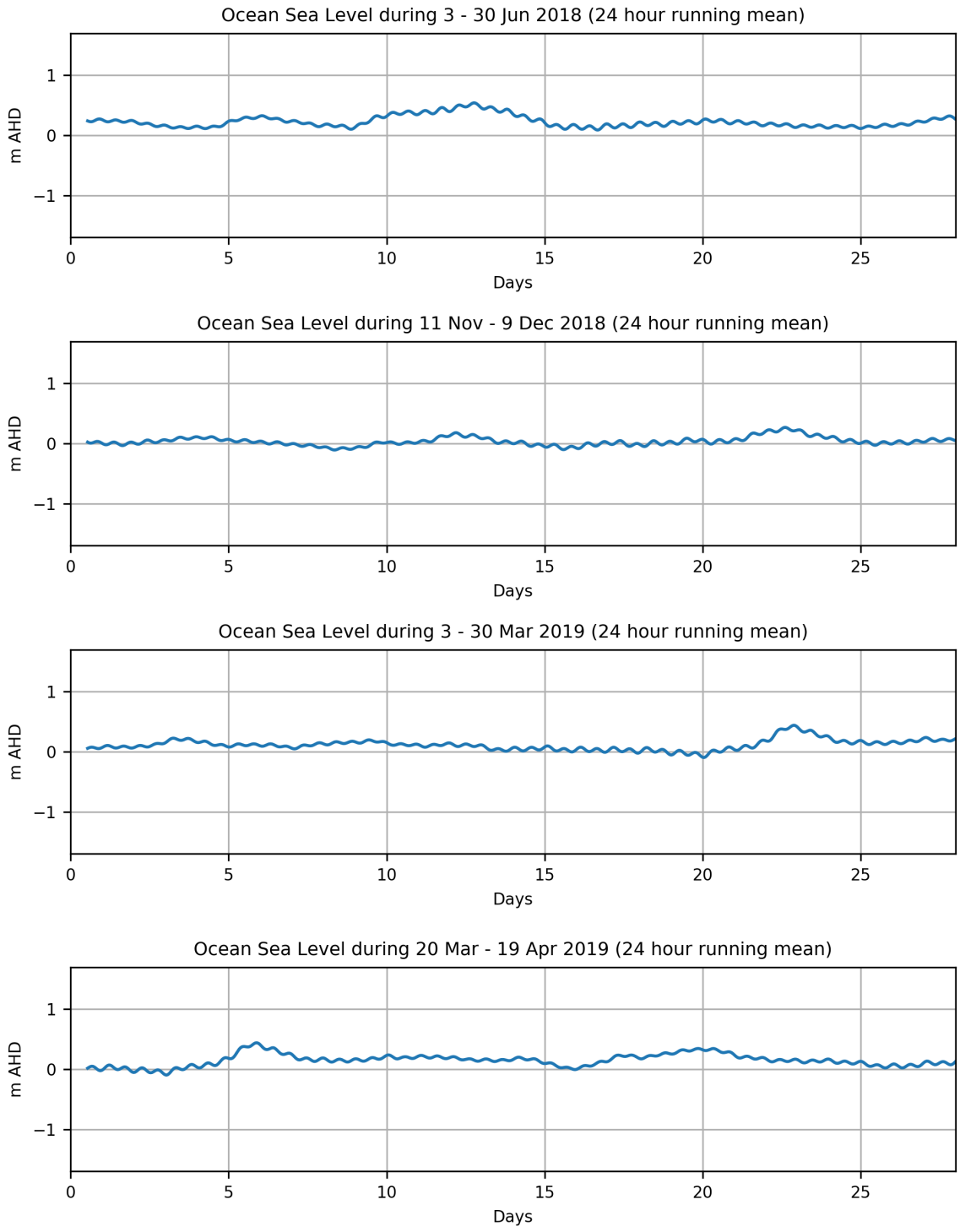

Figure 2.9 24-hour running mean of sea level at the model boundary for selected simulation periods.

2.3 Model Performance

2.3.1 ADCP Data

To assess the performance of the WPB hydrodynamic model data was collected from mid-March to mid-April 2019 using three Acoustic Doppler Current Profilers (ADCPs, Nortek AWAC 1 MHz, see Figure 2.10, refer to memo RHDHV, 2019 for details). The deployment sites were:

- ADCP 1 (West) at Crib Point Jetty Berth 2 (-38.353167^0 N, 145.226533^{o}E);
- ADCP 2 (Middle) in the main channel of northern arm (-38.348367^0 N, 145.241350^{o}E); and
- ADCP 3 (East) in the eastern channel of northern arm (-38.358183^0 N, 145.259750^{o}E).

Each ADCP was deployed at the seabed and recorded current, water level, and temperature every 10 minutes in 1 m vertical bins.

The middle meter was reported as fouled by a small boat at 1.30 pm on 24 March 2019 and subsequently towed to the north. However, the meter was found (the base frame was embedded in a sand ledge 77 m to the south of the deployment site) and it successfully recorded through the month.

The model results were compared against the observations of sea level and northward and eastward vector components near the bottom (2 m above the bed), mid-depth (5 m above the bed) and near the surface (8-9 m above the bed) for each of the deployed ADCPs. Note that only results of the final position of ADCP 2 (middle) where used in the analysis below.

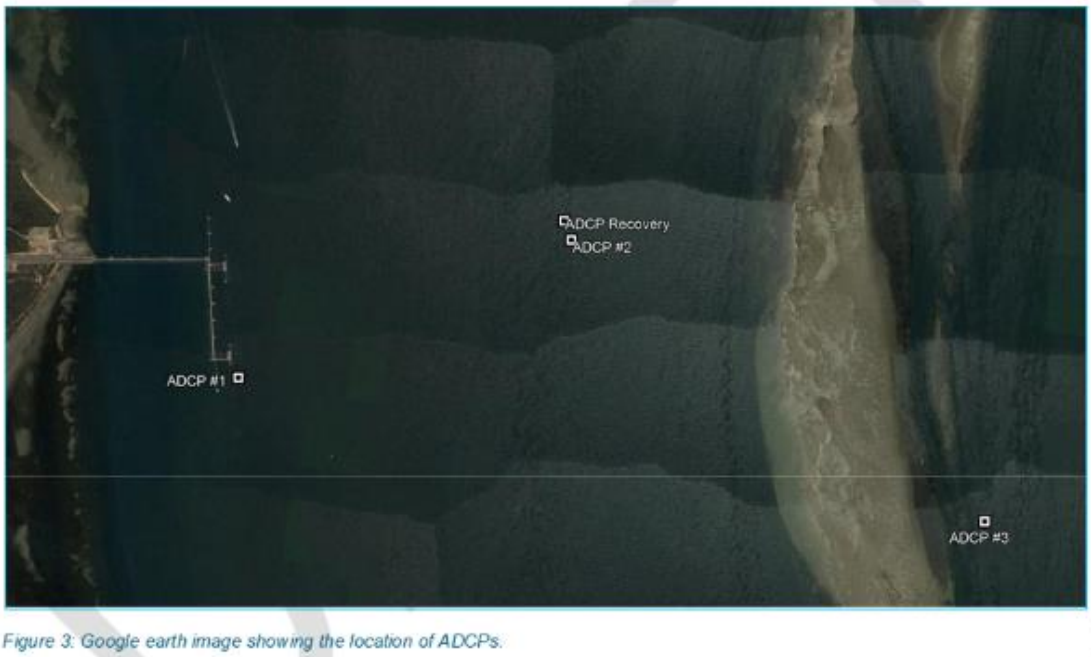

Figure 3: Google earth image showing the location of ADCPs.

Figure 2.10 ADCP locations (RHDHV, 2019)

2.3.2 Model Calibration

The model performance was assessed using the ADCP data collected in March and April of 2019. Iterations of the model configuration were undertaken to determine the most appropriate parameter values to account for bottom drag and vertical mixing rate. Previous iterations for the model were calibrated to current, turbidity and water quality data collected in different regions of the bay (Hydronumerics, 2016).

The model was calibrated by adjusting the bottom drag, mixing energy dissipation rate and mixing rate, which is described further below. The 50 x 50 m grid was used because it allowed for faster simulation times, and a number of duplicate tests using the 20 x 20 m grids demonstrated comparable results for the same parameter settings. A description of the model parameterisations and results from several iterations of the calibration process are provided in Appendix A. These model iterations were also used for model sensitivity testing (see Chapter 6).

The first parameter that was adjusted was the bottom drag coefficient, C_D. Homogenous drag coefficients in the range 10^{-3} to 5 x 10^{-3} were tested in addition to a heterogeneous drag map. The drag map was applied in previous projects (Harrison et al. 2011 and Hydronumerics, 2016) to account for different bed characteristics in WPB, the most pronounced being the differences between unvegetated sandy bed and vegetated bed. Drag values in the map ranged from low to moderate (C_D = 10^{-3} to 5 x 10^{-3}) in the sandy channels and high for seagrass meadows (C_D = 0.15) and fringing mangrove stands (C_D = 0.25). The accuracy of the drag map is not well established and is a potential source of discrepancy between the modelled and observed hydrodynamics.

The second parameter was the coefficient of dissipation, C_ϵ, that is applied in the model to determine dissipation rate $\varepsilon = 0.5 C_\epsilon \Delta t (TKE/\Delta z)^{3/2}$, where Δt is the model time step (s), Δz is the grid height (m) and TKE is Total Kinetic Energy (m^3s^{-2}), which is the mixing energy available for vertical mixing in a model cell (generated primarily by internal shear and boundary turbulence and normalised by ρA_C, where ρ is density and A_C is model cell area). High dissipation rate coefficients result in rapid dissipation of vertical mixing energy that reduces the vertical mixing of lateral momentum and thus reduces the overall momentum loss at the bottom via friction. As C_ϵ approaches 1 the modelled current velocities were faster (particularly near the surface) than the observed currents because of a lack of momentum loss at the bottom. Low values of C_ϵ (<0.1) lead to sustained mixing energy that improved the correlation between modelled and observed currents.

The third parameter that was adjusted was the mixing time rate coefficient, C_{TT}. By applying a small value of C_{TT}, vertical mixing is rapid and completed within each model time step, and so only a small amount of remaining energy is dissipated after the mixing takes place. For larger coefficients C_{TT} ~ 50, mixing within a model time step is only partial and so the TKE not exhausted in the mixing process is lost to dissipation, with the rate of loss depending on C_ϵ. Smaller values of C_{TT}< 10 achieve a similar effect to lowering C_ϵ, however for the former case mixing is more localised (to where is it generated) as only a small amount of TKE available for mixing is transported with the flow.

Because of the strong tidally driven flow in WPB, the processes of bed and internal shear are dominant mechanisms generating mixing energy in the water column and are a function of the bottom drag. Different combinations of bottom drag, dissipation rate, and mixing rate where

able to produce similar predictions of currents; with the exception of cases with weak vertical mixing (i.e. high values of both $C_{\epsilon,}$ and C_{TT}). The calibrated model results that are compared to observations in the sections that follow, arise from model configuration with the heterogeneous bottom drag coefficient map (as described above), low dissipation rate coefficient of C_{ϵ}= 0.018 and high mixing time rate coefficient C_{TT} = 50.

The implications of the key discrepancies that arise between the observed and simulated model results in relation to how they may influence the predictions of the impact of the FSRU are addressed Chapter 6.

2.3.3 Modelled Surface Heights

Figure 2.11 to Figure 2.13 illustrate the comparisons between observed and simulated surface water levels at each of the three ADCP locations. There was good agreement between the observed and modelled sea level for both the tidal heights and phase. The R^2 values were increased to from 98% to 99% or higher when a phase shift of -6 minutes was applied to the modelled results. Discrepancies in the phase may arise from both the hydrodynamic model solution and/or from the accuracy of the sea level that is applied at the open ocean boundary as these values have been synthesised from OceanMAPS low-frequency sea level oscillation model combined with the tidal oscillation model predictions from OTIS.

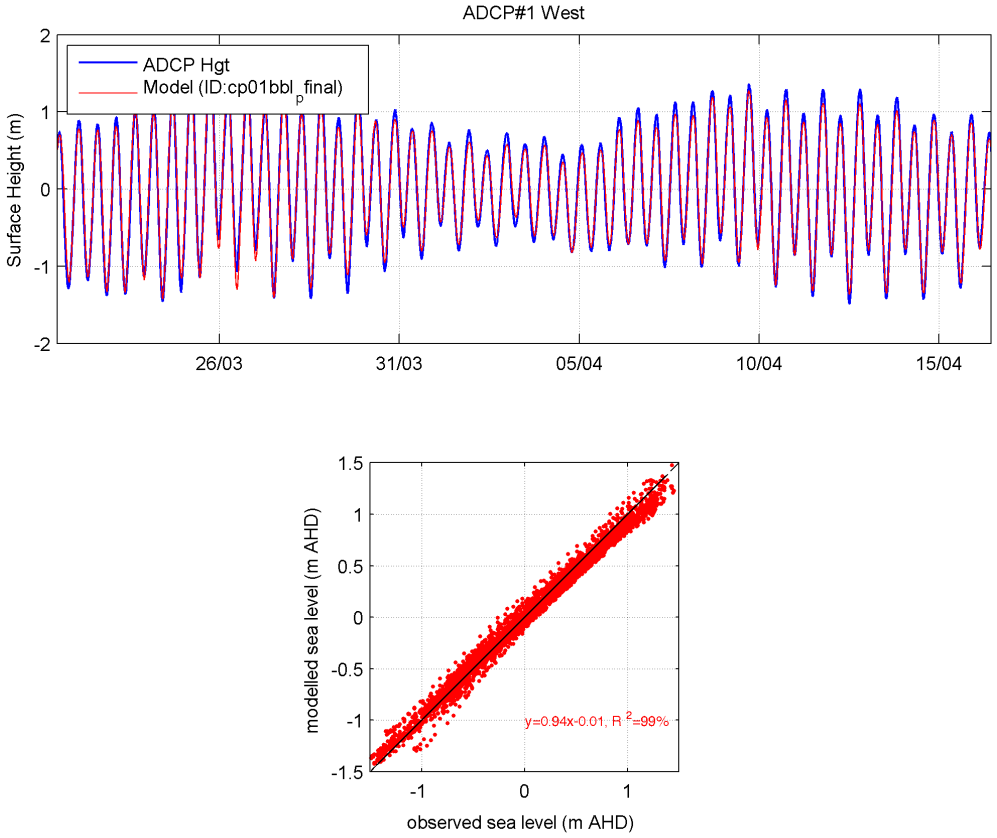

Figure 2.11 Comparison between observed (blue) and modelled (red) surface heights at West ADCP 1 (West).

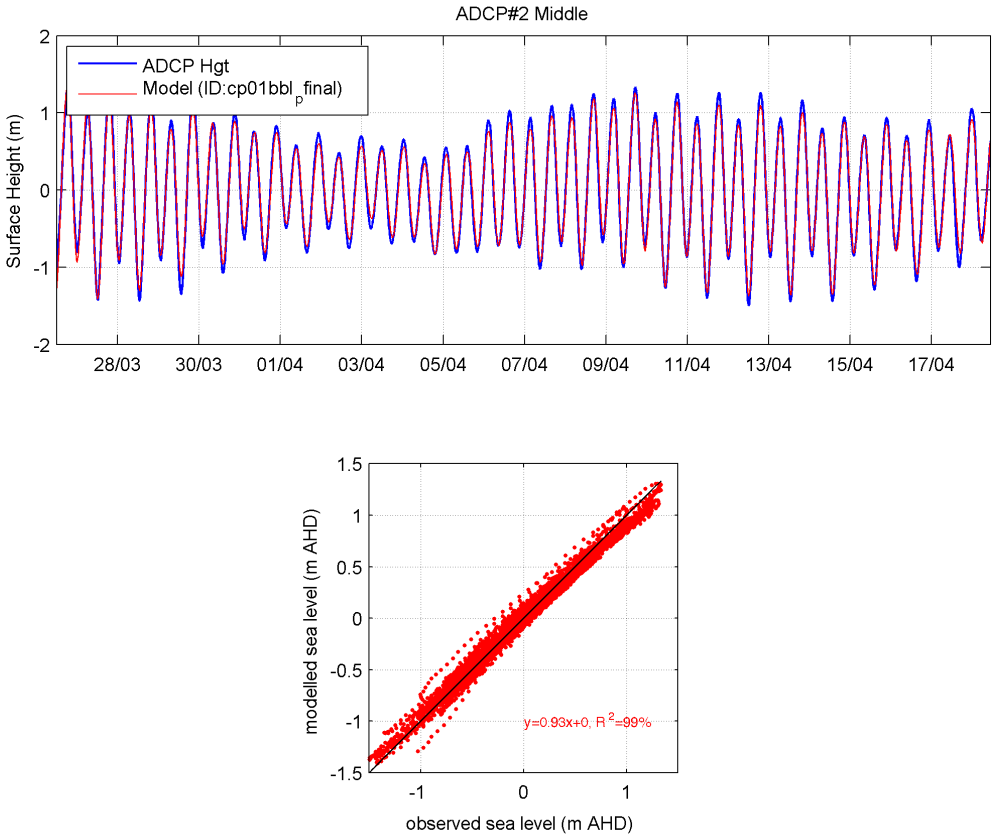

Figure 2.12 Comparison between observed (blue) and modelled (red) surface heights at middle ADCP 2 (Middle).

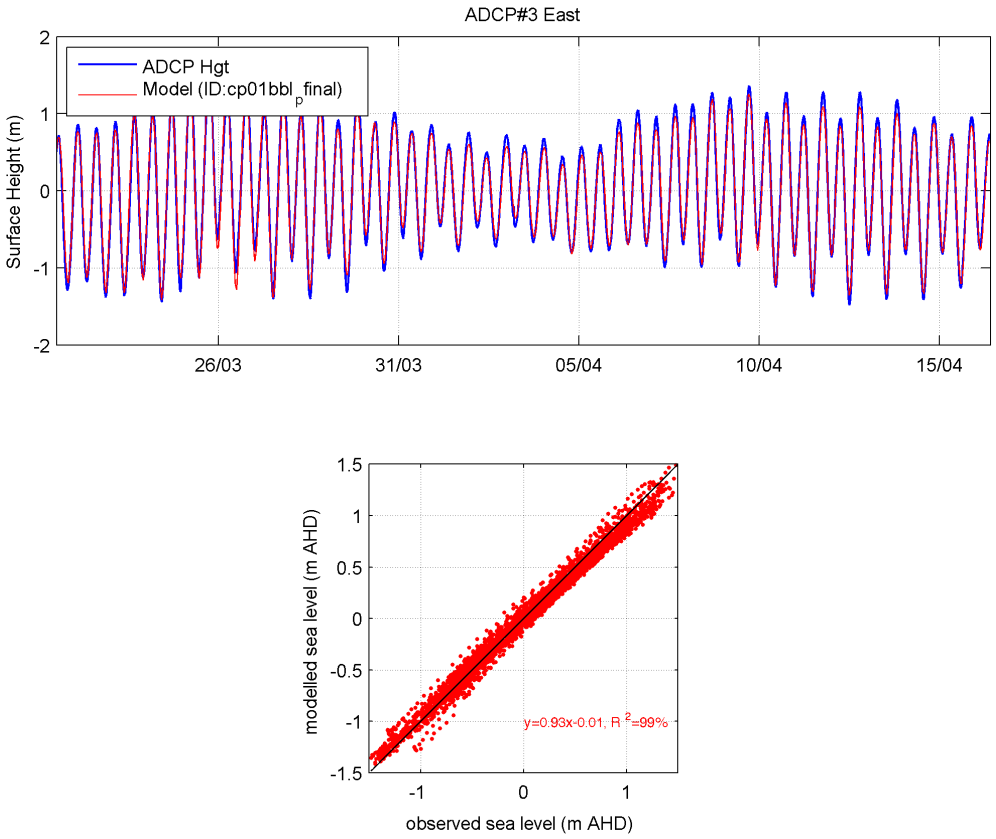

Figure 2.13 Comparison between observed (blue) and modelled (red) surface heights at East ADCP 2 (East).

2.3.4 Modelled Currents

Time series of the simulated and modelled currents are illustrated in Figure 2.14 to Figure 2.16 for each ADCP at three levels above the seabed. Current roses of the same are illustrated in Figure 2.17 to Figure 2.19. Ebb and flood vectors are shown in Figure 2.20 and Figure 2.21.

The results show the dominance of observed and modelled north-south components of the current during the flood and ebb phases of the tide, with only small contributions from the east-west components of the current.

Overall, the model reproduced the observed north-south vector components with a good level of skill, and reliably reproduced the timing of changes in the observed current. The largest discrepancy occurred at the middle ADCP during spring tide, when the model briefly produces 10-20% higher peak near-surface southerly currents during ebb flow. The middle ADCP was installed at a location with complex and relatively dramatic bathymetric features that produce large cross-sectional gradients in the flow (see Figure 2.22). Analysis of model outputs 2 grid cells to the east (i.e. 100m) indicated a reduction of peak ebb southward surface currents of 8% that better correlated with the observed data. It is likely that this discrepancy relates in part to the gridded representation of the bathymetry and is thus more pronounced during spring ebbing tide when water level is lowest and the southerly flow finds passage through bathymetric constrictions, which will accelerate modelled flow near the surface and slower flow near the bottom.

A second notable discrepancy in the modelled north-south currents is weaker bottom currents at the western ADCP as seen in Figure 2.14. This is again likely to be most dependent on the complex local bathymetry, with better matches to the data obtained for model locations 100 m east of the designated ADCP location. To add to this, there is an apparent discrepancy between the recorded maximum depth during the western ADCP deployment of 15 m, and model grid bathymetry maximum depth of 17 m. This will impact on the simulated near-bottom currents and indicates potential changes to the bed-shape in this region since the collection of bathymetric survey data used to construct the model grid.

Observed and simulated east-west current vectors shown good agreement and are significantly weaker than the north-south components with a majority of simulated flow following the north-south grid alignment. RHDHV (2019) notes that the compass accuracy is 2° for a tilt of less than 15°. The authors also note that the middle ADCP was displaced during deployment and embedded in a sand ledge at a steep angle of approximately 45°, which may have influenced the directional readings.

Figure 2.20 and Figure 2.21 show a comparison of the simulated (red arrows) and measured (blue arrows) median and 75th percentile currents at Crib Point and all three ADCP sites, respectively. The results indicate a good overall agreement at all three sites in terms of flow speed and direction. As described above the figures illustrate overpredicted ebb tide at the middle ADCP near the surface, and underpredicted bottom currents at the western ADCP.

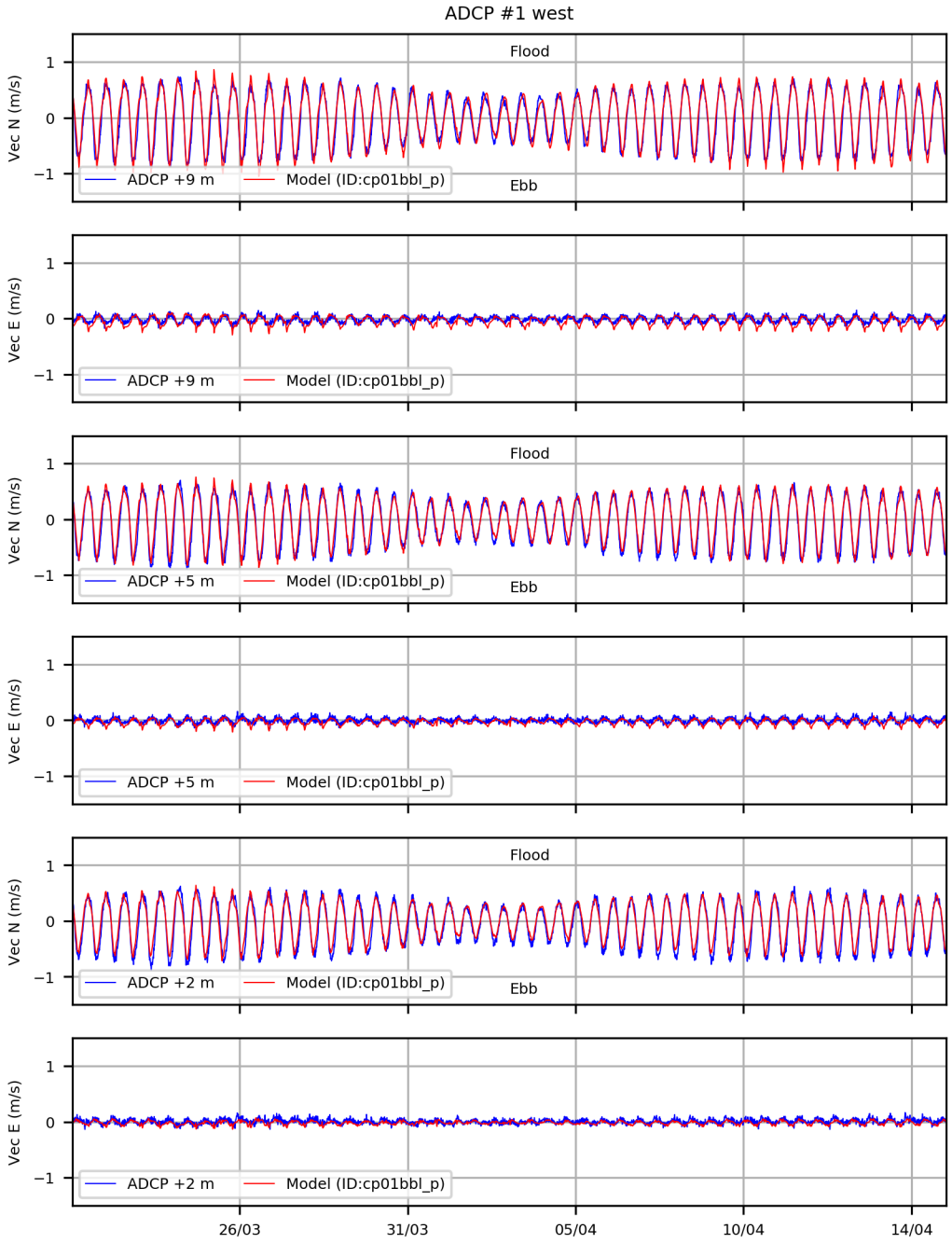

Figure 2.14 Comparison between observed (blue) and modelled (red) north and east current vectors at ADCP 1 (West).

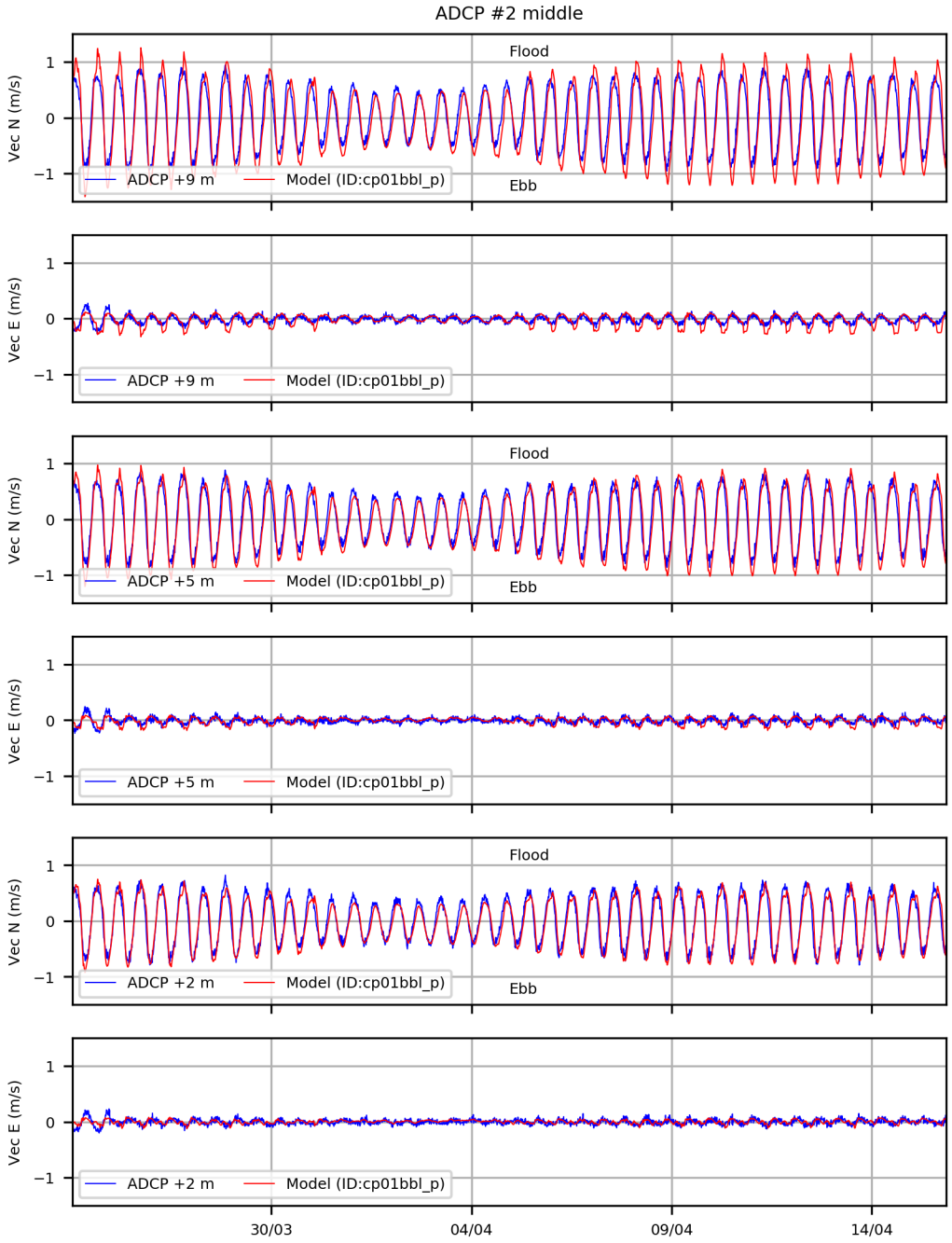

Figure 2.15 Comparison between observed (blue) and modelled (red) north and east current vectors at ADCP 2 (Middle).

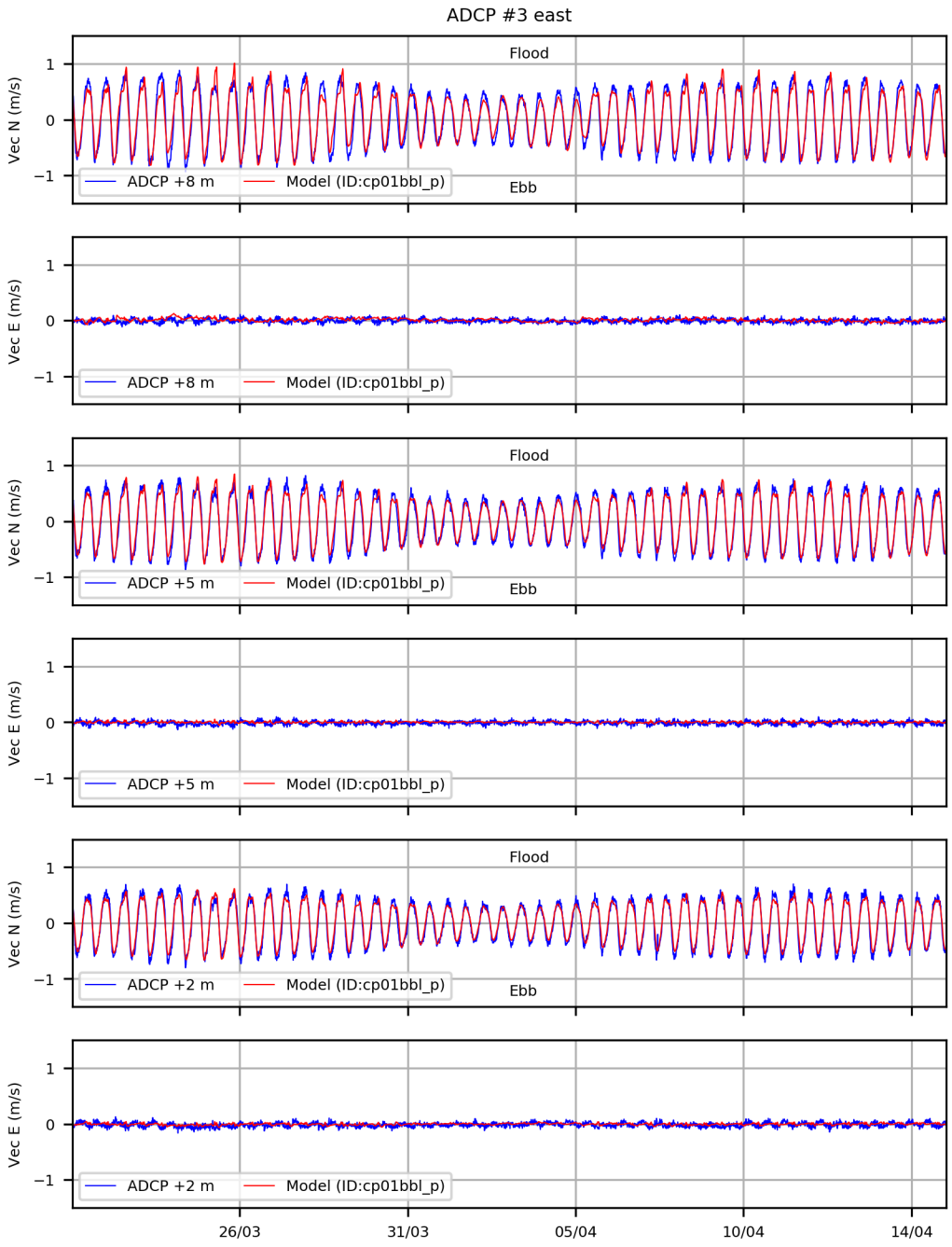

Figure 2.16 Comparison between observed (blue) and modelled (red) north and east current vectors at ADCP 3 (East).

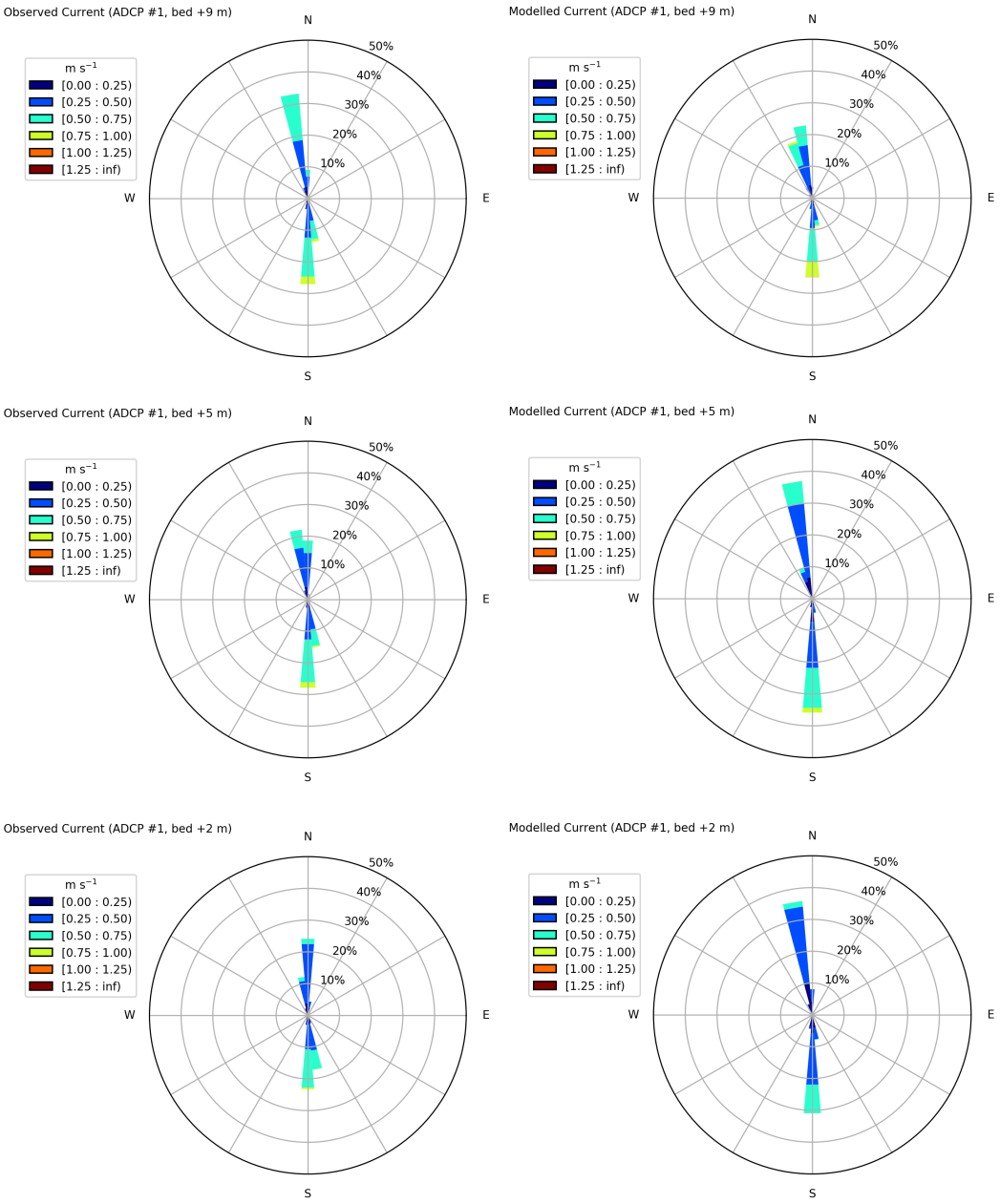

Figure 2.17 Observed (left) and modelled (right) current roses at ADCP 1 (West) at (from top to bottom of page) 9, 5 and 2 m above the seabed.

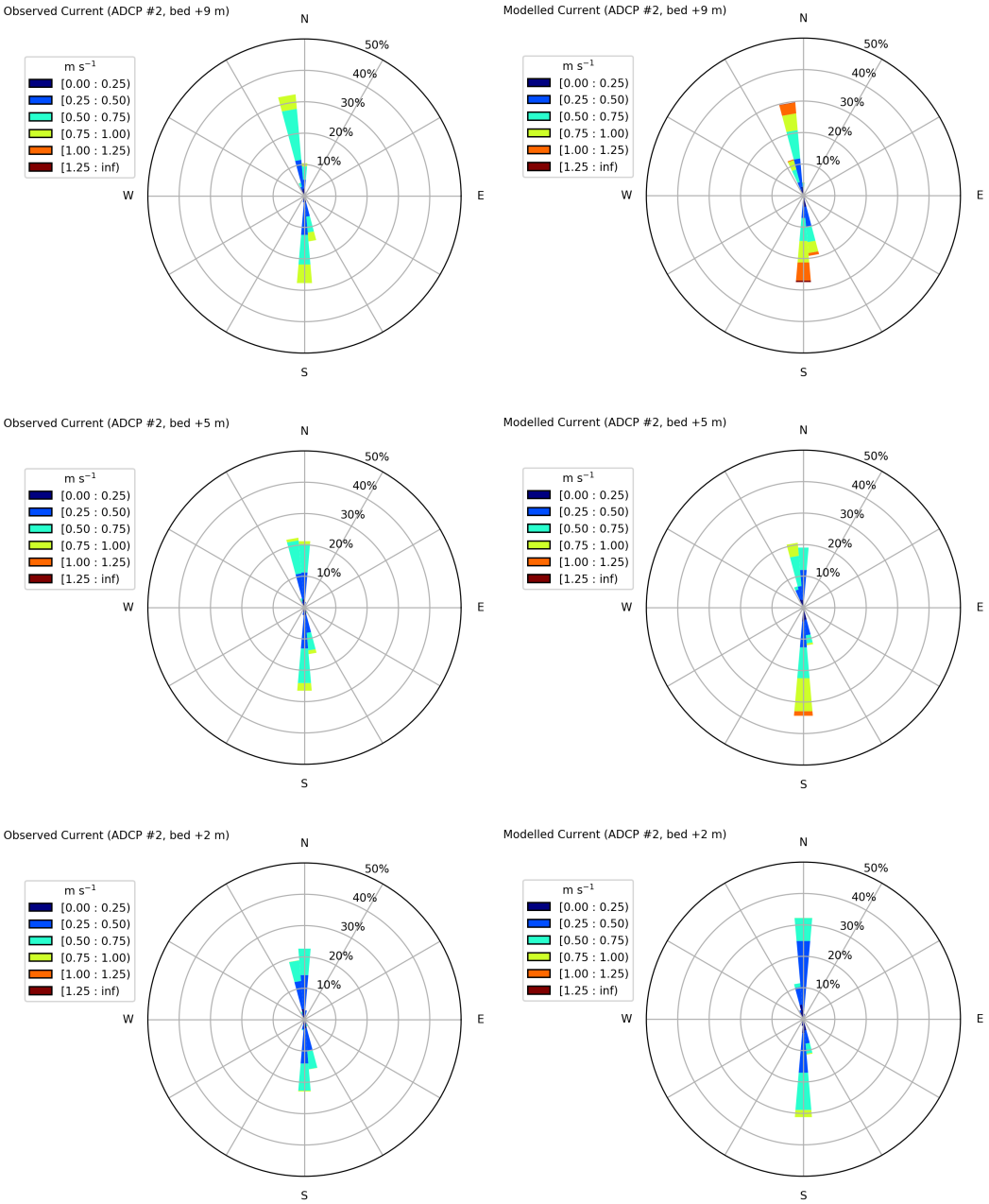

Figure 2.18 Observed (left) and modelled (right) current roses at ADCP 2 (Middle) at (from top to bottom of page) 9, 5 and 2 m above the seabed.

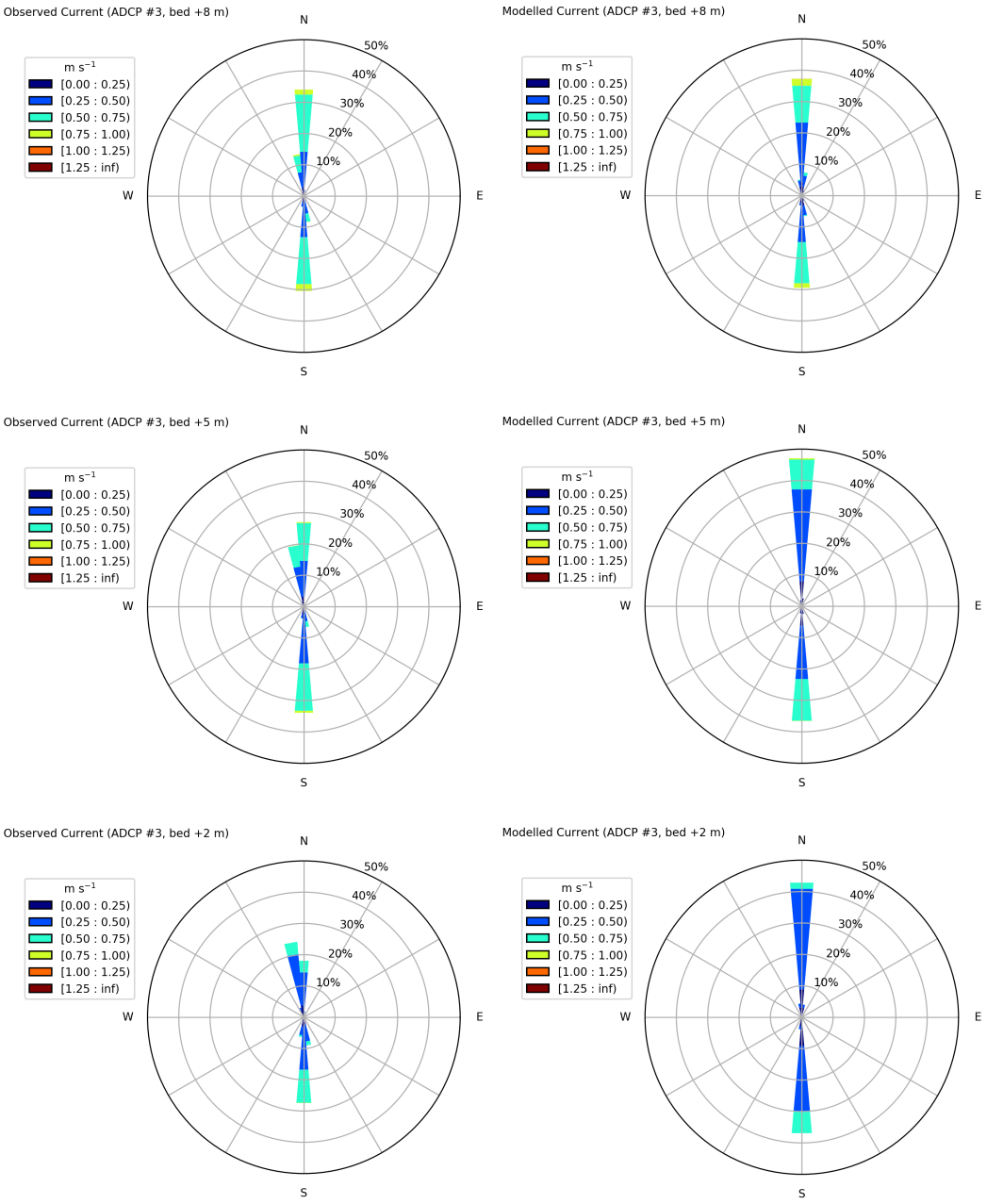

Figure 2.19 Observed (left) and modelled (right) current roses at ADCP 3 (East) at (from top to bottom of page) 9, 5 and 2 m above the seabed.

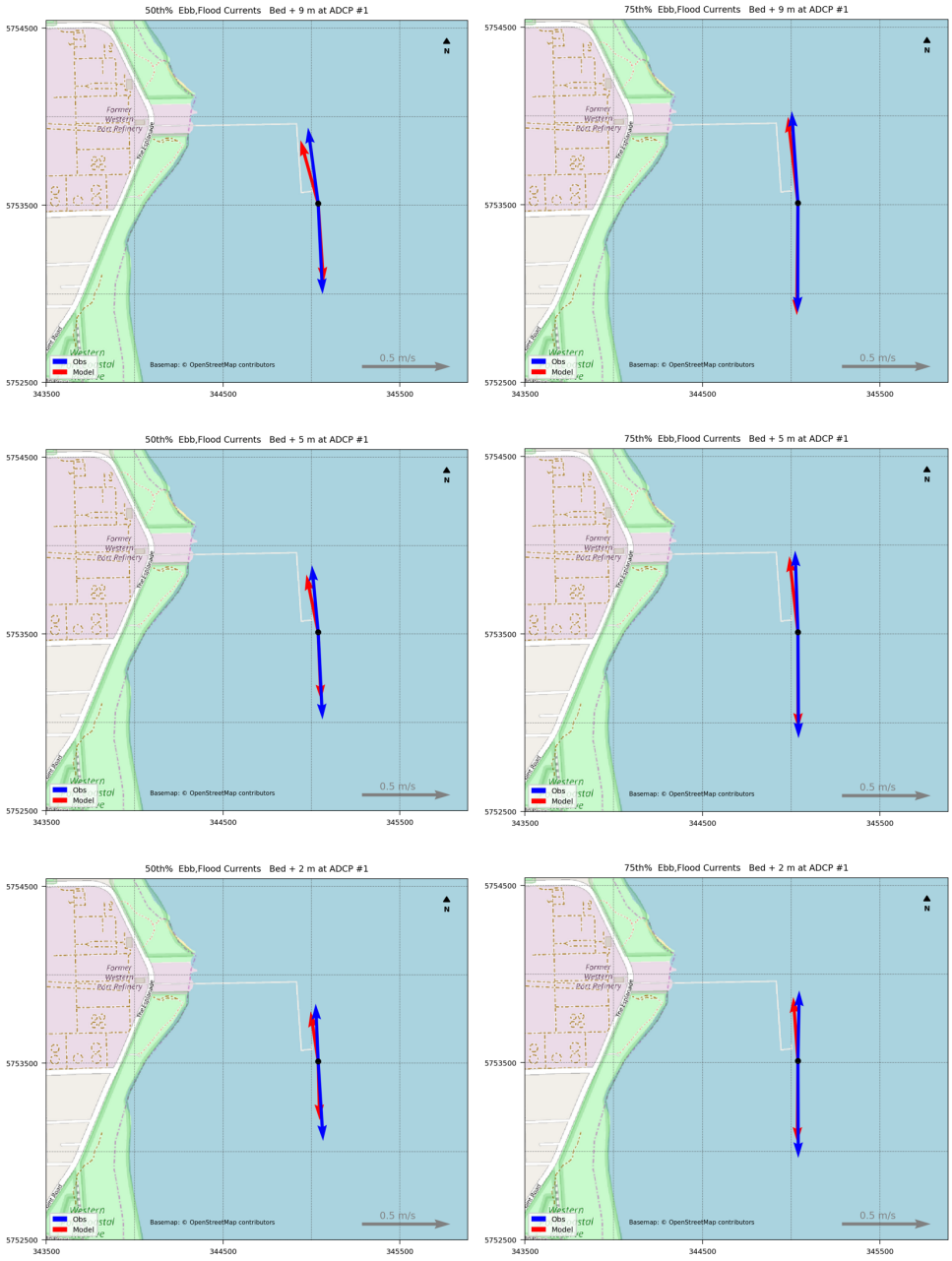

Figure 2.20 Comparison between observed (blue) and modelled (red) 50th (left column) and 75th (right column) percentile ebb and flood velocity vectors at ADCP 1 (West) at (from top to bottom of page) 9, 5 and 2 m above the seabed.

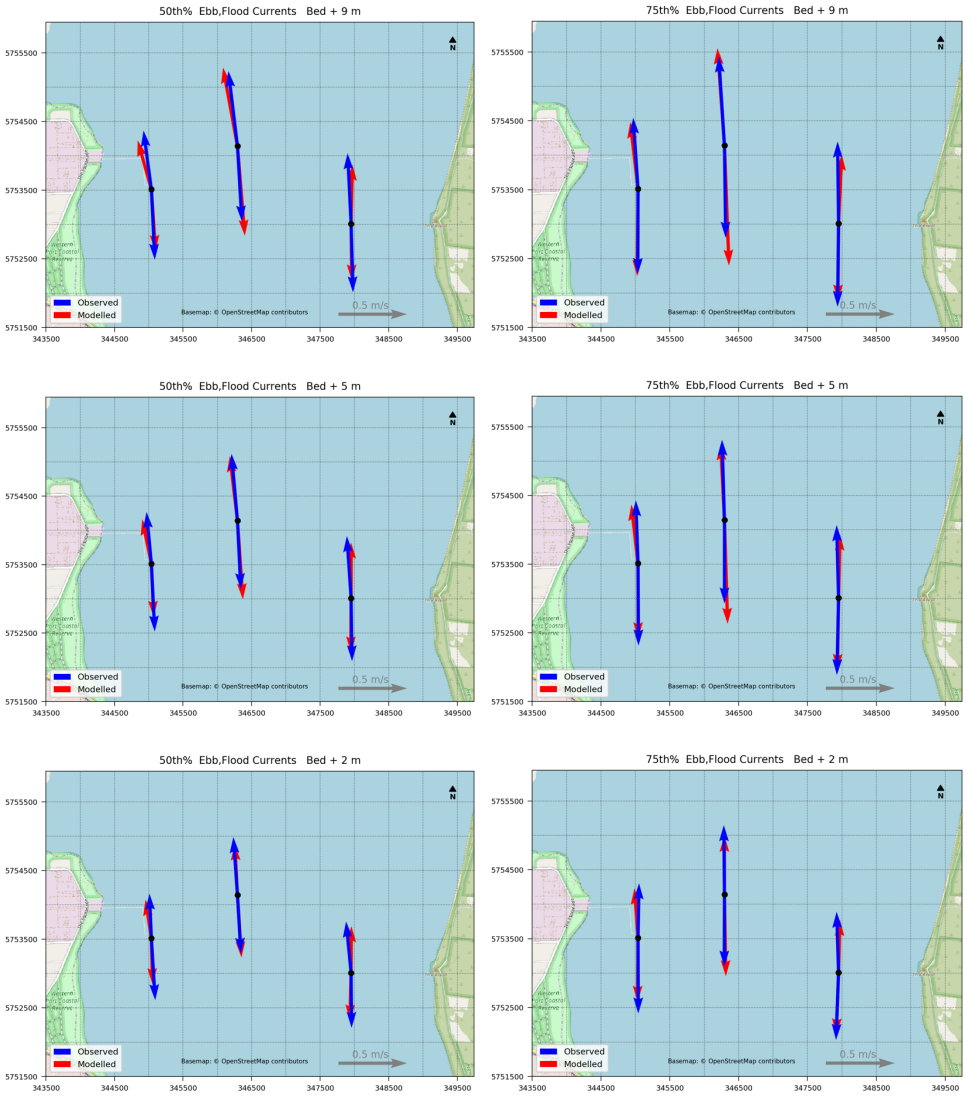

Figure 2.21 Comparison between observed (blue) and modelled (red) 50th (left column) and 75th (right column) percentile ebb and flood velocity vectors at all ADCP locations at (from top to bottom of page) 9, 5 and 2 m above the seabed.

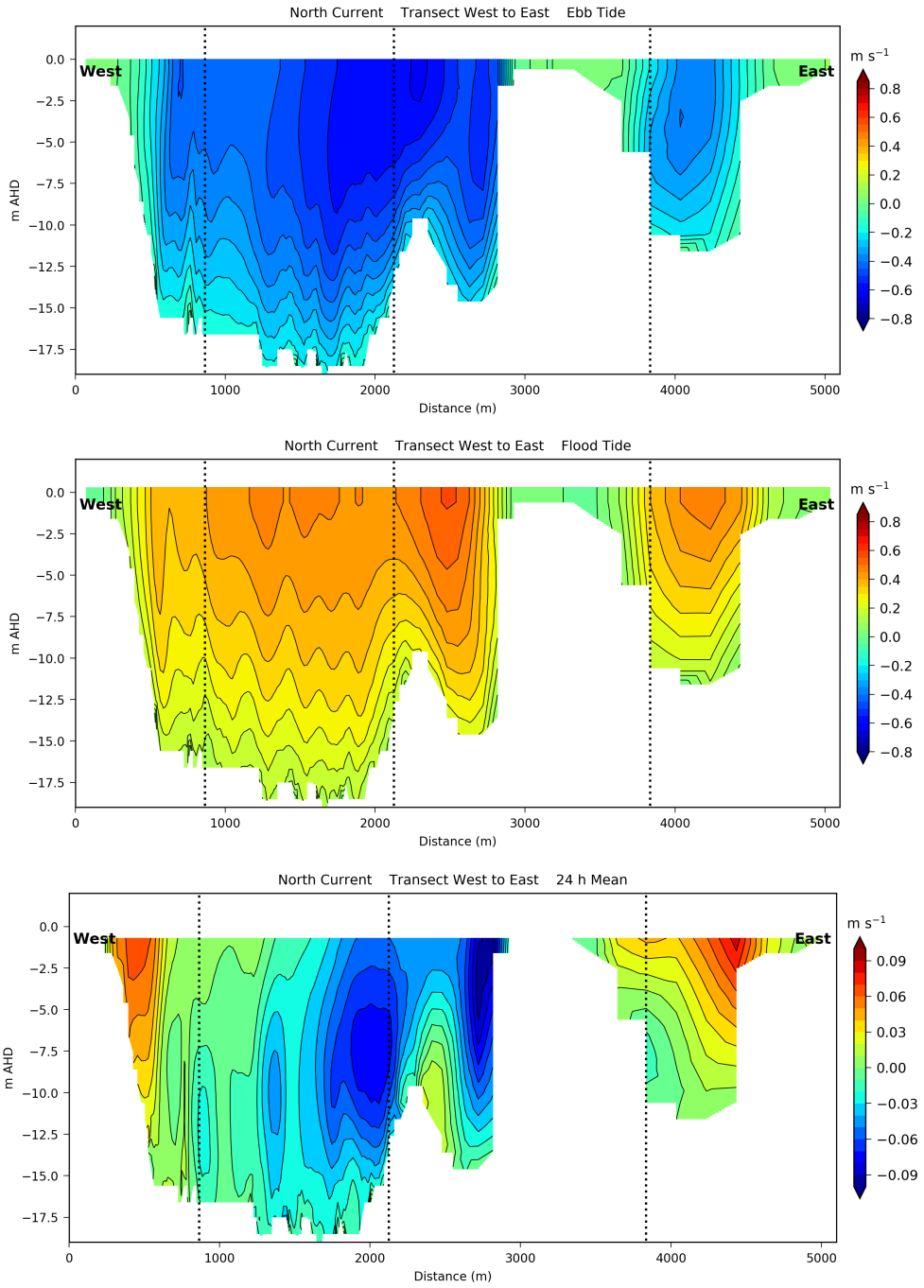

Figure 2.22 A cross-section west to east of the simulated northward current during ebb (top panel) and flood (centre panel) tide, and the 24 h mean northward current (bottom panel, note smaller range of contour values). Approximate locations of ADCPs are indicated by dotted vertical lines.

2.3.5 Correlation with Observed Currents

The correlations between the observed and modelled vector time series are presented in Figure 2.23. The functions relating the variables have been produced by linear least squares fitting. For north-south flow direction R^2 values range from 92% to 98%, which indicates a very good fit between observed and modelled data. For the fitted linear functions all intercepts were

less than 0.06 ms^{-1}. Gradients ranged from the lowest of 0.82 at the bottom for ADCP 1 (West) to 1.12 at the surface for ADCP 2 (middle); the reasons for these discrepancies are discussed above in the vector time series comparison. The remaining gradients were between 0.86 and 1.04, indicating a good fit between the model and observations.

The model produced significantly weaker easterly currents, which were also observed, with gradients between 0.32 and 1.09 and R^2 values from 47% to 73% for ADCP 1 (west) and 2 (middle). The observed and simulated easterly current vectors at ADCP 3 (east) were both very weak and no meaningful correlations were derived.

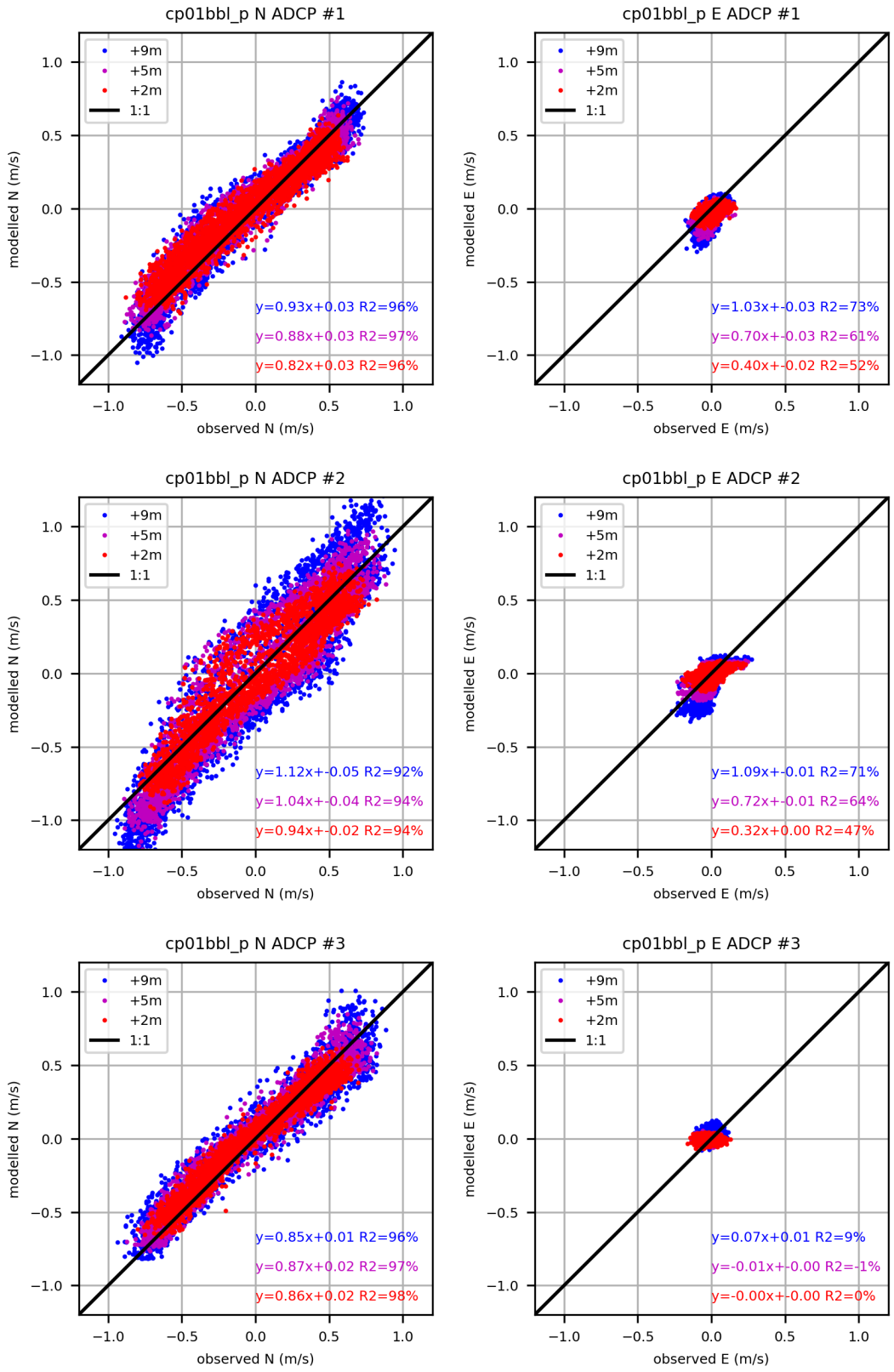

Figure 2.23 Least squares linear fits observed and modelled north and east current vectors at all three ADCP locations.

3 FSRU Cool Water Discharge

3.1 Model Set-up

3.1.1 Description of Discharge

Seawater will be taken from WPB by the FSRU and passed through heat exchangers before being discharged back into the bay. Water discharged from the FSRU will be up to 7 °C cooler than ambient seawater. The discharge exits via six ports on the starboard side, each having a diameter of 0.45 m, spaced at least 10 m apart, and located about 2 m below sea level. Discharge through each port creates six separate plumes that spread laterally to the east and dilute before merging.

There are three heat exchangers (regasification units) on the FSRU, each with two ports so, depending on the level of gas production, two, four or six ports will be operating concurrently. The indicative month-by-month gas production is shown in Figure 1.4. Peak gas production, and hence peak seawater intake and discharge, will occur in the winter months when six ports discharge a total of 5.4 m^3/s. Over the year, the average intake and discharge is equivalent to four discharge ports at a total of 3.6 m^3/s.

3.1.2 Near Field Modelling of Plumes

Near field modelling of the discharge plumes was undertaken by CEE. The description that follows was provided by Ian Wallis (memo dated 14 May 2019**).**

The trajectory of the plumes was calculated by a 3-D plume model taking account of entrainment around the perimeter of the plume, conservation of mass, conservation of lateral momentum with entrainment of a northward or southward current, and conservation of vertical momentum allowing for the effect of gravity in pulling the slightly dense plume towards the seabed. The resultant plume for a range of current speeds is described in Table 3.1.

With faster currents, the plume more rapidly entrains the transverse momentum of the ambient tidal current and turns into the current, thereby limiting the lateral travel of the plume. With weaker currents, there is a larger lateral travel, and also a greater sinking of the plume towards the seabed.

The plume spreads rapidly as it entrains the ambient tidal current and reaches the seabed at the lower edge of the plume, with the majority of the plume in the water column. There is always dilution due to the high initial velocity of the plumes (with a discharge velocity of 5.4 m/s), with the dilution increasing with the tidal current speed.

At times of weak or zero current (which occurs for about 15 minutes per day when the current speed is 3 cm/s or less) the temperature at the end of the diluted plume is 0.35 ^{0}C cooler than ambient. The median current is 0.4 m/s and the extra mixing with this current means that the temperature difference of the diluted plume is only 0.14 ^{0}C cooler than ambient.

Table 3.1 Near-field Prediction of Plume Extent and Temperature Difference.

Current Speed[#] (m/s)	Lateral Extent (m)	Top of Plume (m bsl*)	Base of Plume (m bsl)	Temp Difference ^{0}C	Percentile current Exceeded
0.03	60	0	14	0.35	99 %
0.1	50	0	14	0.33	90 %
0.15	48	0	13	0.28	85 %
0.2	45	1	12	0.23	80 %
0.3	40	1	12	0.18	65 %
0.4	35	1	12	0.14	50 %
0.5	30	2	12	0.13	30 %
0.6	28	2	12	0.11	10 %
0.7	26	2	12	0.10	3 %
0.8	24	2	12	0.09	1 %
0.9	22	2	12	0.09	-
1	20	2	12	0.09	-

[#2] N/S current east of FSRU; * bsl refers to distance below sea level.

3.1.3 Far Field Modelling of Plumes

To provide sufficient plume detail the 20 x 20 m model grid was used for the far-field modelling of the cooled water discharge. The discharge configuration of 6 ports spaced 10 m apart and the near-field discharge characteristics identified by CEE (Table 3.1) were used to define initial 'footprints' of the discharge in the far-field model (Table 3.2). The FSRU discharge was represented in the far-field model by continually updating the water temperature of the model cells in the plume footprint (determined by the near-field model) at each timestep. A temperature decrease of ΔT_t was determined during each model time-step using the calculation:

$$\Delta T_t = \frac{-\Delta T_F Q_F \Delta t}{V_{TC}},$$

where

ΔT_F is the decrease from intake temperature, T_{intake} (-7 °C)

Q_F is the outflow rate from FSRU (5.4 m^3 s^{-1})

Δt is the model time step (20 s)

V_{TC} is the total volume of model cells within initial footprint.

The plume generated by 6 ports is located 40 to 120 m from the bow on the starboard (eastern) side of vessel. This configuration is illustrated diagrammatically in plan-view in Figure 3.1. The lateral travel of the discharged plume perpendicular to the vessel in response to the momentum of the discharge flow is modified using the simulated ambient current velocity and matching this with the nearest velocity from Table 3.2, as illustrated in Figure 3.2. The advection of the plume after this initial input is governed by the modelled ambient flow in the far-field model. A description of the plume boundary conditions and resultant behaviour of the plume during the tidal cycles has been provided in Section 3.2.1 below using examples of model results.

The effect that the vessel hull has on local flow around the vessel was taken into account in the far-field model (see Appendix B). The model was configured with uniform background temperature of 13.4 °C for winter months. The FSRU was the only source of heat loss (i.e. no additional boundary and atmospheric exchange) in the simulation so the results identify only the impacts to water temperature that are produced directly by the FSRU discharge.

Discharge scenario simulations were undertaken using input data from a 28-day period in March 2019, which includes neap and spring tide periods and a range of wind conditions (see Section 2.2.4). Additional sensitivity tests were undertaken using the model forcing data from June 2018 (see Section 9.2.1).

The simulations of discharge in this report assumes that the FSRU has average draught. Whilst at times the FSRU will be heavier and sit deeper in the water, or lighter and sit higher, the near-field modelling indicates that the plume will develop quickly to occupy the water column from surface to bed and so the changes in vessel draught are unlikely to have a significant influence on the modelling outcomes.

Table 3.2 Initial footprint in 20 x 20 m far-field model (north-south extent is 60 m for 4-port case)

Current Speed (m/s)	North-South Extent (m)	East-West Extent (m)	Distance FSRU to Plume Centre (m)	Top of Plume (m bsl)	Base of Plume (m bsl)
0.0 (slack tide)	80 (60)	40	60	0	14
0.1	80 (60)	40	40	0	14
0.15	80 (60)	40	40	0	13
0.2	80 (60)	40	40	1	12
0.3	80 (60)	40	40	1	12
0.4	80 (60)	40	40	1	12
0.5	80 (60)	40	20	2	12
0.6	80 (60)	40	20	2	12
0.7	80 (60)	40	10	2	12

0.8	80 (60)	40	10	2	12
0.9	80 (60)	20	10	2	12
1	80 (60)	20	10	2	12

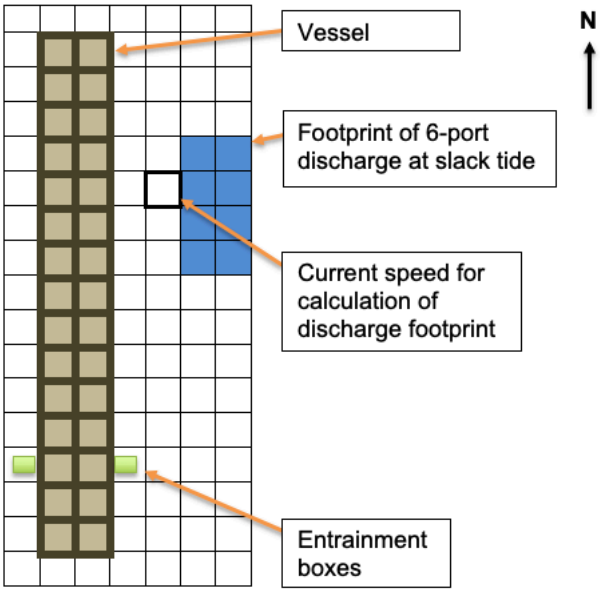

Figure 3.1 Model cell locations selected for plume input in far-field model. Each cell is 20 x 20 m in size.

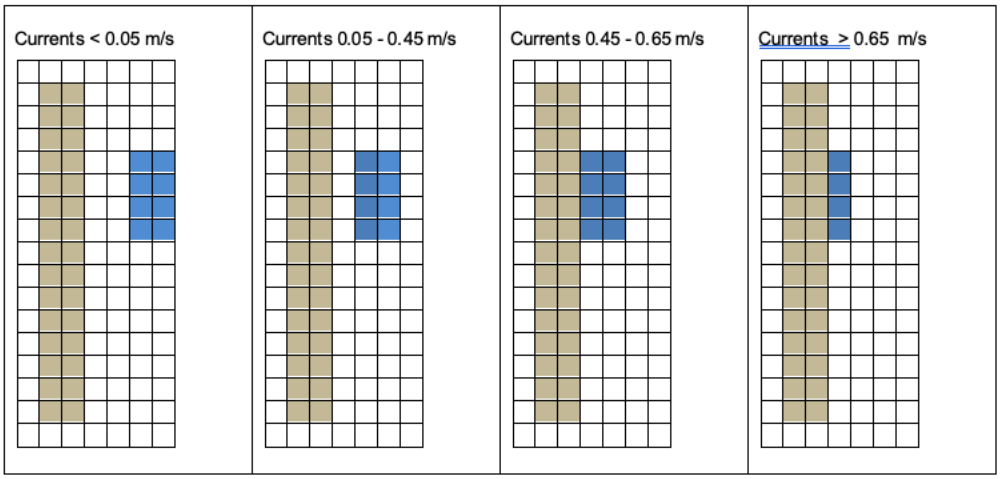

Figure 3.2 Modified lateral plume position as a function of ambient velocity.

3.2 Model Results

3.2.1 Behaviour of the Discharge Plume

The heat exchanger discharge plume input and behaviour in the far-field model is described below over for the phases of a tidal cycle.

High Tide

At high tide the ambient northward currents weaken and the momentum of the discharge from the heat exchanger ports means that the plume is input into the far-field model at a distance of 60 m to the east of the FSRU with a width of 40 m (Table 3.2). The plume is spread from the water surface to 14 m below the surface and because it is cooler than the ambient seawater, and therefore of higher density, it descends towards the seabed in the far-field model. From here it spreads radially as a dense flow with the lowest temperatures simulated at the seabed (Figure 3.3 to Figure 3.7).

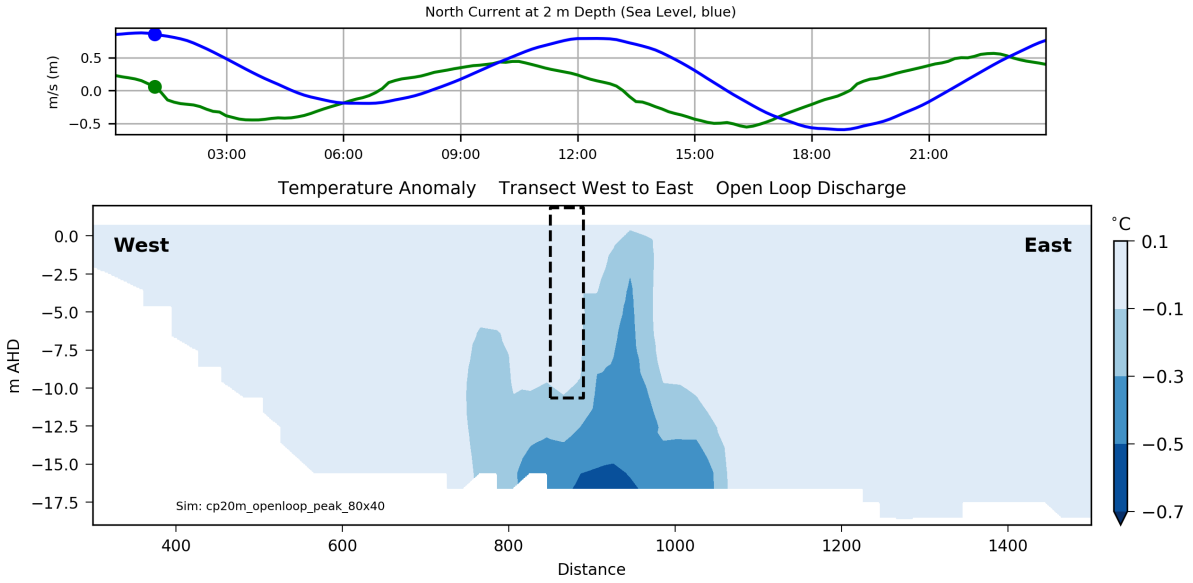

Figure 3.3 A cross-section west to east of the simulated temperature anomaly during high tide (sea level and northward current are shown in top time series panel, with circle indicating timing of cross-section; location of FSRU indicated by dashed line in cross-section).

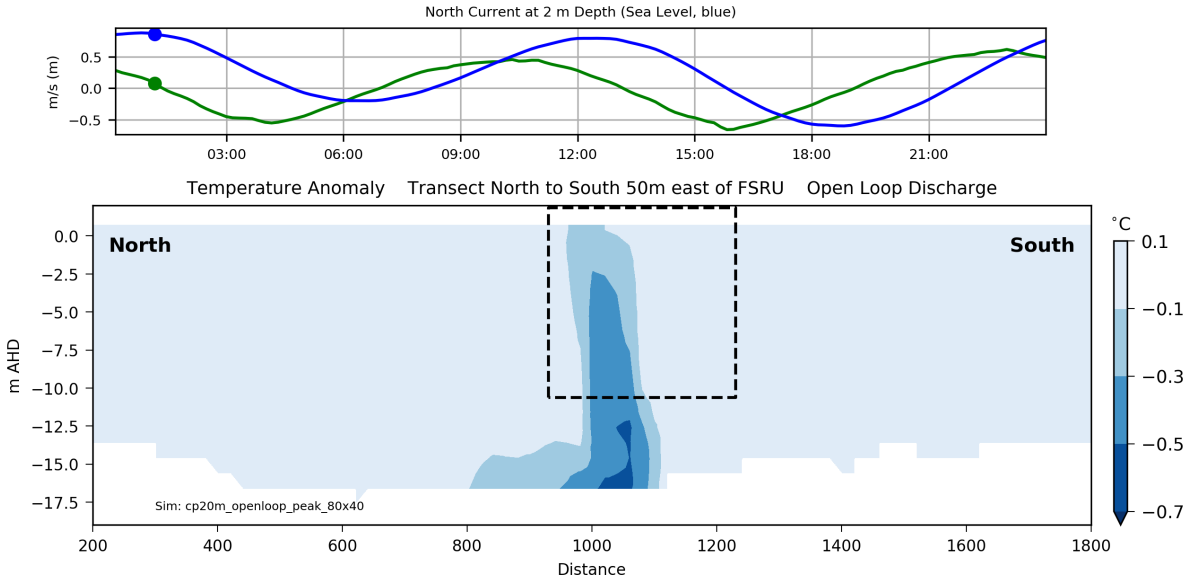

Figure 3.4 A cross-section north to south of the simulated temperature anomaly during high tide (sea level and northward current are shown in top time series panel, with circle indicating timing of cross-section; location of FSRU indicated by dashed line in cross-section).

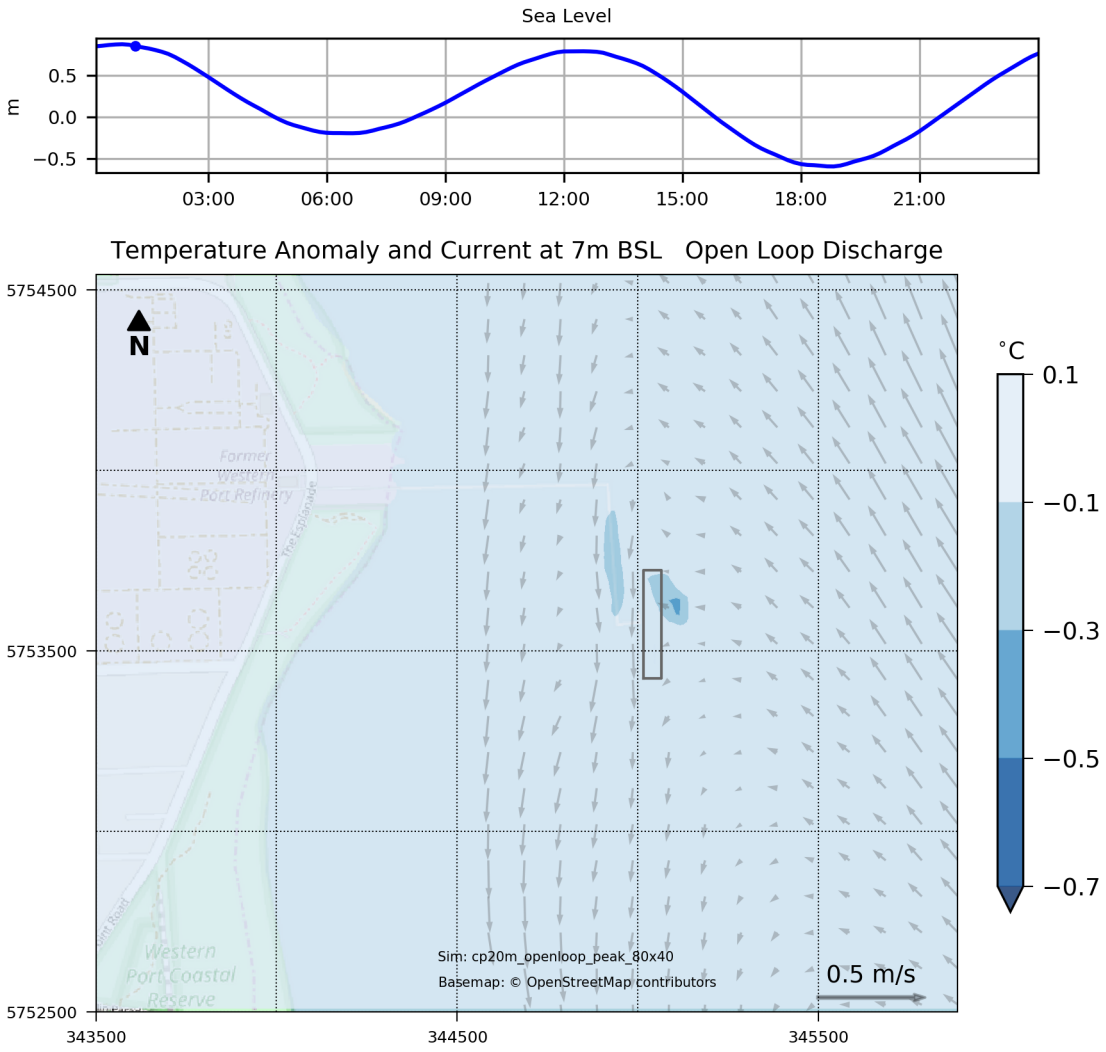

Figure 3.5 A plan view of the simulated temperature anomaly at 7 m below sea level during high tide (sea level is shown in top time series panel, with circle indicating timing of plan view).

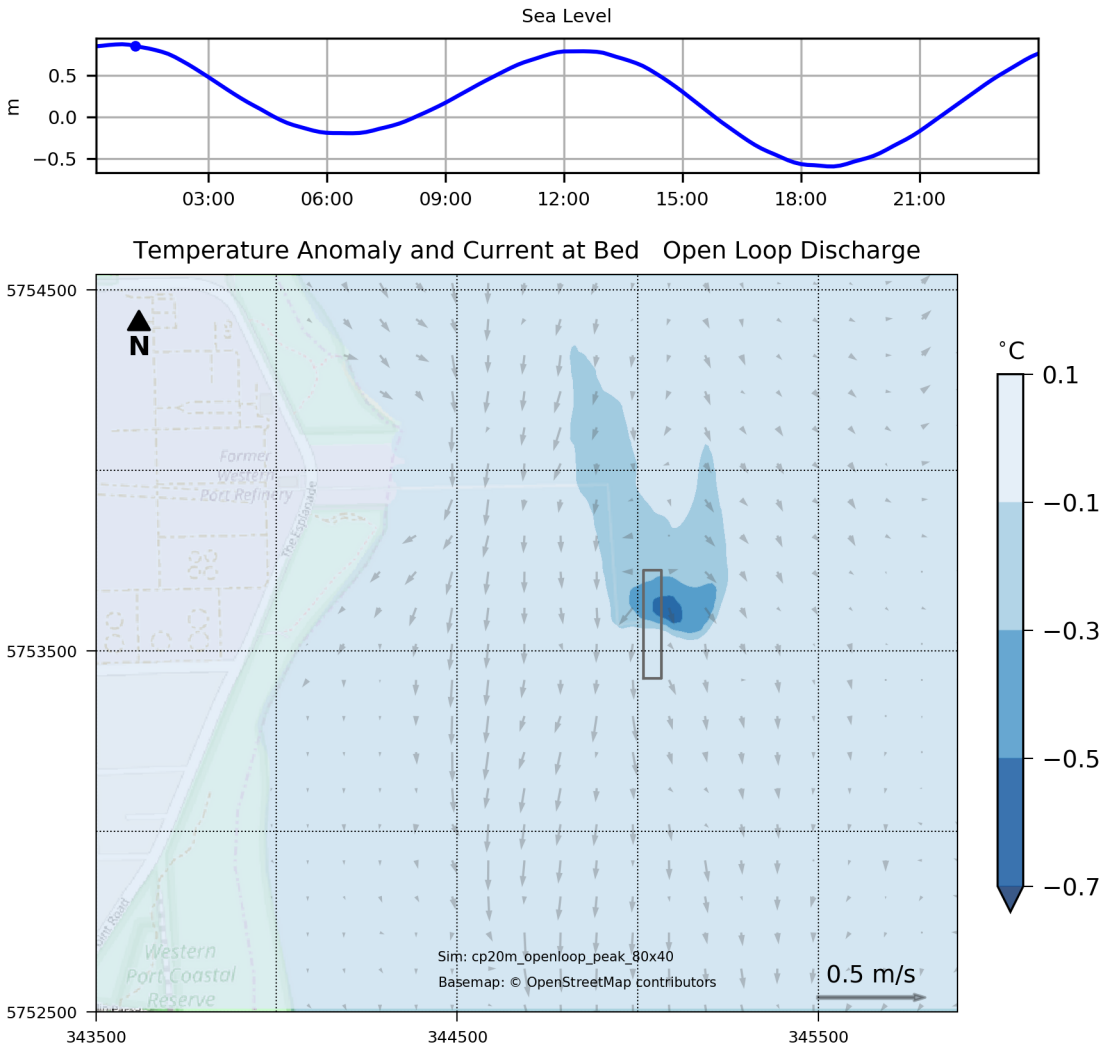

Figure 3.6 A plan view of the simulated temperature anomaly at the seabed during high tide (sea level is shown in top time series panel, with circle indicating timing of plan view).

Falling Tide

After slack water at high tide the currents increase southward as the tide falls. During this period there are two processes occurring. Firstly, the plume of new discharge water is injected into the far-field model back towards the hull of the FSRU (Table 3.2, Figure 3.2). This change is implemented based on the near-field modelling that indicates southward movement of the plume with the ambient current and reduced eastward trajectory. The plume near the ports remains in the mid-depth as the southerly current prevents direct descent beneath the vessel (Figure 3.7 and Figure 3.9). The plume reaches the bottom at some distance south of the vessel (Figure 3.8 and Figure 3.10) by which time it has become diluted. The southern elongation of the plume from the FSRU during falling tide is also partly due to a second process whereby the water that pooled near the bed during high tide moves south along the bed with the currents. While it travels along the seabed the pooled water is increasingly diluted by vertical and lateral mixing as shear increases, until mixing erodes the plume completely.

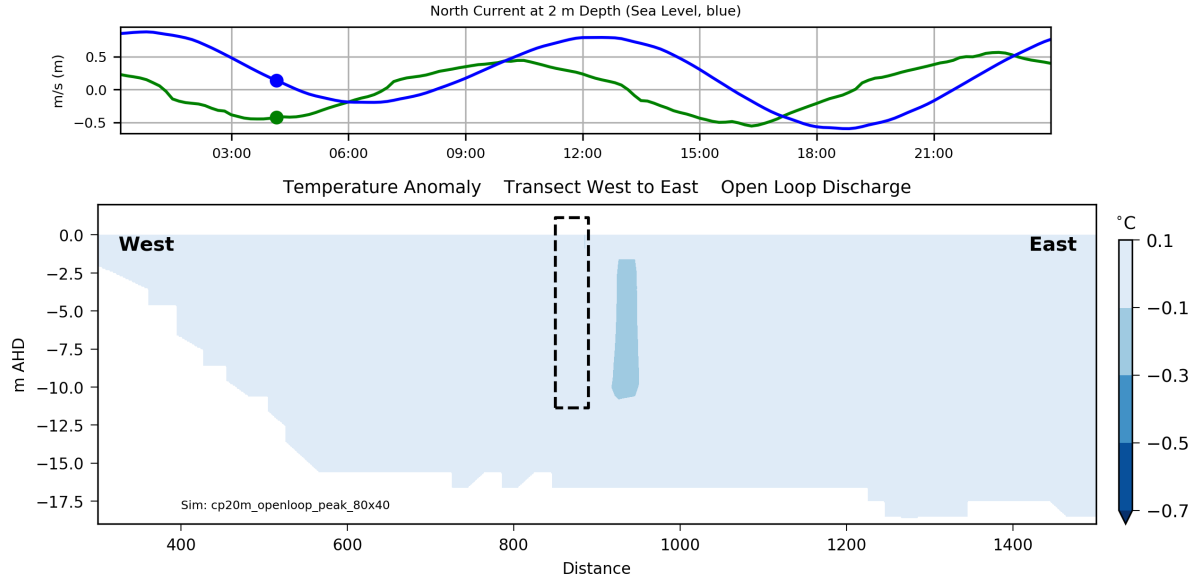

Figure 3.7 A cross-section west to east of the simulated temperature anomaly during falling tide (sea level and northward current are shown in top time series panel, with circle indicating timing of cross-section; location of FSRU indicated by dashed line in cross-section).

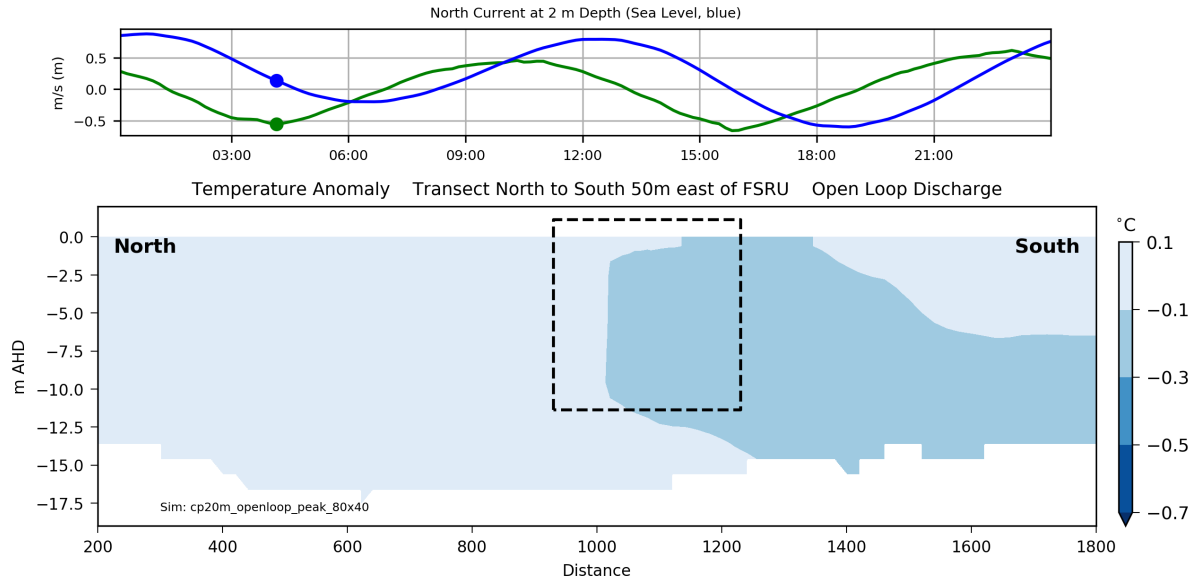

Figure 3.8 A cross-section north to south of the simulated temperature anomaly during falling tide (sea level and northward current are shown in top time series panel, with circle indicating timing of cross-section; location of FSRU indicated by dashed line in cross-section).

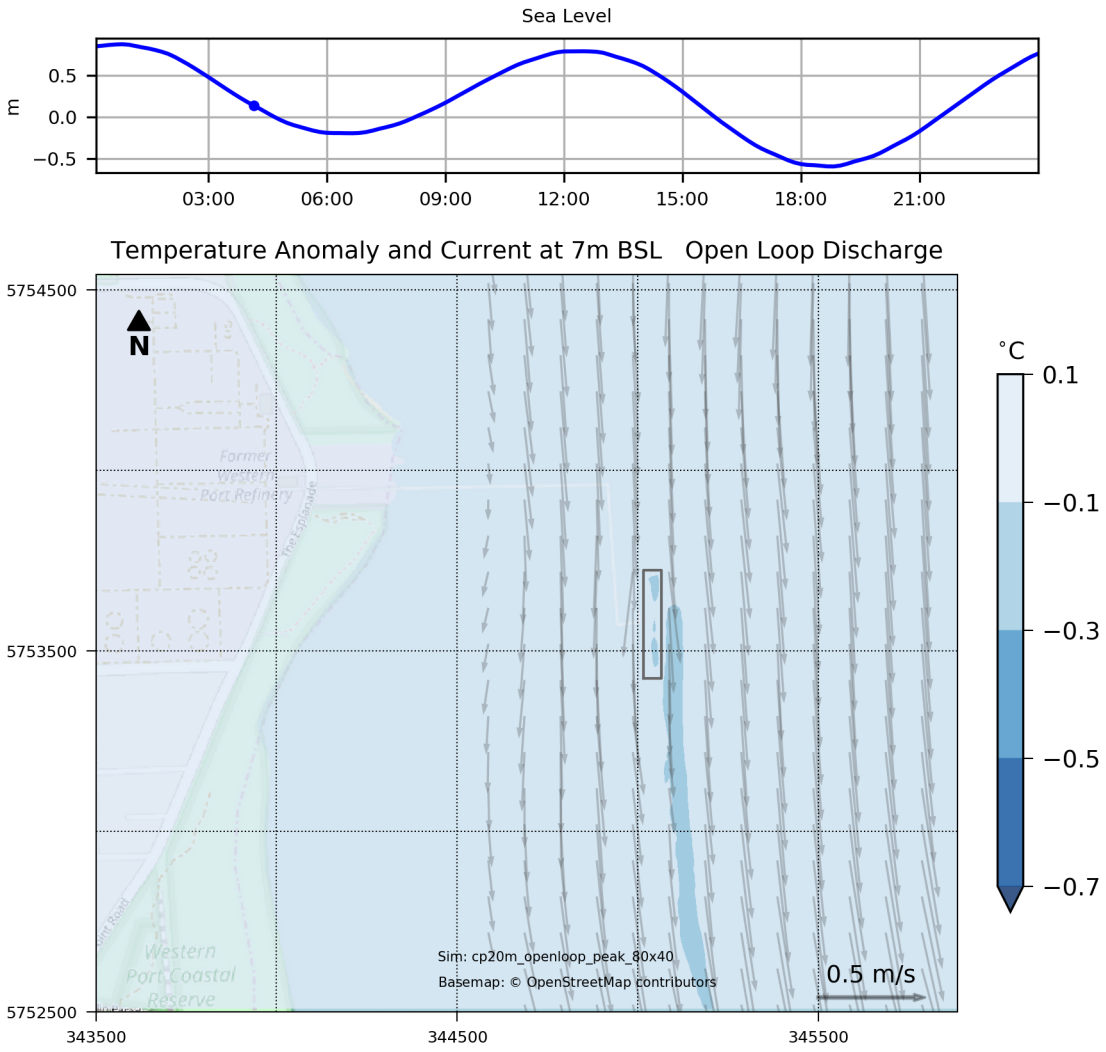

Figure 3.9 A plan view of the simulated temperature anomaly at 7 m below sea level during falling tide (sea level is shown in top time series panel, with circle indicating timing of plan view).

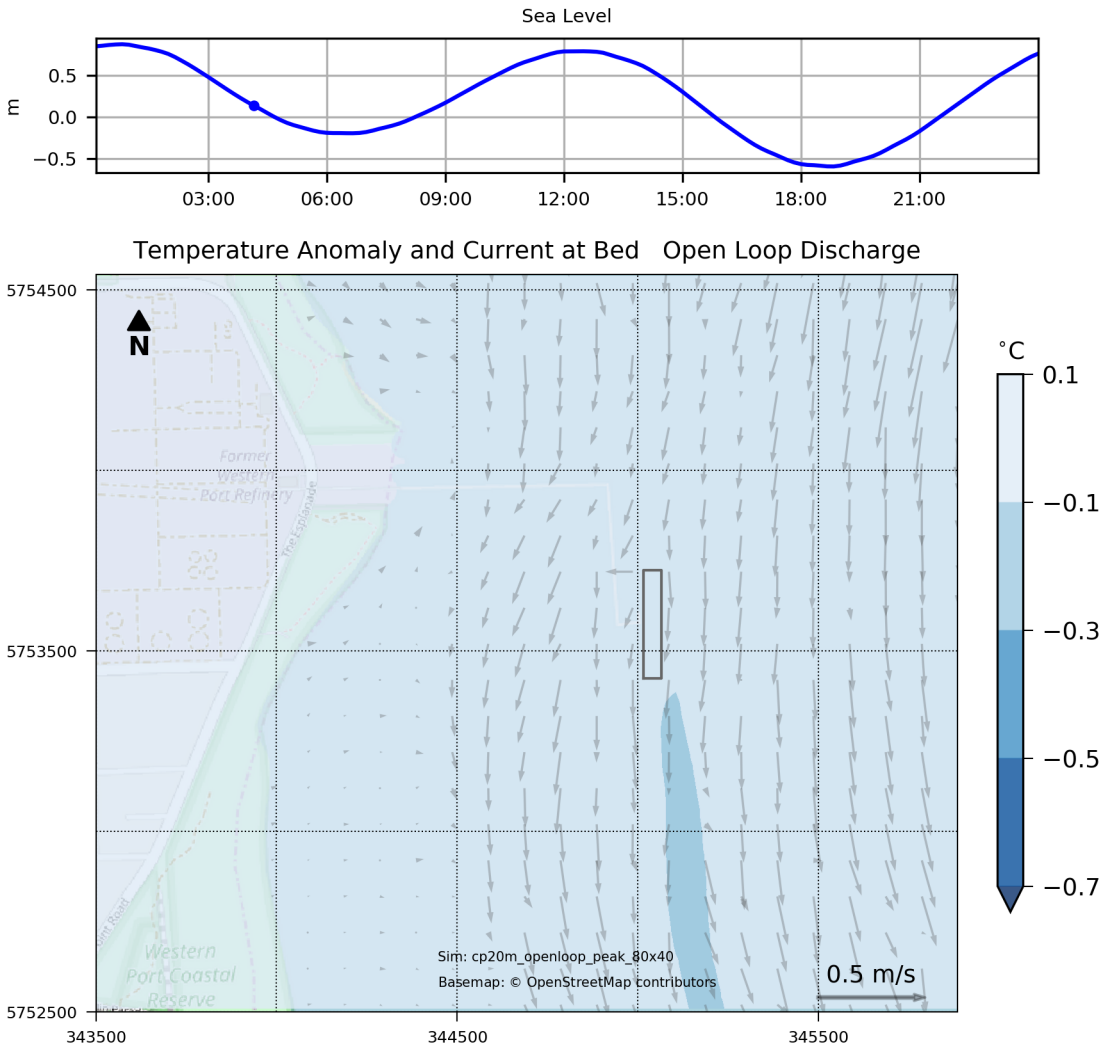

Figure 3.10 A plan view of the simulated temperature anomaly at the seabed during falling tide (sea level is shown in top time series panel, with circle indicating timing of plan view).

Low Tide

As low tide approaches the currents weaken and, as in the case of high tide, the momentum of the discharge from the heat exchange ports (as simulated in the near-field plume model) means that the plume is again injected at a distance of 60 m to the east of the FSRU. The plume collapses towards the bed and spreads radially as a dense flow (Figure 3.11 to Figure 3.12). The lowest temperatures are simulated at the bed below where the plume develops. Because there is less water depth at low tide to initially mix the plume the temperatures at the seabed beneath the FSRU are coolest at low tide.

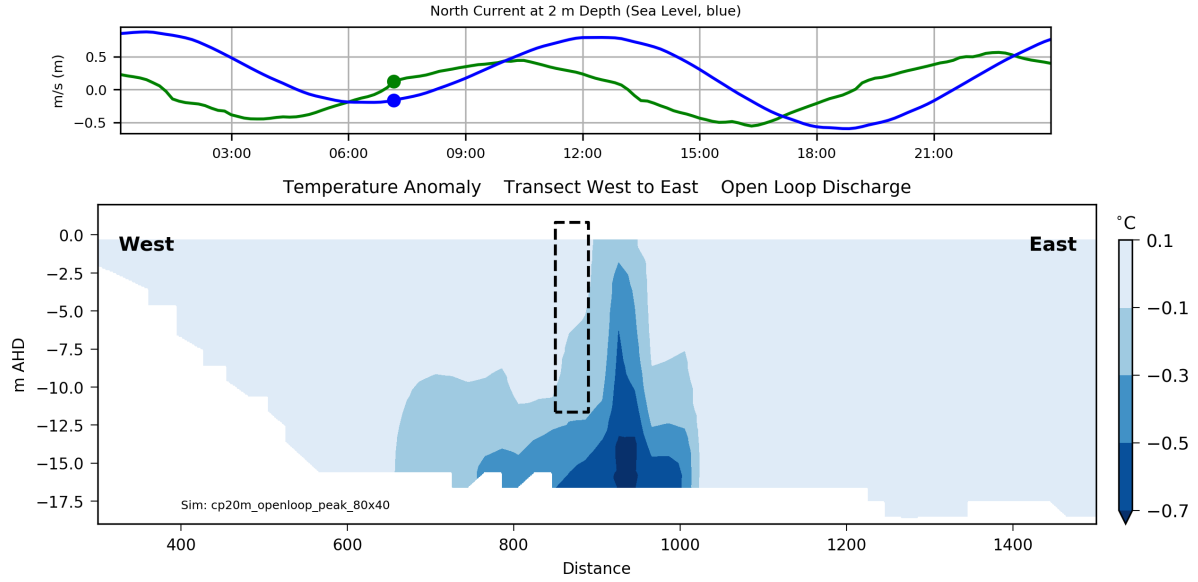

Figure 3.11 A cross-section west to east of the simulated temperature anomaly during low tide (sea level and northward current are shown in top time series panel, with circle indicating timing of cross-section; location of FSRU indicated by dashed line in cross-section).

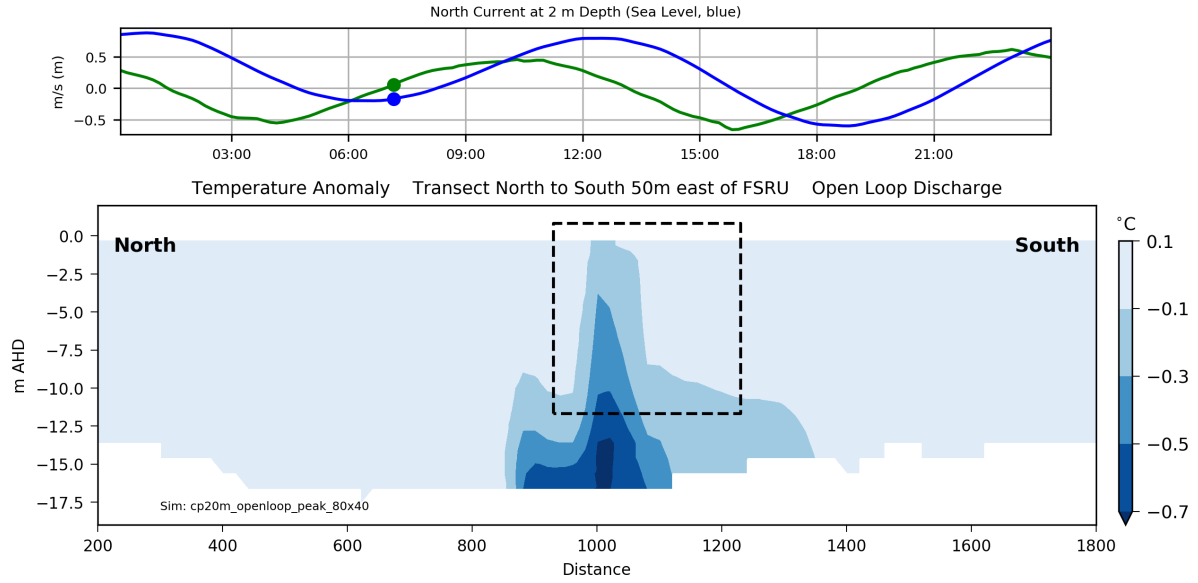

Figure 3.12 A cross-section north to south of the simulated temperature anomaly during falling tide (sea level and northward current are shown in top time series panel, with circle indicating timing of cross-section; location of FSRU indicated by dashed line in cross-section).

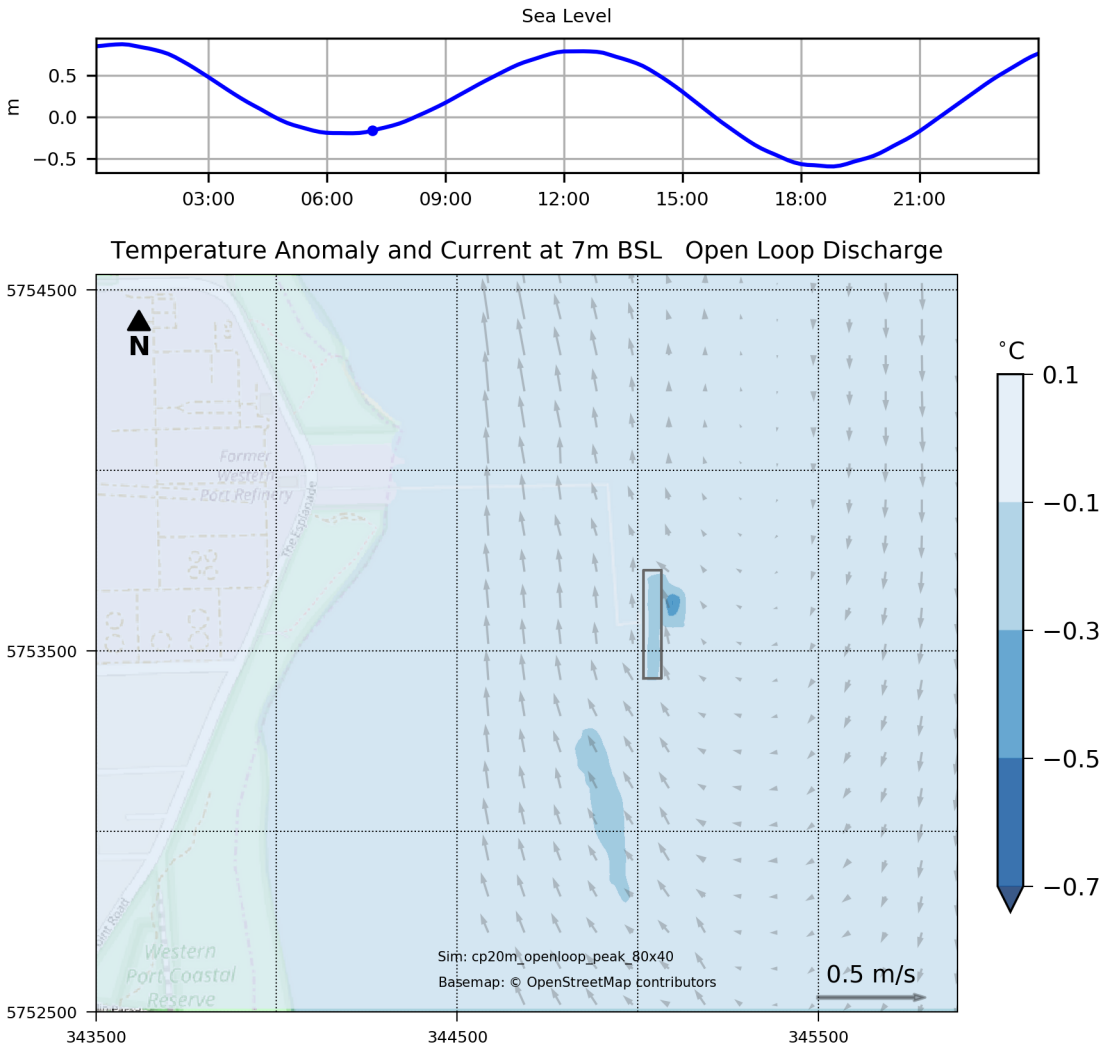

Figure 3.13 A plan view of the simulated temperature anomaly at 7 m below sea level during low tide (sea level is shown in top time series panel, with circle indicating timing of plan view).

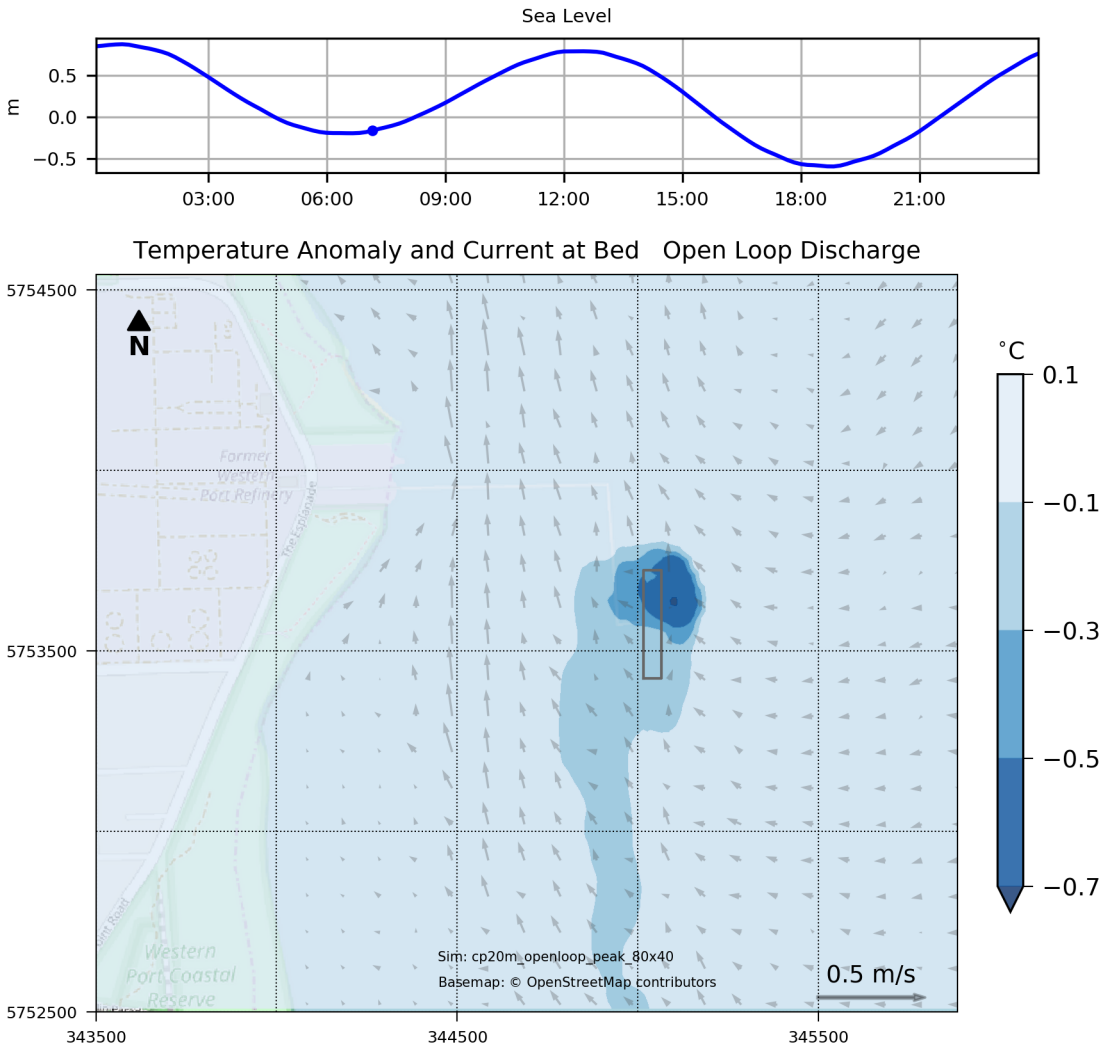

Figure 3.14 A plan view of the simulated temperature anomaly at the seabed during low tide (sea level is shown in top time series panel, with circle indicating timing of plan view).

Rising Tide

After slack water at low tide the currents increase northward so that the plume is injected further west towards the hull of the FSRU and higher in the water column (from Table 3.2). The new discharge water entering via the ports and water pooled near the bottom during low tide are transported north and diluted in the process (Figure 3.15 to Figure 3.18).

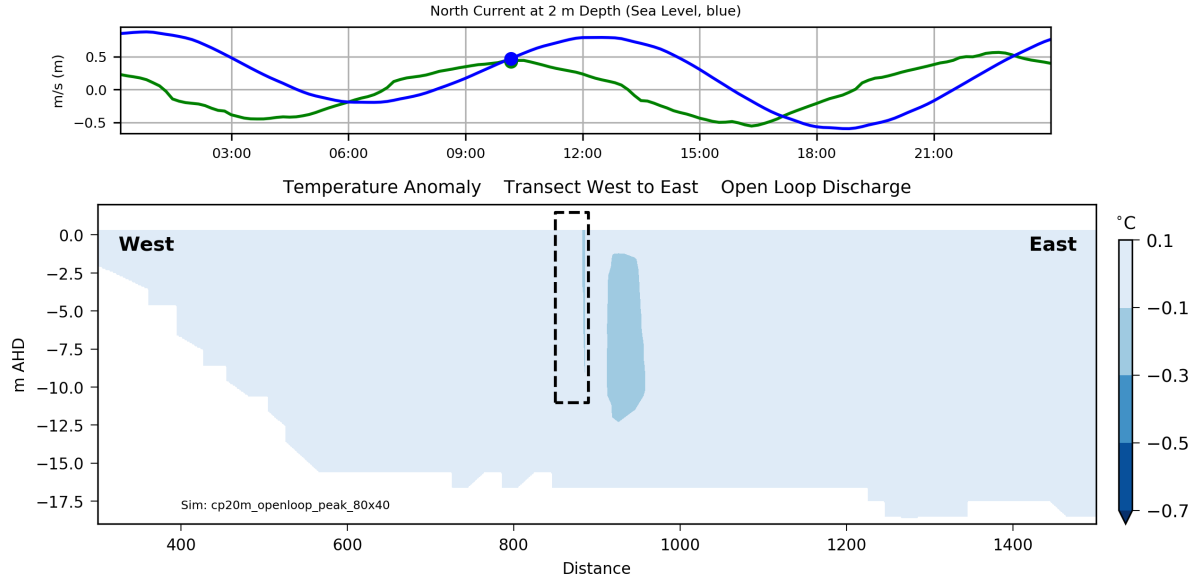

Figure 3.15 A cross-section west to east of the simulated temperature anomaly during rising tide (sea level and northward current are shown in top time series panel, with circle indicating timing of cross-section; location of FSRU indicated by dashed line in cross-section).

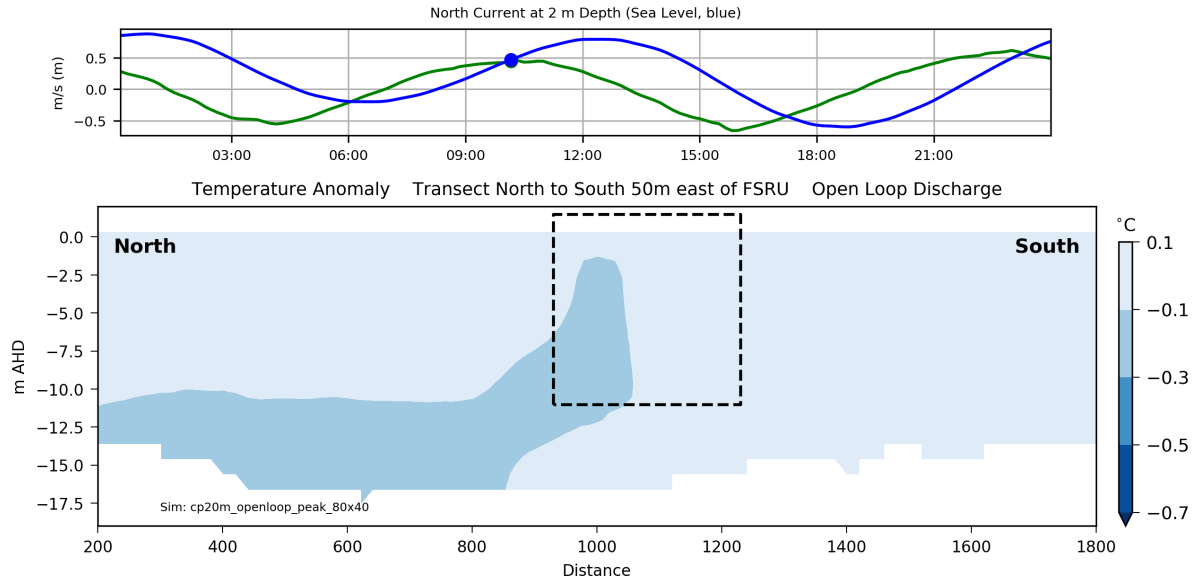

Figure 3.16 A cross-section north to south of the simulated temperature anomaly during rising tide (sea level and northward current are shown in top time series panel, with circle indicating timing of cross-section; location of FSRU indicated by dashed line in cross-section).

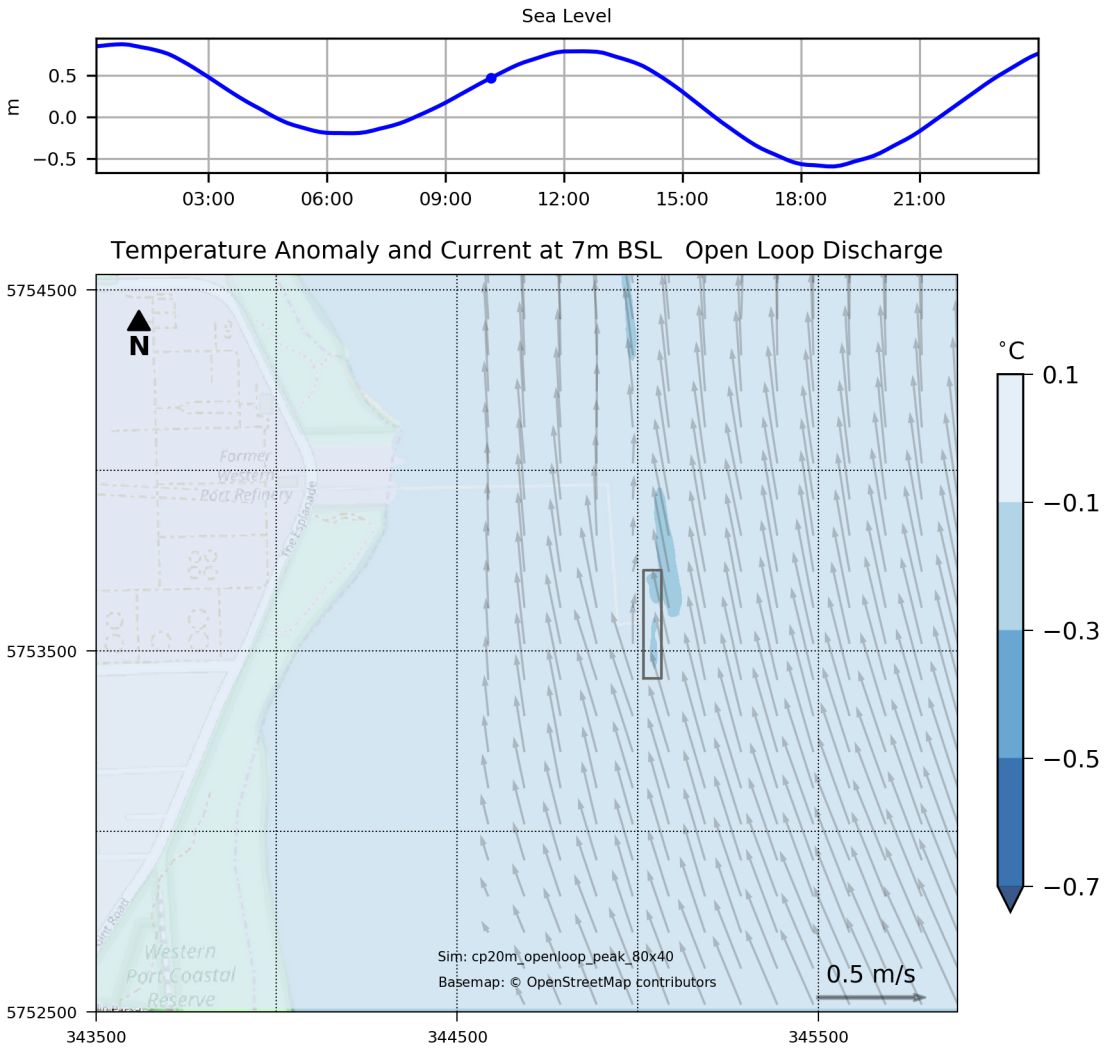

Figure 3.17 A plan view of the simulated temperature anomaly at 7 m below sea level during rising tide (sea level is shown in top time series panel, with circle indicating timing of plan view).

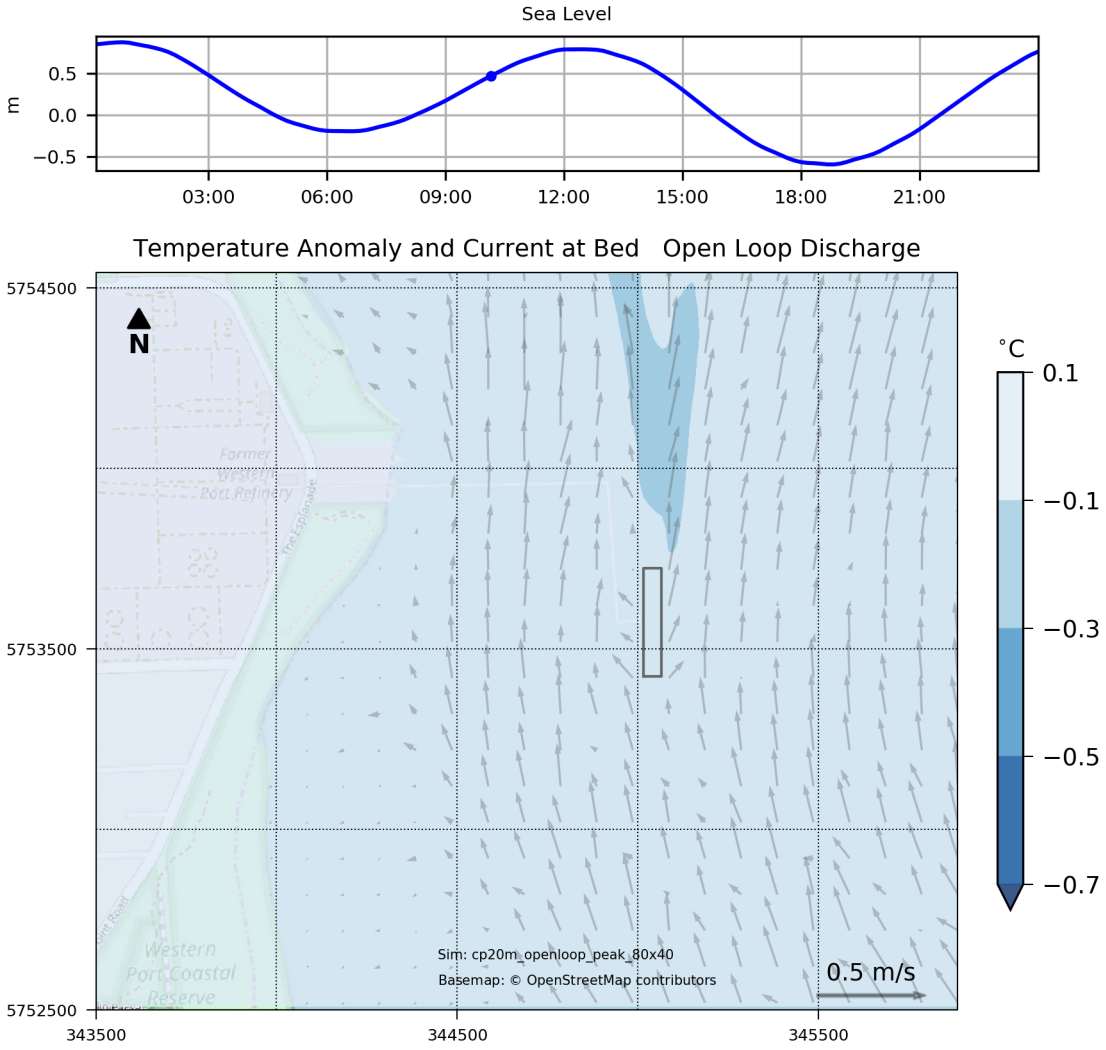

Figure 3.18 A plan view of the simulated temperature anomaly at the seabed during rising tide (sea level is shown in top time series panel, with circle indicating timing of plan view).

3.2.2 Peak FSRU Discharge

For the peak discharge case, the median and 20th percentile temperature decrease at the seabed is less than -0.3 °C from ambient. A map of the 10th percentile temperature decrease (Figure 3.19) shows a small area adjacent to the FSRU with temperatures -0.3 to -0.5 °C from ambient. The map of the 5th percentile temperature reduction (Figure 3.20) shows decreases between -0.5 and -0.7 °C adjacent to the FSRU where the discharge plume descends to the bed, and an outer contour of -0.3 to -0.5 °C extending 200 to 300 m north and south of the FSRU.

Timeseries of simulated temperature reductions at the seabed (Figure 3.21) indicate slack tide periods that briefly produce reductions down to -1 °C beneath the discharge with lowest temperatures occurring during low spring tides. At 300 m north and south of the input plume (i.e. 340 m north and south of the centre of the discharge ports) the reductions reach approximately -0.5 °C for brief periods after slack water, alternating between north and south for rising and falling tide respectively.

At 100 m west of the discharge plume the lowest temperatures are approximately -0.7 °C from ambient, and -0.2 °C at 200 m to the west. The temperatures remain higher (-0.1 to -0.3 °C from ambient) to the east (300 and 200 m, respectively) of the FSRU.

A 24-hour running average (i.e. averaged over approximately two low and high tide oscillations) of the temperature reductions at locations on the seabed (Figure 3.22) indicate that there are low-frequency signals in sea-level that change the average temperature reductions simulated at the bed. However, the results indicate that the 24-hour average temperature reduction lies between -0.05 and -0.15 °C at the locations considered over the 28-day simulation period. Importantly, the model does not suggest that there is ongoing cooling of waters at the bed.

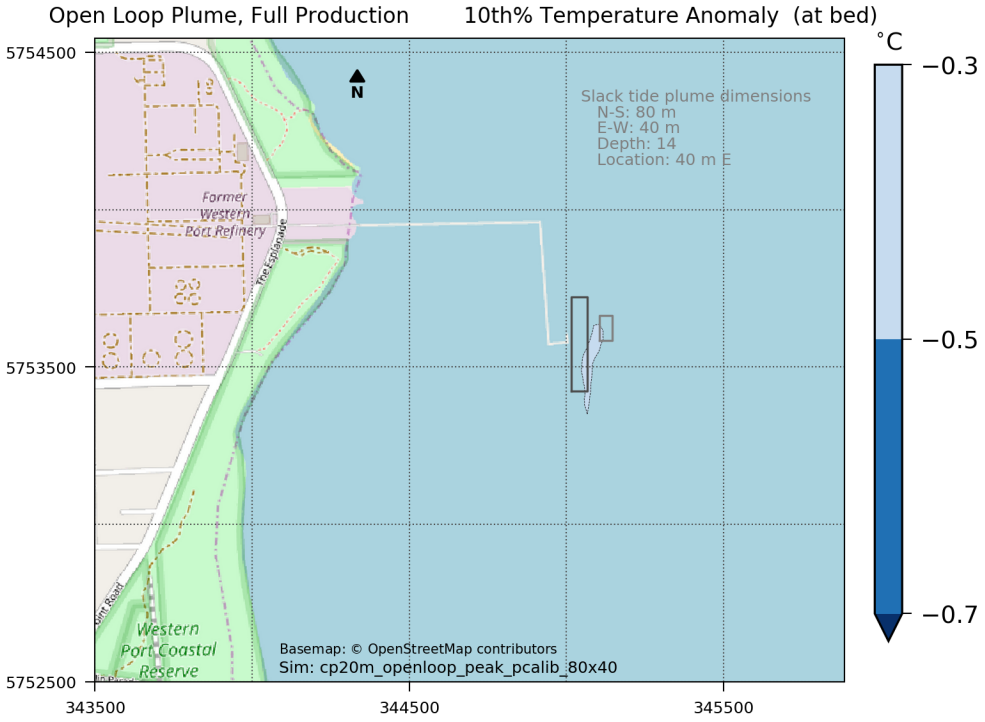

Figure 3.19 10th percentile of temperature change at the seabed over a 28-day simulation at peak FSRU discharge.

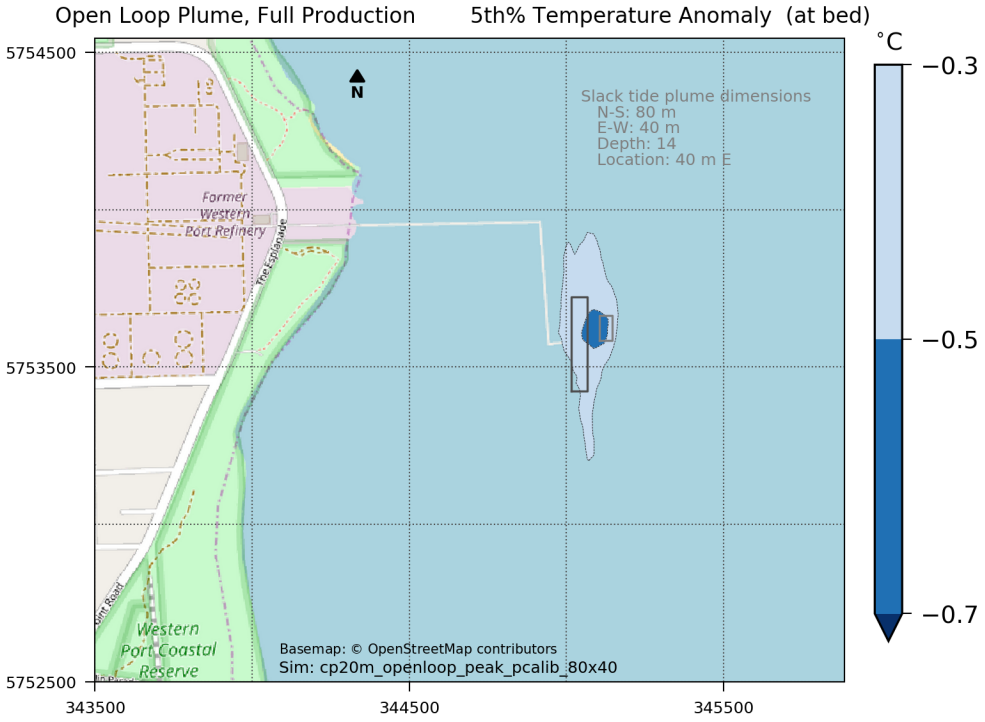

Figure 3.20 5th percentile of temperature change at the seabed over a 28-day simulation at peak FSRU discharge.

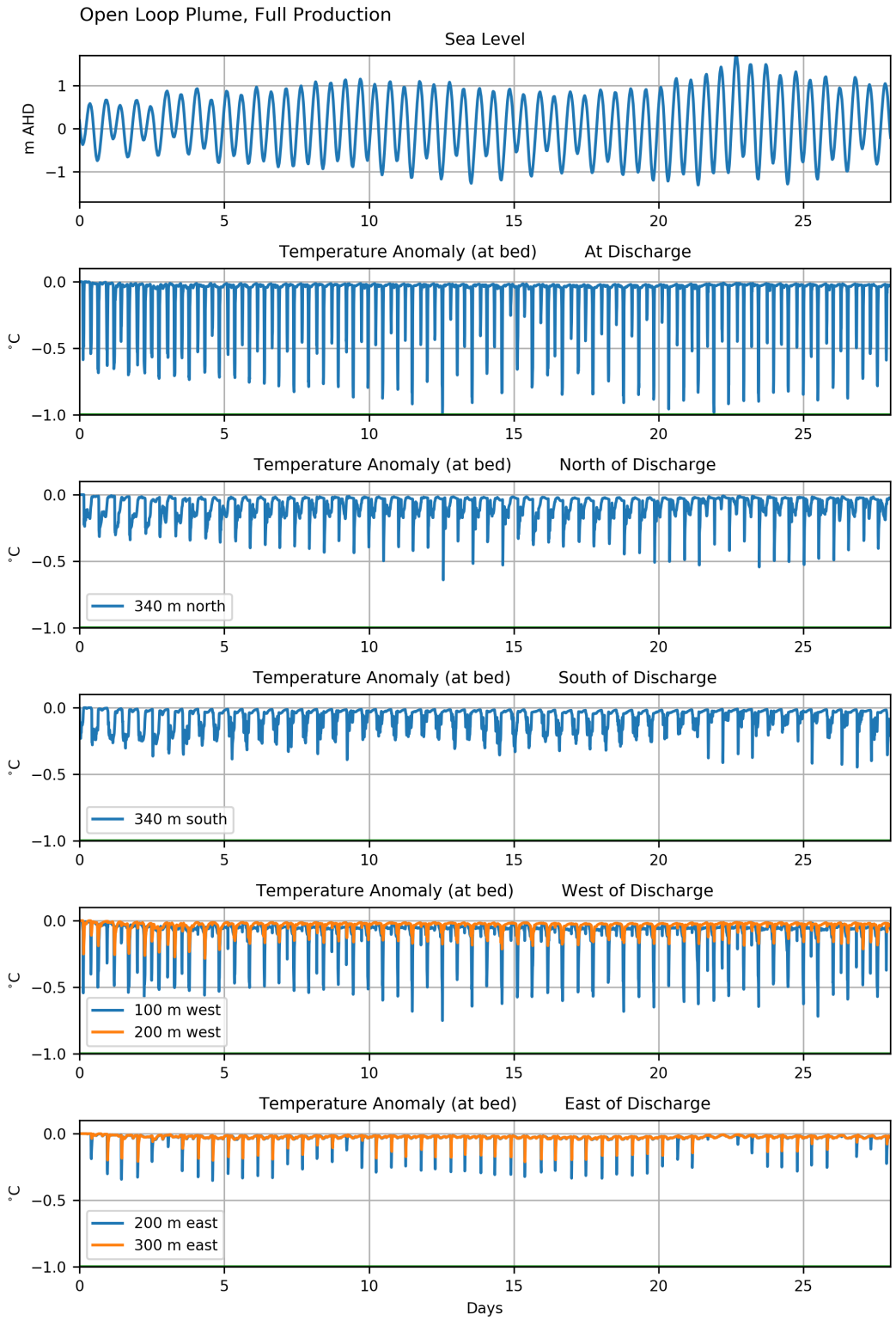

Figure 3.21 Time series of sea level (top panel) and (running down the page) temperature reduction at the seabed below the plume and north, south, west and east of the FSRU during peak discharge.

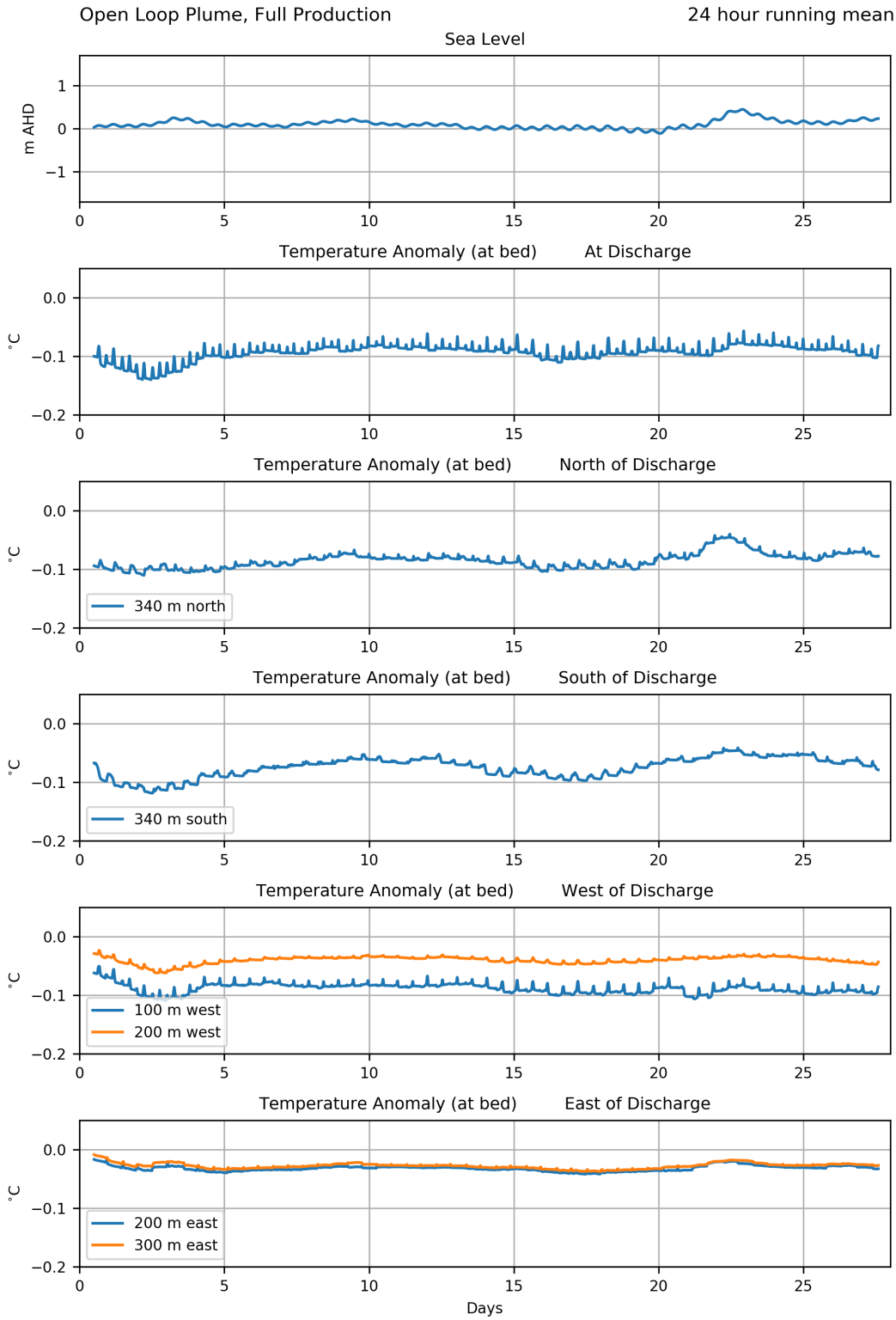

Figure 3.22 24-hr moving average time series of sea level (top panel) and (running down the page) temperature reduction at the seabed below the plume and north, south, west and east of the FSRU during peak discharge.

3.2.3 Average FSRU Discharge

For a reduced FSRU discharge rate occurring at two-thirds of peak production (i.e. 3.6 m^3/s) the 10th percentile temperature reduction is less than 0.3 °C. The 5th percentile map indicates

a reduction between -0.3 and -0.5 °C (Figure 3.23) in a region approximately 100 m length and width below the discharge ports.

Timeseries of simulated temperature reductions at the seabed (Figure 3.24) indicate slack tide periods that briefly produce reductions down to -0.7 °C beneath the discharge with lowest temperatures occurring during low spring tides. At 300 m north and south of the input plume (i.e. 340 m north and south of the centre of the discharge ports) the reductions reach approximately -0.3 °C for brief periods after slack water, alternating between north and south for rising and falling tide respectively.

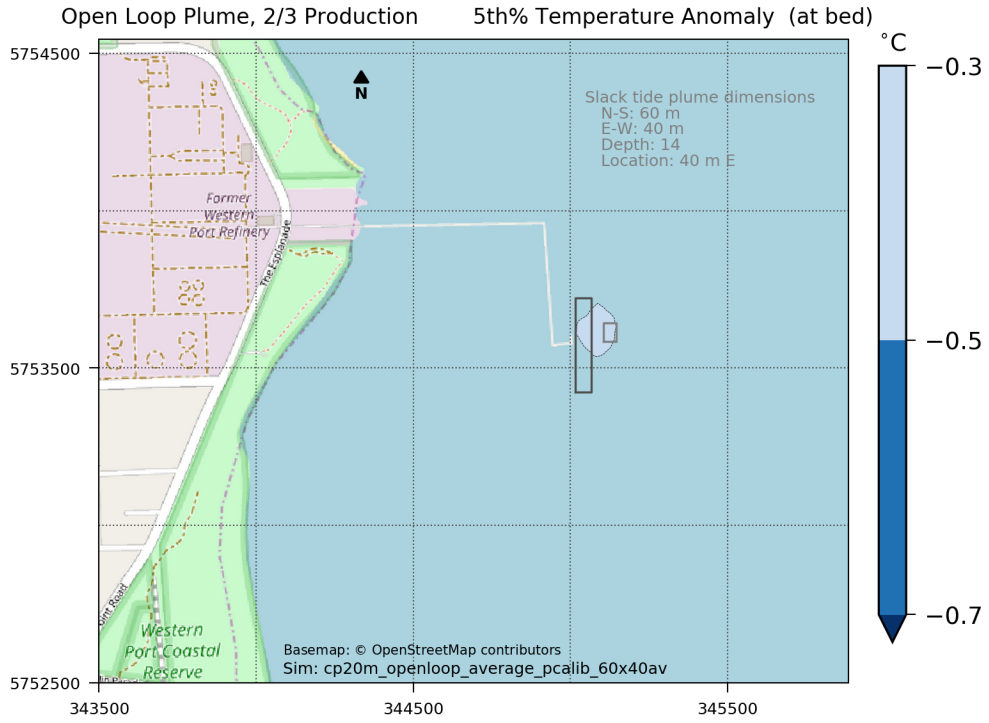

Figure 3.23 5th percentile of temperature change at the seabed over a 28-day simulation at average FSRU discharge.

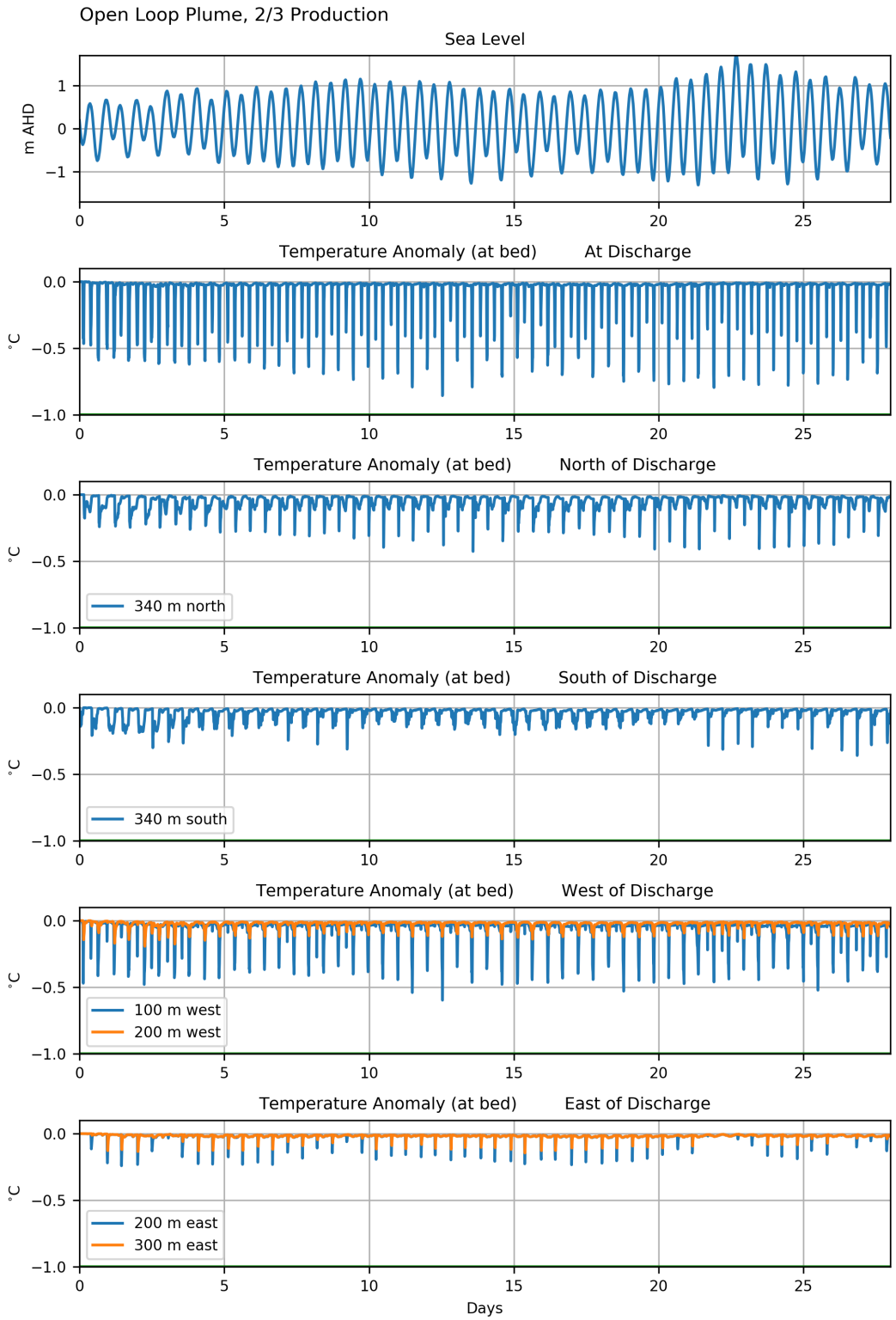

Figure 3.24 Time series of sea level (top panel) and (running down the page) temperature reduction at the seabed below the plume and north, south, west and east of the FSRU during average discharge.

3.3 Temperature Outcomes

The following summary can be drawn for temperature changes at the seabed during peak FSRU discharge rate of 5.4 m^3/s:

- For 10 % of the time there is a small area of seabed beside the FSRU (and extending for less than the dimensions for the FSRU) that experiences cooling of -0.3 to -0.5 ^oC from ambient; and
- For 5 % of the time there is:
    - A region beneath the plunging zone of the plume (approx. 100 m by 100 m) that experiences cooling of -0.5 to -0.7 ^oC from ambient; and
    - An outer region that extends up to 300 m north and south of the FSRU that experiences cooling of -0.3 to -0.5 ^oC from ambient. The width of the elongated plume is approximately 50 to 200 m, and widest near the FSRU.

For the average FSRU discharge rate of 3.6 m^3/s:

- For 5 % of the time there is region beneath the plunging area of the plume (approx. 100 m by 100 m) that experiences cooling of -0.3 to 0.5 ^oC from ambient.

Cumulative Impacts

At the bay-wide scale, heat fluxes are dominated by exchanges with the ocean and atmosphere (on diurnal and seasonal cycles and during events such as storms) so that the dispersed cool water has a local effect but a negligible large scale or cumulative effect on the water temperatures in the remainder of the bay. The model results indicate no continual cooling of waters at the seabed in the project area.